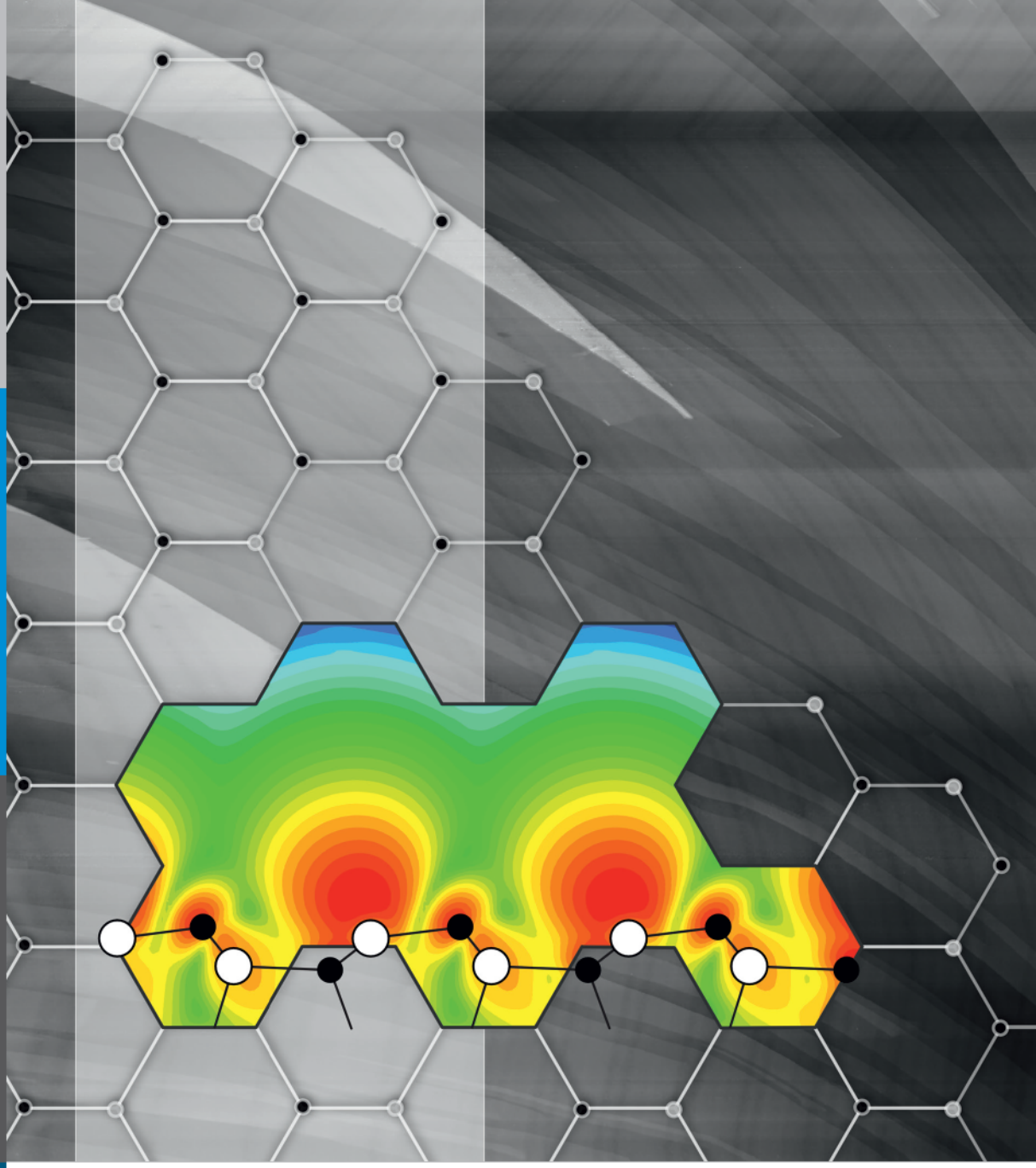

Structure, electronic properties, and interactions of defects in epitaxial GaN layers

Phillip H. Weidlich

JÜLICH
FORSCHUNGSZENTRUM

Mitglied der Helmholtz-Gemeinschaft

Schriften des Forschungszentrums Jülich
Reihe Information / Information Band / Volume 34

Forschungszentrum Jülich GmbH
Peter Grünberg Institute (PGI)
Microstructure Research (PGI-5)

Structure, electronic properties, and interactions of defects in epitaxial GaN layers

Phillip H. Weidlich

Schriften des Forschungszentrums Jülich
Reihe Information / Information Band / Volume 34

ISSN 1866-1777 ISBN 978-3-89336-951-5

Bibliographic information published by the Deutsche Nationalbibliothek.
The Deutsche Nationalbibliothek lists this publication in the Deutsche Nationalbibliografie; detailed bibliographic data are available in the Internet at http://dnb.d-nb.de.

Publisher and Distributor: Forschungszentrum Jülich GmbH
Zentralbibliothek
52425 Jülich
Tel: +49 2461 61-5368
Fax: +49 2461 61-6103
Email: zb-publikation@fz-juelich.de
www.fz-juelich.de/zb

Cover Design: Grafische Medien, Forschungszentrum Jülich GmbH

Printer: Grafische Medien, Forschungszentrum Jülich GmbH

Schriften des Forschungszentrums Jülich
Reihe Information / Information, Band / Volume 34

D 82 (Diss., RWTH Aachen, University, 2013)

ISSN 1866-1777
ISBN 978-3-89336-951-5

The complete volume is freely available on the Internet on the Jülicher Open Access Server (JUWEL) at www.fz-juelich.de/zb/juwel

Contents

1. Introduction **7**

I. Theoretical principles and experimental techniques **11**

2. Theory of the scanning tunneling microscope **13**
2.1. Fundamental theory 13
2.2. Theory of the band structure 19

3. Properties of wurtzite gallium nitride **23**

4. Experimental techniques **27**
4.1. Preparation of samples 27
4.2. Preparation of tips 29
4.3. Correction of nonlinear distortions in STM images 29

5. Experimental details **37**
5.1. Experimental details of Part II 37
5.2. Experimental details of Part III and Part IV 38

II. Hidden surface states at GaN ($10\bar{1}0$) surfaces **39**

6. Introduction **41**

7. Initial experiment **43**
7.1. Experimental results 43
7.2. Discussion of the tunneling spectra 44

8. Ab initio calculations **47**
8.1. Calculation method 47
8.2. Surface states and dispersion 49
8.3. Decay of the DOS into the vacuum 50

9. Experimental identification of the surface state **55**
9.1. Modified experiment 55
9.2. Experimental results and discussion 58

III. XSTM of v-shaped defects in gallium nitride **61**

10. Introduction **63**

11. Doping modulation in epitaxial gallium nitride **65**
11.1. Features on large scale STM images 65
11.2. Characterization of the modulation 68
11.3. Discussion of the contrast 69

12. Evidence of deep traps **73**
12.1. Scanning tunneling microscopy observations 73
12.2. Determination of the geometric structure 75
12.3. Scanning tunneling spectroscopy on v-shaped defects 78
12.4. Discussion of the electronic properties 79

13. Meandering of v-shaped defects **83**
13.1. Experimental observations 83
13.2. Quantification of the meandering 85
13.3. Determination of the origin of the meandering 87

IV. Characterization of dislocations and their interactions **91**

14. Introduction **93**

15. Repulsive interactions of dislocations **95**
15.1. Experimental observations 95
15.2. Distribution of the dislocations 98
15.3. Discussion 102

16. Analysis of dislocations **105**
16.1. Determination of the intersection angle of the dislocation line 105
16.2. Simulation of the displacement field of a dislocation 112

17. Conclusion **115**

Bibliography **117**

List of Figures **131**

Abbreviations **133**

Symbols **135**

1. Introduction

Gallium nitride (GaN) is a III-V semiconductor which is widely used in optoelectronic devices, especially in lasers and light emitting diodes (LEDs). Due to its wide band gap of approximately 3.4 eV at room temperature [1], GaN - like related ternary group III-nitride semiconductors - is a material of choice for the emission of light within the blue to near ultraviolet range [2]. Due to its application in ultraviolet LEDs, GaN is deployed in microelectronic devices, but also finds use in the medical field both for diagnostic and therapeutic purposes as well as for the purification of air and water [3]. At present, the efficacy of devices based on GaN is, however, limited by the quality of the bulk crystal material. Since there are hardly any large bulk substrates available [4], almost all GaN films are grown on substrates which exhibit a large lattice mismatch as well as a large thermal mismatch using heteroepitaxy or are deposited onto pseudo substrates which themselves were nucleated on mismatched substrates [3]. The mismatch induces high concentrations of defects, of which dislocations negatively affect the properties of the device in particular. Dislocations in transistors, for example, can cause a large reverse bias leakage [5] and threading dislocations have been associated with luminescence at various wavelengths in GaN epitaxial layers [6].

Although group III-nitrides and especially GaN are already being used commercially in optoelectronic devices, the knowledge of the general properties of defects within these materials and of the interactions between the defects in particular is still limited: The electronic properties of dislocations, for example, are debated controversially, with different groups reporting either only charged or only uncharged dislocations or a mixture of both [7–14] depending on the type of dislocation as well as on the material investigated. In addition, various ideas on the origin of charges spanning from reconstructions of the dislocation cores, impurities, point defects, to strain [14–21] are being discussed. Similarly, the electronic

properties of other extended defects, such as v-shaped defects, are still not fully understood [22].

To improve the quality of GaN substrates, the high concentrations of the various defects present, especially of dislocations, have to be reduced [23]. A large variety of methods targeting the reduction of defects in GaN have been developed recently, including epitaxial lateral overgrowth (ELO), patterning with semipolar facets, introduction of interlayers into the material, and 3D to 2D growth transitions [23–33]. The aim of all these methods is to interrupt the propagation of dislocations along the growth direction by bending their line direction. Crucial factors for the optimization of the reduction of dislocations are the interaction between dislocations themselves, between dislocations and the growth front as well as between dislocations and other defects. Unfortunately, rather little is known about interactions of dislocations in GaN epitaxial layers [34–37].

Therefore, this thesis investigates the structure, electronic properties, and interactions of extended defects in GaN epitaxial layers using cross-sectional scanning tunneling microscopy (XSTM) and spectroscopy (XSTS). This study is divided into four parts.

In Part I, theoretical principles and experimental techniques are presented. Chapter 2 introduces the variables needed to characterize and simulate scanning tunneling spectra with regard to tip-induced band bending. The physical properties of wurtzite structure gallium nitride are briefly noted in Chapter 3. In Chapter 4, a methodology is presented which allows to reduce nonlinear distortions in large scale scanning tunneling images by using information gained from probing a custom-built calibration sample consisting of a single crystal Nb:$SrTiO_3$ substrate equipped with an added periodical pattern of TiO_2 features.

In Part II, a new approach is developed to probe the controversially debated minimum of the empty GaN $(10\bar{1}0)$ surface state. The results of *ab initio* calculations shown in Chapter 8 provide a set of experimental parameters which allow for the empty surface state to be found below the minimum of the conduction band and hence proven to be situated within the fundamental band gap as shown in Chapter 9.

Part III addresses the formation and the characteristics of overgrown v-shaped defects in gallium nitride epitaxial layers by investigating their geometric and

electronic structure utilizing cross-sectional scanning tunneling microscopy and spectroscopy. Using a doping modulation presented in Chapter 11 to determine the opening angle of the v-shaped defects, these defects are found to be three-dimensional hexagonal pyramidal structures defined by six inclined $\{11\bar{2}2\}$ facets in Chapter 12. The defects exhibit inhomogeneous electronic properties which arise from the presence of deep traps. Additionally, the v-shaped defects meander perpendicular to the growth direction, as shown in Chapter 13.

In PART IV the interactions between dislocations themselves, between dislocations and the inclined growth front as well as between dislocations and other defects are investigated. A comparison of the spatial distribution of the dislocations and their line directions in Chapter 15 reveals the dislocations being bent away from the semipolar facets of the v-shaped defects. The dislocations are found to form bundles of dislocations with parallel projected line directions. For a better characterization of dislocations, a method for the determination of the angle between the line of a dislocation intersecting the surface and the cleavage surface itself is presented in Chapter 16. Chapter 17 summarizes the results of this work.

Part I.

Theoretical principles and experimental techniques

2. Theory of the scanning tunneling microscope

2.1. Fundamental theory

2.1.1. One-dimensional tunneling effect

In classic electrodynamics, an electron with energy E cannot pass a barrier of height V_0 as long as E is smaller than V_0. In quantum mechanics, however, there is a finite probability for the electron to enter the barrier and even for passing it [38]. Considering the one-dimensional case of a time-constant potential $V(z)$ of height V_0 and width z_0, as shown in Figure 2.1, as well as an electron of mass m and energy $0 < E < V_0$, the electron can be described by a complex wave function $\psi(z)$, if $\psi(z)$ is a solution to the one-dimensional Schrödinger equation:

$$-\frac{\hbar^2}{2m}\frac{\mathrm{d}^2}{\mathrm{d}z^2}\psi(z) + V_p(z)\psi(z) = E\psi(z) \tag{2.1}$$

For $-\infty < z < 0$ and $z_0 < z < \infty$, $\psi(z)$ is a planar wave function. For $0 < z < z_0$, however, $\psi(z)$ is an evanescent wave:

$$\psi(z) \sim e^{-\kappa z} \tag{2.2}$$

with a decay constant, κ, given by:

$$\kappa = \sqrt{\frac{2m(V_0(z) - E)}{\hbar^2}} \tag{2.3}$$

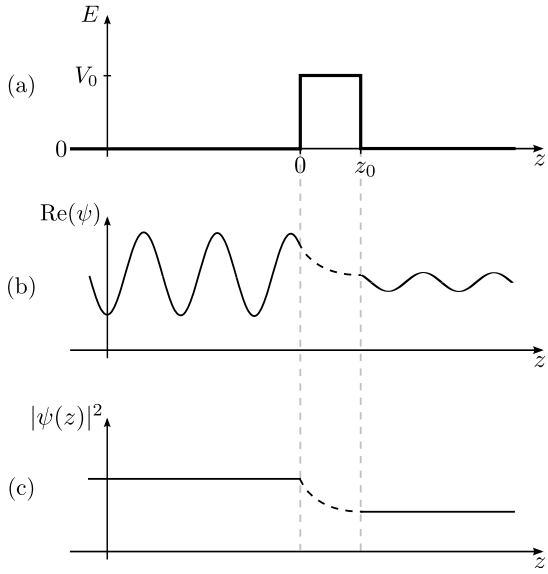

Figure 2.1. *Quantum tunneling in one dimension for an electron traveling in the $-z$ to z direction. (a) Time-constant potential $V(z)$ with height V_0. (b) Real part* $\mathrm{Re}(\psi)$ *of the wave function $\psi(z)$ which is a planar wave when outside of the barrier ($-\infty < z < 0$ and $z_0 < z < \infty$) and an evanescent wave within the potential barrier ($0 < z < z_0$ range). (c) Probability density $|\psi(z)|^2$ of the electron in real space. The probability of the electron being located in the $z > z_0$ range is smaller than that of the $z < 0$ regime due to the evanescent wave function within the potential, $\psi(z) \sim e^{-\kappa z}$, which causes an exponential decrease in the probability of the electron being in the $z > z_0$ range.*

Figure 2.1(c) depicts the probability density $|\psi(z)|^2$ of the electron in real space. For electrons traveling in the $-z$ to z direction, the probability of the electron being situated in the $z > z_0$ region is smaller than that of the $z < 0$ regime. It is, however, greater than zero, as long as z_0 is small enough. This is a consequence of the evanescent wave function within the potential, $\psi(z) \sim e^{-\kappa z}$, which causes an exponential decrease in the probability of the electron being in the $z > z_0$ range with increasing z_0.

The scanning tunneling microscope utilizes this very effect. The tip is brought into close proximity z to the sample (located at $z=0$), with z being small enough for electrons to tunnel from the tip into the sample or vice versa, depending on the polarity of the voltage applied to the gap between tip and sample. While scanning the tip across the surface, any difference in the local elevation of the surface will change the distance between tip and sample and because of $\psi(z) \sim e^{-\kappa z}$ influence the current. If the tip is solely moved horizontally, the change in the current can directly be related to the change in height of the surface of the sample. Images acquired using this method are called *constant-height* images. A more commonly used technique is keeping the current constant while scanning the tip across the surface. This case necessitates a vertical adjustment of the tip position during the horizontal movement in order to keep z constant and thus keeping the tunneling current constant. Information on the structure of the surface is then gained by recording the vertical movements of the tip and the images acquired in this matter are called *constant-current* images. A theoretical description of the quantification of the tunneling current is presented below.

2.1.2. Tunneling current

According to the approach developed by Bardeen, the tunneling current between the sample and the tip can be calculated using perturbation theory [39]. The current in first order perturbation theory can be written as:

$$I = \frac{2\pi e}{\hbar} \cdot \sum_{t,s} f(E_t)\left[1 - f(E_s + eV)\right] \cdot |M_{ts}|^2 \cdot \delta\left(E_t - E_s\right) \tag{2.4}$$

with V being the voltage applied between the tip and the sample, M_{ts} the matrix element of the transition of a state ψ_t in the tip to a state ψ_s in the sample, E_t and E_s the energies of the states ψ_t, ψ_s, respectively, and $f(E)$ being the Fermi-Dirac distribution shown in Equation 2.5:

$$f(E) = \frac{1}{1 + e^{\frac{E - E_F}{k_B T}}} \tag{2.5}$$

Equation 2.4 exhibits a strong similarity to *Fermi's Golden Rule* [40, 41], which describes the transition of a state n with energy ε_n into another state n' with energy $\varepsilon_{n'}$:

$$\Gamma_{n\to n'} = \frac{2\pi}{\hbar} \cdot |M_{n'n}|^2 \cdot \delta\left(\varepsilon_{n'} - \varepsilon_n\right) \tag{2.6}$$

Assuming low temperatures, small gap voltages, and conservation of energy, Equation 2.4 can be simplified to:

$$I = \frac{2\pi}{\hbar} \cdot e^2 V \cdot \sum_{t,s} |M_{ts}|^2 \cdot \delta(E_s - E_F) \cdot \delta(E_t - E_F) \tag{2.7}$$

In their continuative approach [42, 43], Tersoff and Hamann assume that both tip and sample have the same work functions $\Phi_t = \Phi_s \equiv \Phi$ and that the tip can be considered having an s-type orbital with a radius of curvature R as shown in Figure 2.2. They further assume that the wave functions of the tip are extremely localized. This allows the simplification of Equation 2.7 to:

$$I \propto \left(\frac{32\pi^3 e^2 V \Phi^2 R^2}{\hbar\kappa^4}\right) \cdot e^{2\kappa R} \cdot D_t(E_F) \cdot \rho(\vec{r}_0, E_F) \tag{2.8}$$

where D_t is the density of states of the tip per unit of volume and $\rho(\vec{r_0}, E_F)$ is the density of states of the sample at the Fermi energy being measured at the position $\vec{r_0}$ of the tip above the surface. Consequently, Equation 2.8 primarily states a proportionality of the tunneling current to the local density of states $\rho(\vec{r}_0, E_F)$ of the sample close to the Fermi energy E_F at the position of the tip above the surface of the sample, $\vec{r}_0$:

$$I \propto \rho(\vec{r}_0, E_F) \tag{2.9}$$

If solely the vertical distance between tip and sample, z, is taken into account, $\rho(\vec{r}_0, E_F)$ can be transformed to

$$\rho(\vec{r}_0, E_F) = \rho(z, E_F) = \rho(z{=}0, E_F) \cdot e^{-2\kappa z} \tag{2.10}$$

with B being the height of the barrier and κ being the inverse decay length, defined as:

$$\kappa = \sqrt{\frac{2mB}{\hbar^2}} \tag{2.11}$$

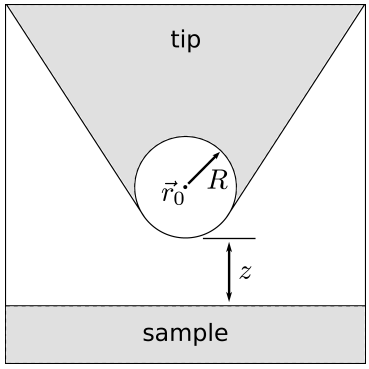

Figure 2.2. *Schematic representation of the tip-sample configuration used in the Tersoff-Hamann model. The tip is approximated to be of spherical shape having a radius of curvature R with its center at $\vec{r}_0$. During scanning tunneling microscopy experiments, the tip is brought into close proximity to the sample, with the distance between the apex of the tip and the surface of the sample being z.*

Hence, Equation 2.9 can be simplified to:

$$I \propto \rho(z{=}0) \cdot e^{-2\kappa z} \tag{2.12}$$

and further to:

$$I = I_0 \cdot e^{-2\kappa z} \tag{2.13}$$

When using scanning tunneling microscopy on metal samples, the approximation presented in Equation 2.9 is particularly applicable since the density of states of energies close to the Fermi energy is almost constant. In this case, the transmission of electrons through the vacuum barrier can be considered to not show a significant dependence on the energy of the states involved, as long as only small gap voltages are applied. For tunneling into a semiconductor, however, larger gap voltages are necessary to overcome the band gap. In this case, every single state with an energy between the Fermi energy of the sample and the Fermi energy of the tip contributes to the tunneling current. Furthermore, every state faces a different barrier height.

Using the Wentzel-Kramers-Brillouin approximation, the tunneling current for tunneling into a semiconductor can be written as the integral of all contributing

states [44], i.e. the states which are defined by the gap voltage V:

$$I \approx \int_0^{eV} \rho_s(z=0,\varepsilon) \cdot T(\varepsilon, eV, z, U) d\varepsilon \quad , \quad (\rho_t \approx \text{const.}) \tag{2.14}$$

where $T(\varepsilon, eV, z, U)$ is the transmission coefficient for an electron with energy E at a gap voltage V and a potential $U = E_F - E_V$ and the elementary electric charge, e, is supposed to be positive. According to Equation 2.13, the transmission coefficient strongly depends on the distance between tip and sample and can be approximated by:

$$T(\varepsilon, eV, z, U) = \exp\left(-\frac{2z\sqrt{2m}}{\hbar} \cdot \sqrt{\frac{\Phi_{\text{SC}} + \Phi_t}{2} + \frac{eV}{2} - \varepsilon}\right) \tag{2.15}$$

The term $\left(\frac{\Phi_{\text{SC}}+\Phi_t}{2} + \frac{eV}{2} - \varepsilon\right)$ is the effective barrier height with the work function of the semiconductor, Φ_{SC}, being defined as:

$$\Phi_{\text{SC}} = E_{\text{vac}} - E_F = \underbrace{E_{\text{vac}} - E_V}_{\chi + E_{\text{gap}}} + \underbrace{(E_V - E_F)}_{=-U} \tag{2.16}$$

As a consequence, the transmission coefficient and hence the tunneling current depend on the potential U.

2.2. Theory of the band structure

A more detailed understanding of the connection between tunneling current and the band structure of the sample and tip is required to interpret scanning tunneling microscopy images. Figure 2.3 shows the schematic band structure for a positive gap voltage being applied between the tip and a semiconductor[1]. If a positive gap voltage[2] is applied, electrons tunnel from the tip into the empty conduction band of the sample. The images acquired are thus called "empty state images".

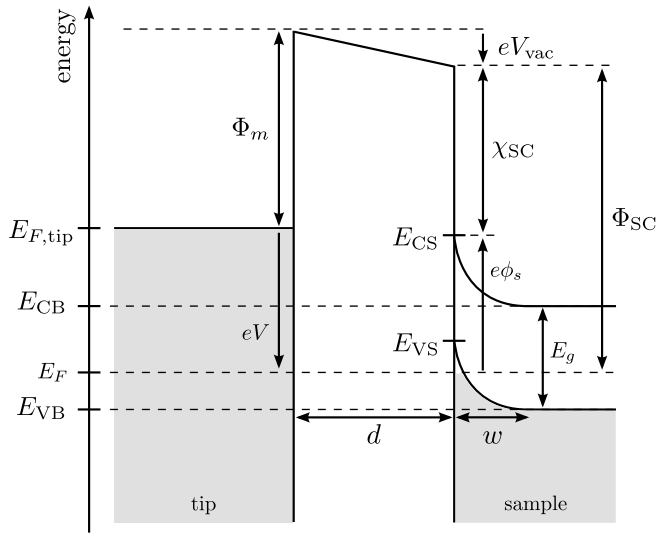

Figure 2.3. *Schematic band structure for a positive gap voltage[2] being applied between the tip and a semiconductor with definition of important parameters[1]. In the given case, electrons tunnel from the tip into the empty conduction band of the sample.*

[1] To enable a fast access to the detailed definition of the numerous prameters in this figure, they are listed in Chapter "Symbols" on page 135.
[2] The voltage is applied with the sample carrying the positive sign.

2.2.1. Fermi level

A very important quantity is the Fermi energy, also called Fermi level. The Fermi level is defined as the energy of the energetically highest state still occupied by electrons at temperature $T = 0\,\mathrm{K}$ in the state of equilibrium [45]. The Fermi level of a semiconductor can be determined by its net charge balance and vice versa. For a semiconductor in a state of equilibrium, the net charge balance is:

$$n + N_a^- = p + N_d^+ \tag{2.17}$$

where the concentration of negative charges due to electrons, n, and ionized acceptors, N_a^-, has to be equal to the concentration of positive charges caused by holes and ionized donors, p, N_d^+, respectively. The balance is determined by the energetic position of the Fermi level, E_F. According to Sze [46], the concentrations of electrons and holes are:

$$n = N_C \cdot \frac{2}{\sqrt{\pi}} \cdot F_{1/2}\left(\frac{E_F - E_C}{k_B T}\right) \tag{2.18}$$

$$p = N_V \cdot \frac{2}{\sqrt{\pi}} \cdot F_{1/2}\left(\frac{E_V - E_F}{k_B T}\right) \tag{2.19}$$

with E_C being the energy at the bottom of the conduction band and E_V being the energy at the top of the valence band. N_C and N_V are the effective density of states in the conduction band and in the valence band, respectively. They are defined as:

$$N_C = 2 \cdot \left(\frac{2\pi m_n^* k_B T}{h^2}\right)^{\frac{3}{2}} \tag{2.20}$$

$$N_V = 2 \cdot \left(\frac{2\pi m_p^* k_B T}{h^2}\right)^{\frac{3}{2}} \tag{2.21}$$

with m_n^* and m_p^* being the effective mass for electrons and holes, respectively. $F_{1/2}(x)$ is the Fermi-Dirac integral given by:

$$F_{1/2}(x) = \int_0^\infty \frac{\eta^{1/2}}{1 + e^{\eta - x}} \mathrm{d}\eta \tag{2.22}$$

The concentrations of ionized donors and ionized acceptors are:

$$N_d^+ = N_D \cdot \frac{1}{1 + 2 \cdot e^{\frac{E_F - E_D}{k_B T}}} \tag{2.23}$$

$$N_a^- = N_A \cdot \frac{1}{1 + 2 \cdot e^{\frac{E_A - E_F}{k_B T}}} \tag{2.24}$$

where E_D and E_A are the energy levels of donors and acceptors, respectively, N_D is the concentration of donors and N_A that of acceptors.

2.2.2. Tip-induced band bending

When metal tips are used for the investigation of semiconductors by scanning tunneling microscopy, two materials with (very) different work functions, Φ_m for the metal tip and Φ_{SC} for the semiconductor, are brought into close proximity. If the gap is small enough, electrons will tunnel from the material featuring the energetically lower work function into the other material. With every electron being transferred, the charge balance changes slightly, which consequently requires an adaption of the Fermi level of both materials. After a certain amount of electrons has been transferred from one material to the other one, the energetic positions of the respective Fermi levels align and no further electrons will be transferred. Due to the changed charge balance, neither material is electrically neutral anymore, which causes the built up of an electric field, ξ_{vac}, within the gap. This field is screened by free electrons in the metal and by free carriers due to dopants, defects or ionized surface states in the semiconductor. While the effective length of screening in the metal is the Thomas-Fermi screening length, the space charge region, w, in the semiconductor is much more extended.

When additionally applying a gap voltage V, the difference in the electrostatic potentials, V_{vac}, shifts the energetic positions of the surface of the conduction band, E_{CS}, and the surface of the valence band, E_{VS}. The difference in the electrostatic potentials can be written as:

$$V_{\mathrm{vac}} = \xi_{\mathrm{vac}} \cdot d \tag{2.25}$$

with d being the separation of tip and sample. The difference of the work functions is also known as the contact potential:

$$\begin{aligned} \Delta\Phi &= \Phi_m - \Phi_{\mathrm{SC}} && (2.26)\\ &= \Phi_m - \chi_{\mathrm{SC}} - (E_{\mathrm{SC}} - E_F) && (2.27) \end{aligned}$$

where χ_{SC} is the electron affinity of the semiconductor and the magnitude of the barrier potential ϕ_s is related to the charge density ρ by Poisson's equation, which, for the one-dimensional case, can be written as:

$$\frac{\mathrm{d}^2\phi(x)}{\mathrm{d}x^2} = -\frac{\rho(x)}{\varepsilon\varepsilon_0} \tag{2.28}$$

with ε and ε_0 being the dielectric constant of the semiconductor and the permittivity in vacuum, respectively.

As a result, the shifted energetic positions of the surface of the conduction band, E_{CS}, and the surface of the valence band, E_{VS}, are:

$$\begin{aligned} E_{\mathrm{CS}} &= E_{\mathrm{CB}} - (E_g + E_F) + e\phi_s && (2.29)\\ E_{\mathrm{VS}} &= E_{\mathrm{VB}} - (E_g + E_F) + e\phi_s && (2.30) \end{aligned}$$

where E_g denotes the energy of the band gap and E_{CB} and E_{VB} are the energetic positions of the valence band edge and the conduction band edge, respectively, in the bulk material.

3. Properties of wurtzite gallium nitride

Gallium nitride (GaN) is a group III-nitride semiconductor which typically crystallizes in the wurtzite structure[1]. The lattice parameters of the hexagonal crystal structure of wurtzite GaN at a temperature of $T = 300\,\mathrm{K}$ are $a = 3.189\,\text{Å}$ and $c = 5.185\,\text{Å}$ [1]. GaN has a wide direct band gap of 3.51 eV [1] at a temperature of 0 K. At room temperature, the band gap is approximately 3.4 eV, as resulting from the empirical formula by Varshni [47] shown in Equation 3.1 with a temperature $T = 300\,\mathrm{K}$ and α and β being 0.909 meV/K and 830 K, respectively [1]:

$$E_g(T) = E_g(0) - \frac{\alpha \cdot T^2}{T + \beta} \tag{3.1}$$

The most important crystal planes in wurtzite GaN are presented in Table 3.1.

Plane	**Index**	**Polarity**
c-plane	(0001)	polar
a-plane	$(11\bar{2}0)$	nonpolar
m-plane	$(10\bar{1}0)$	nonpolar
r-plane	$(1\bar{1}02)$	semipolar

Table 3.1. *Miller indices of the most important crystal planes in wurzite GaN. The samples investigated for this thesis were cleaved along the nonpolar m-plane.*

The c-plane exhibits the hexagonal characteristics of the wurtzite structure. When cleaving wurtzite GaN perpendicular to its c-plane, the resulting surface may be

[1] GaN can also exhibit the zinc blende structure, however, the only stable structure for GaN is the wurtzite structure.

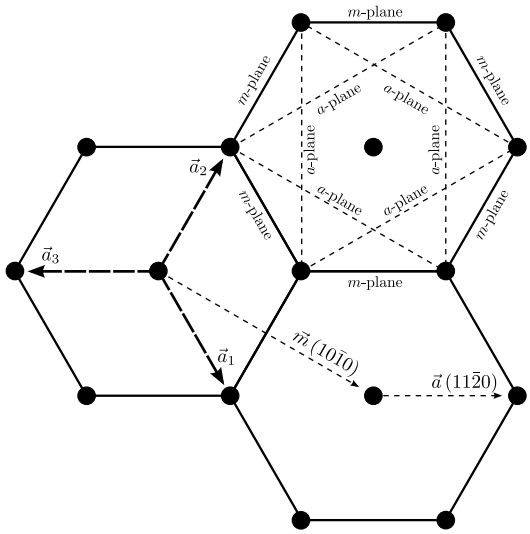

Figure 3.1. *Definition of lattice vectors perpendicular to the c-axis of wurtzite GaN (superlattice). The three unit vectors within the c-plane are $|\vec{a}_1| = |\vec{a}_2| = |\vec{a}_3| = a$ in length with $a = 3.189\,Å$. The fourth unit vector is $c = 5.185\,Å$ in length [1]. As a result to the hexagonal structure, there are six m-planes and six a-planes, whose intersection lines with the c-plane are indicated by dashed lines. The angle between planes of the same type is $n{\cdot}60°$, whereas the angle between two planes of different types is $(2n{+}1){\cdot}30°$.*

either an a-plane or an m-plane. Despite both types of surface being nonpolar, experiments show that GaN prefers to expose an m-type surface [48]. Important parameters of the structure of wurtzite GaN are shown in Figure 3.1. As a result of the hexagonal structure, there are six m-planes and six a-planes (intersection lines with c-plane in Figure 3.1). The angle between planes of the same type is $n{\cdot}60°$, whereas the angle between two planes of different types is $(2n{+}1){\cdot}30°$.

The surface structure of the a-plane and the m-plane in side and top view as well as the corresponding surface Brillouin zones are depicted in Figure 3.2. On both the a and the m-plane, the N surface anions relax outward into the vacuum relative to the Ga cations [49]. GaN wurtzite structure cleavage surfaces exhibit an occupied as well as an empty state above the N anion and the Ga cation,

respectively. A charge transfer from the Ga dangling bond to the N dangling bond occurs. The most important points in both Brillouin zones are the $\bar{\Gamma}$, $\bar{X}$, $\bar{M}$ and the $\bar{X}'$ points.

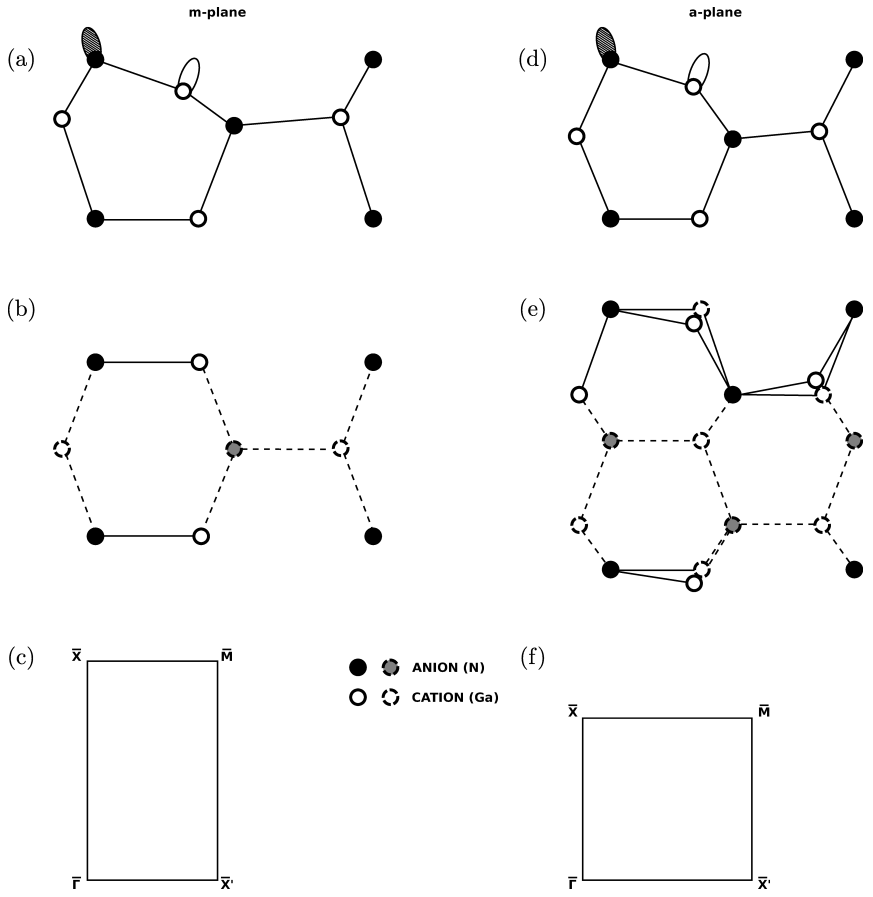

Figure 3.2. *Surface structure and definition of important points in the GaN surface Brillouin zones according to Wang [50]. (a) m-plane side-view showing filled N (striped) and empty Ga dangling bonds. (b) m-plane top-view. (c) m-plane surface Brillouin zone. (d) a-plane side-view. (e) a-plane top-view. (f) a-plane surface Brillouin zone. The most important points in both Brillouin zones are the $\bar{\Gamma}$, $\bar{X}$, $\bar{M}$ and the $\bar{X}'$ points.*

4. Experimental techniques

4.1. Preparation of samples

Rectangular samples with a width and height of approximately 3 mm and 7 mm, respectively, were cut from a gallium nitride wafer. For a better cleavage, the samples were thinned and polished using a grinding machine until a thickness of less than 100 µm was attained, as can be discerned from the cross-sectional view in Figure 4.1(c). To improve the conductivity of the contact of sample and specimen holder, a layer of gold was sputtered onto the sample surface ($\pm c$-plane), as can be discerned as a golden layer at both ends of the sample shown in Figure 4.1(b). The layer of gold and the sample were joined by applying short pulses of current to the interface of the two materials.

To create a predetermined breaking point on the sample, a diamond tip was indented into the surface creating a small indented spot and a crack. Predetermined breaking spots like these were inserted approximately every 500 µm forming a straight line across the sample. Two of these indented spots are shown in Figure 4.1(a). Afterward, the sample was glued onto a cube of metal in such a matter, that one third of the sample at most was in contact with the metal cube using a conducting glue that contains large amounts of silver. This cube was then mounted to a specimen holder which was inserted into the vacuum chamber. To cleave the sample *in situ*, its non-attached part was forced against a firm overhang. This way, the bending force applied to the crystal initiated cleavage, preferably at the indented spots, resulting in a clean and atomically flat surface. A sample with the cleaved part still attached to the sample holder by excess glue is shown in Figure 4.1(b). The cleaved surface is shown as a top-view in Figure 4.1(c) and a side-view in Figure 4.1(d).

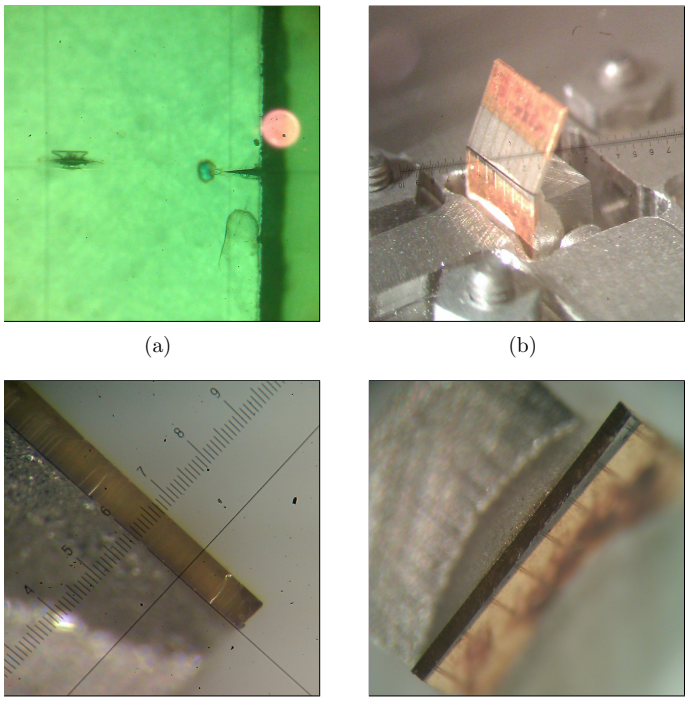

(a) (b)

(c) (d)

Figure 4.1. *Preparation of samples. To create a predetermined breaking point on the sample, a diamond tip is indented into the surface creating small indented spots and cracks (a). To cleave the sample in situ, it is attached to a metal cube, transferred into the preparation chamber of the STM where the part is forced against a firm overhang. This way, the bending force applied to the crystal initiates cleavage (b), preferably at the indented spots, resulting in a clean and atomically flat surface (c)[1] and (d).*

4.2. Preparation of tips

Tungsten tips were used for all experiments. For the preparation of the tips, a tungsten wire with a diameter of 0.25 mm is inserted into a flat droplet of sodium hydroxide solution, suspended in a ring of platinum wire. Additionally, a constant voltage is applied between platinum wire and the tungsten wire with the latter one having a positive bias. With a distinctive frequency of approximately one Hertz, the sign of the voltage is reversed for a short time, creating small pulses. In this matter, the surface of the tungsten wire is cleaned, resulting in an enhancement of the etching. The actual process of etching occurs while the tungsten wire has a positive bias:

$$\begin{aligned} \text{anode} &: \mathrm{W}_{(s)} + 8(\mathrm{OH})^- \rightarrow \mathrm{WO}_4^{2-} + 4\mathrm{H_2O} + 6e^- \\ \text{cathode} &: 6\mathrm{H_2O} + 6e^- \rightarrow 3\mathrm{H}_{2(g)} + 6(\mathrm{OH})^- \\ \text{total} &: \mathrm{W}_{(s)} + 2(\mathrm{OH})^- + 2\mathrm{H_2O} \rightarrow \mathrm{WO}_4^{2-} + 3\mathrm{H}_{2(g)} \end{aligned}$$

4.3. Correction of nonlinear distortions in STM images

This study uses large scale scanning tunneling microscopy images with several micrometes in size like the one shown in Figure 4.2. Scanning tunneling microscopes usually position their tip utilizing piezo-crystal tubes, whose application requires a calibration of their lateral and vertical positioning. Since scanning tunneling microscopes are mainly used for imaging surfaces with atomic resolution, the calibration of the piezo-crystals is optimized for ranges between one and a few hundred nanometers. Due to the large scale of the images acquired within this study, the parameters used to perform the measurements exceed the designated linear range of the calibration. This results in the occurrence of a variety of nonlinear effects of the piezo-crystals such as hysteresis creep, drift, and a nonlinear dependence of the displacement on the applied voltage, which, in most cases, causes distortions of the image [51].

[1]The scale is an internal light microscope measuring unit which is to be disregarded.

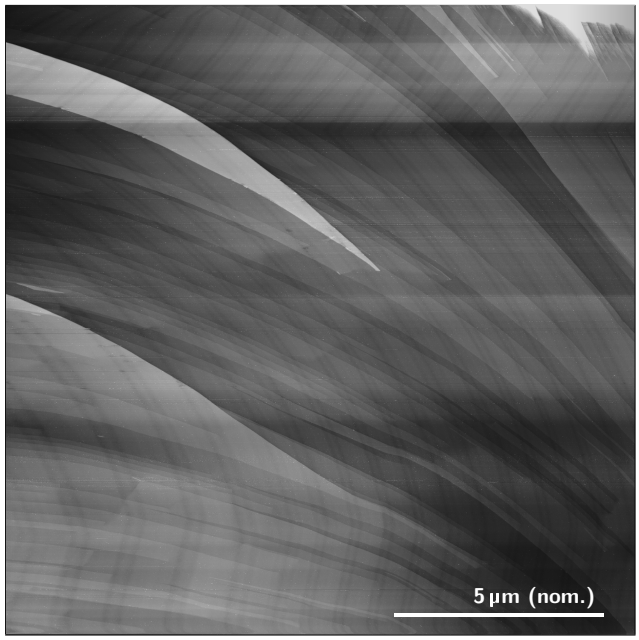

Figure 4.2. *Measurement of a GaN epitaxial layer with a nominal size of* $15\,\mu m \times 15\,\mu m$*. Without further information, neither can actual distortions be discerned from the image, nor is it possible to determine the real size of the area having been investigated.*

By using a calibration sample, a fast and reliable method for correcting nonlinear distortions *after* the measurement was developed within this study[2]. The sample was designed to exhibit regular nanostructures with a great accuracy concerning the distances between the features. The underlying idea was to investigate the calibration sample while utilizing many different sets of parameters, in particular those usually used within the actual measurements. Due to the knowledge of the actual geometry of the sample, a displacement tensor can then be computed after having measured a distorted image of the surface [52]. Applying the inverse of this tensor to any image acquired using the same set of parameters facilitates the correction of the image. The main advantage of this method is the ability to easily

[2]The calibration sample was produced by D. Weber, S. Trellenkamp, R. Borowski, and L. Jin according to set requirements.

correct various distortions without knowing their origin or having a quantitative description thereof. However, this procedure has to be re-performed for every individual scanning tunneling microscope.

4.3.1. The calibration sample

The substrate of the calibration sample was a Nb:$SrTiO_3$ single crystal. This material was chosen not only because of its resistance to oxidation or to degradation up to very high temperatures, but also because of its nature as an n-type semiconductor with a band gap of about 3 eV and resulting comparable properties to GaN, as well as the intrinsic chemical resistance of the compound. The dots were made of Ti due to its excellent adhesion to $SrTiO_3$, where it oxidizes to TiO_2, which in turn is electronically very similar to Nb:$SrTiO_3$ and ensures a good charge transfer even in case of oxidation. Both metal and oxide are mechanically stable without exhibiting any surface oxidation in most mediums. The application of lift-off and electron beam lithography enable the achievement of a high resolution of the pattern, with the electron beam writer ensuring a positioning accuracy of better than 5 nm on a 320 µm × 320 µm field. Hence, the error of the dot pitch of 1% is much smaller than the distortion created by piezo nonlinearities and is therefore neglected in the following. The patterned dots are approximately 10 nm in height and are arranged as shown in Figure 4.3(b). The vertical and lateral spacing between the dots is 500 nm. Every fifth dot has a more pronounced size and every tenth dot is replaced by four dots forming a small dotted square. This enables the determination of the position of the tip.

4.3.2. Correction of distortions

Without knowing details of the sample structure, the image presented Figure 4.2 appears to be a normal scanning tunneling image and distortions cannot be identified. To gain an understanding of the distortions occurring during the acquisition of large images on the employed scanning tunneling microscope, the calibration sample prepared as described in Section 4.3.1 was investigated. The scanning tunneling image acquired from the calibration sample is shown in Figure 4.3(a). According to the STM data, the image supposedly has a size of 10 µm × 10 µm.

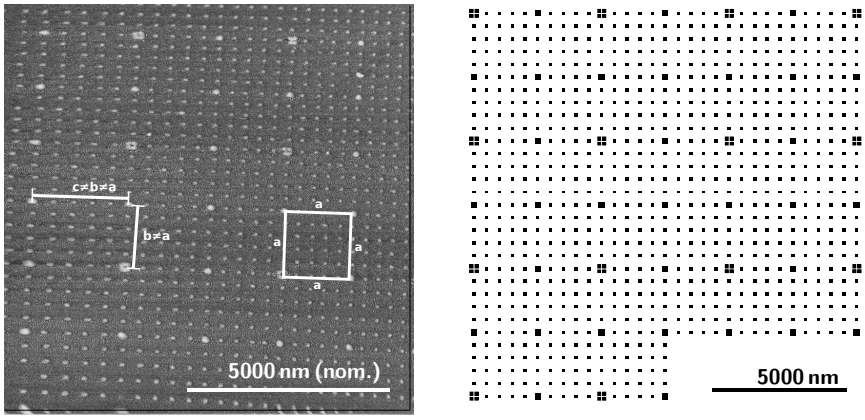

(a) Distorted STM image (b) Calibration pattern

Figure 4.3. *STM image of the calibration sample with a nominal size of 10 µm × 10 µm (a). Counting the dots and considering their real distance of 500 nm as shown in (b), however, results in a real size of about 12.5 µm width and 15 µm height for the image in (a). While the discrepancies in size are a result of distortions, the slight rotation of the grid in (a) is merely due to inaccuracies of the sample holder and the process used to fix the sample to it. The marked square in (a) has an actual edge length of a = 2500nm.*

Counting the dots visible in the image, however, and computing the size from the spacing between the dots of 500 nm reveals that the analyzed area is actually 12.5 µm × 15 µm in size. The original pattern of the calibration sample has a squared geometry where any six horizontally and six vertically neighboring dots form 6×6 dot squares with an edge length of $a = 2500$ nm. While the dots located at the lower right hand side of the measurement in Figure 4.3(a) maintain the squared geometry, dots on the left hand side are displaced, with 6×6 dot areas forming a rectangle with neither of the two pairs of edges b and c being equal to a and c being greater than b. These results denote a bigger distortion of the image in the horizontal direction than the vertical one. Furthermore, the apparent horizontal dot separation in the lower left part of the image is almost twice the dot separation in the upper right part, therefore not only showing a difference between horizontal and vertical distortion but also a dependency on the position within the

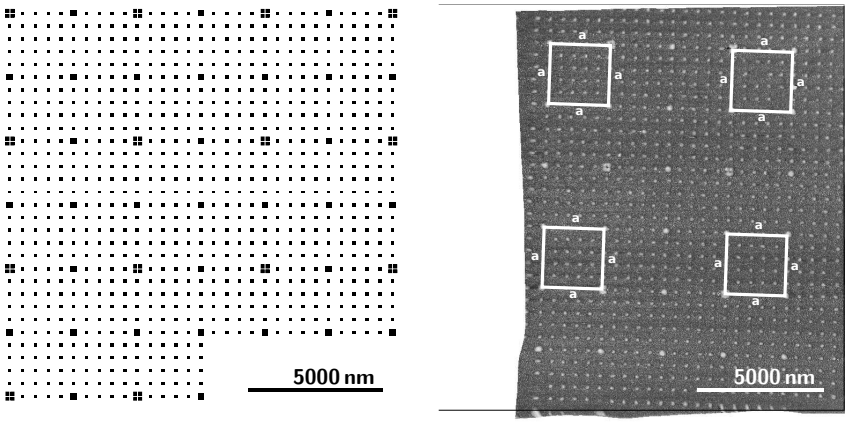

(a) Calibration pattern (b) Corrected image

Figure 4.4. *(a) Calibration pattern. (b) Corrected image. Each 6 × 6 dot area now forms a square with the same edge length as the pattern in Figure 4.4(a). The image seems to be horizontally compressed compared to the raw STM image in Figure 4.3(a).*

image. The experiments revealed that distortion does not primarily depend on the scan speed or movements of the piezo tube that have been performed prior to the scanning of the image, while the size of the scan area as well as its rotation angle do affect the distortions most significantly.

With the aim of correcting the distortions, the displacement of the dots in Figure 4.3(a) has been quantified using a custom software developed within the research group [52, 53]. After analyzing the distorted image, a tensor containing the quantified distortion could be computed, which, henceforward, was used to correct the distorted images. The corrected image of the calibration sample is shown in Figure 4.4(b), demonstrating that each 6×6 dot area now forms a square with the same edge length as the pattern in Figure 4.4(a). Due to the predominance of distortions in the horizontal direction, the corrected image seems to be horizontally compressed as compared to the raw STM image in Figure 4.3(a).

This procedure has been performed with a large variety of different scanning parameters so as to be able to compute as many different distortion tensors as possible. In this matter, every image used for this study was corrected using an

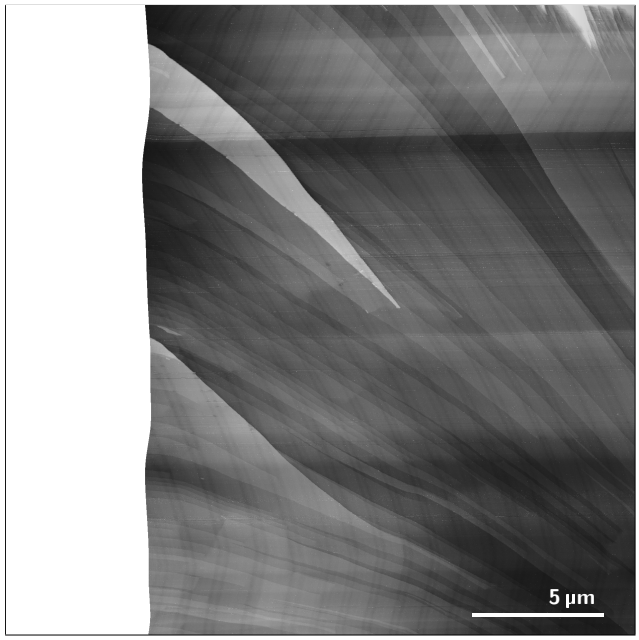

Figure 4.5. *Corrected image. The image presented in Figure 4.2 has been corrected using an appropriate distortion tensor as obtained by probing the calibration sample with the exact same parameters as used for the measurement of this STM image. The square image in Figure 4.2 has a nominal with of 15 µm. The corresponding square frame surrounding Figure 4.5 which results from the correctional calculations, however, has a width of about 24 µm, proving that Figure 4.2 is actually covering an area much larger than reported by the software controlling the measurement. Additionally, the corrected image does not retain a squared geometry, representing the fact, that the distortions in horizontal (x) and vertical (y) direction differ significantly.*

appropriate distortion tensor.

The significant changes resulting from the application of the correction algorithm to the acquired STM raw images and resulting importance of performing said correction process is demonstrated in Figure 4.5, displaying the corrected version of the image presented in Figure 4.2. Figure 4.2 has been corrected using a distortion tensor obtained by probing the calibration sample with the exact same scanning parameters as used for the acquisition of the image. While Figure 4.2

has a nominal width of 15 µm, the square frame surrounding Figure 4.5 which results from the calculations[3], however, has a width of about 24 µm, proving that Figure 4.2 is actually covering an area much larger than reported by the software controlling the measurement. Additionally, the corrected image does not retain a squared geometry, representing the fact that the distortions in horizontal and vertical direction differ significantly.

The presented methodology results in a significant improvement of accuracy of measurements of distance and angle in large scanning tunneling images.

[3]Further details and explanations concerning the algorithm used for the computation of the distortion tensor can be found in [52]: M. Schnedler, P. H. Weidlich, V. Portz, D. Weber, R. Dunin-Borkowski, and Ph. Ebert. "Correction of nonlinear lateral distortions of scanning probe microscopy images". In: *Ultramicroscopy* **136** (2014), 86–90.

5. Experimental details

5.1. Experimental details of Part II

For both the initial and the modified experiment, free-standing n-type GaN samples with a nominal average dopant concentration of $(1{-}5) \times 10^{18}\,\mathrm{cm}^{-3}$ were used. After having been prepared as presented in Chapter 4, they were cleaved in ultra high vacuum with a pressure of approximately $1 \times 10^{-8}\,\mathrm{Pa}$ in order to expose a clean and stoichiometric $(10\bar{1}0)$ surface. Immediately after the cleaving process, the samples were cooled to 77 K and investigated by an Omicron LT-STM equipped with tungsten tips. The samples are shown in Figure 5.1.

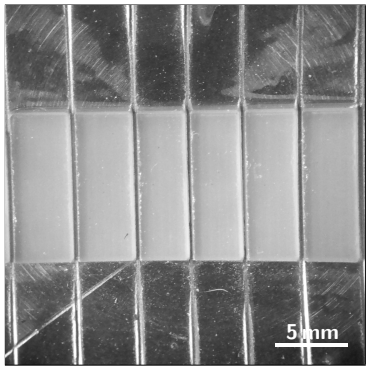

Figure 5.1. *(a) GaN samples with a nominal dopant concentration of* $(1-5) \times 10^{18}\,cm^{-3}$*. They were cleaved in ultra high vacuum with a pressure of approximately* $1 \times 10^{-8}\,Pa$ *in order to expose a clean and stoichiometric* $(10\bar{1}0)$ *surface.*

5.2. Experimental details of Part III and Part IV

Gallium nitride samples with n-doped GaN epitaxial layers (n-type dopant concentration of approximately $1{\times}10^{17}$ to $5{\times}10^{18}\mathrm{cm}^{-3}$) were prepared for the investigation according to the procedure described in Chapter 4. The samples were cleaved in ultrahigh vacuum ($1{\times}10^{-8}$ Pa) along a $(10\bar{1}0)$ m-plane and the orientation of the wafer was determined by Laue diffraction measurements as shown in Figure 5.2(a).

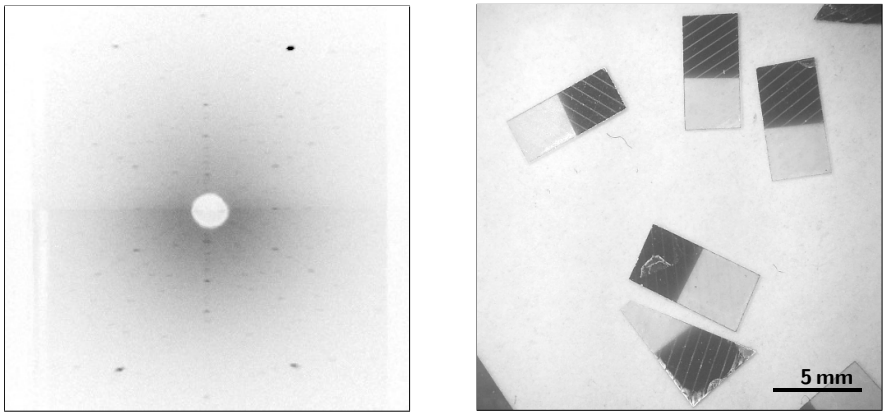

(a) Laue diffraction image (b) Characteristic samples

Figure 5.2. *Sample preparation: (a) Representative Laue diffraction image of the uncleaved wafer recorded for the determination of the orientation of the crystal lattice. (b) Prepared samples (gold sputtered) before cleavage.*

For the actual measurements, a variable temperature Omicron STM equipped with electro-chemically etched tungsten tips was used and operated at room temperature[1]. After *in situ* cleavage, the freshly exposed cross-section of the m-plane was widely flat and free of defects. As a consequence, large scale scanning tunneling images could be acquired. These images were corrected as depicted in Chapter 4 to minimize nonlinear distortions induced by the increased movements due to the large scan area.

[1]For the preparation of the tungsten tips, see Section 4.2.

Part II.

Hidden surface states at GaN $(10\bar{1}0)$ surfaces

6. Introduction

For cross-sectional scanning tunneling experiments, the GaN freestanding wafers and epitaxial layers are cleaved on m-planes ($(10\bar{1}0)$ surfaces). To interpret the experimental data, it is important to know the electronic and geometric structure in detail. The m-planes are also highly relevant for GaN nanowires, since nanowires exhibit an extremely high surface-to-volume ratio as compared to conventional semiconductor devices. Consequently, surface-induced effects dictate many properties of nanowires. The distribution of dopants and hence the distribution of potential in particular is largely affected by surface states. If surface states within the fundamental band gap of sidewall facets of the nanowire were present, they might even lead to paths of non-radiative recombination and thus reduce quantum efficiency. According to Bertness [54] and Largeau [55], the non-polar m- and a-plane sidewall facets are the most important surfaces for wurtzite structure group III-nitride nanowires. Despite its great importance, the electronic structure of the GaN $(10\bar{1}0)$ m-plane surface has not been sufficiently investigated yet. Particularly, the presence of a surface state within the fundamental band gap is controversially being discussed and hence its influence on the electronic properties of nanowires remains unknown [56].

Calculations using density functional theory within the local density approximation predict the presence of two surface states shifted out of the fundamental band gap [57, 58]. Recent density functional theory calculations based on modified pseudopotentials, however, predict the upper (empty) surface state to be within the fundamental band gap for any point in the first Brillouin zone [59, 60]. Experimental techniques like scanning tunneling microscopy (STM), however, were not able to probe any of the surface states in the band gap [58, 61].

In this PART, the results of *ab initio* calculations, as presented in Chapter 8, are used to obtain a set of experimental parameters to successfully probe the empty

gallium surface state by conducting a modified scanning tunneling microscopy experiment. The modified experiment and its results are presented in Chapter 9.

Contents of PART II have recently been published in [62]: L. Lymperakis, P. H. Weidlich, H. Eisele, M. Schnedler, J.-P. Nys, B. Grandidier, D. Stievenard, R. E. Dunin-Borkowski, J. Neugebauer, and Ph. Ebert. "Hidden surface states at non-polar GaN $(10\bar{1}0)$ facets: Intrinsic pinning of nanowires". In: *Applied Physics Letters* **103** (2013), 152101.

7. Initial experiment

7.1. Experimental results

The *in situ* cleaved surfaces predominantly consisted of large terraces of up to several micrometers in size. These GaN $(10\bar{1}0)$ terraces were separated by steps with a height of one to three monolayers (ML). Such a step, separating two terraces, is shown in inset (a) next to its averaged height profile across the step in Figure 7.1. The terraces exhibited a 1×1 reconstruction as visible in inset (b) of Figure 7.1. This is in good accordance with theoretical calculations and prior STM images of GaN [58] and other wurtzite structure compound semiconductor m-plane cleavage surfaces [63].

In addition to imaging the terraces, scanning tunneling spectra (STS), $I(V)$, as well as conductivity spectra, $\mathrm{d}I(V)/\mathrm{d}V$, were acquired on the terraces. The latter spectra are also known as *differential conductivity* spectra. The normalized conductivity can be defined as:

$$\text{normalized conductivity} = \frac{\mathrm{d}I}{\mathrm{d}V}\Bigg/\left\langle\frac{I}{V}\right\rangle \tag{7.1}$$

where, for simplicity, $I(V)$ is replaced by I. To obtain the differential conductivity, either the total current $I(V)$ can be numerically differentiated as a function of V or, if available, it can be directly measured by extracting the amplitude (and phase) from the signal of a Lock-In amplifier. The differential conductivities presented in this Chapter have been measured using such a Lock-In amplifier. The normalized differential conductivity is shown in Figure 7.2.

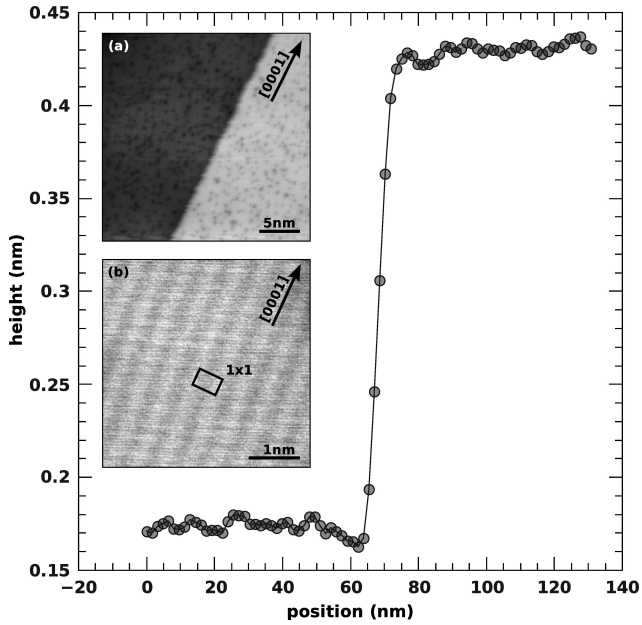

Figure 7.1. *Averaged height profile across the step shown in inset (a). The height of the step shown is one atomic layer. Nearly all terraces measured in various areas of the sample were separated by steps between one and three monolayers in height. Inset (a): STM image of an n-type GaN*$(10\bar{1}0)$ *surface measured at +4.26 V and 5 pA showing two large terraces separated by a monoatomic step. Inset (b): High resolution STM image of an n-type GaN*$(10\bar{1}0)$ *surface measured at +3.0 V and 200 pA showing a* 1×1 *reconstruction.*

7.2. Discussion of the tunneling spectra

According to Feenstra [64] and Tersoff *et al.* [43], the differential conductivity $\mathrm{d}I(V)/\mathrm{d}V$ is directly proportional to the density of states:

$$\frac{\mathrm{d}I(V)}{\mathrm{d}V} \propto \rho^S(\vec{r_0}, E_F) \tag{7.2}$$

with $\rho^S(\vec{r_0}, E_F)$ being the density of states of the sample at the position of the tip $\vec{r_0}$. In the present case, however, the interpretation is not that simple. At negative

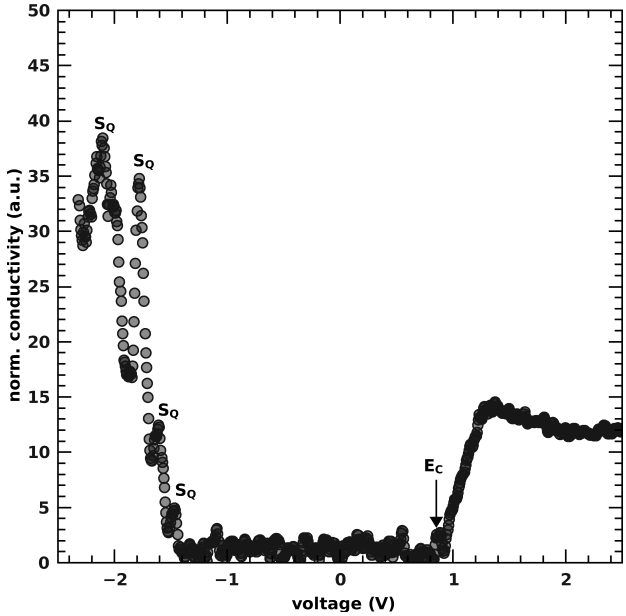

Figure 7.2. *Normalized differential conductivity spectrum measured at 77 K. The tip-sample separation z was kept constant by applying a set voltage V_{set} of +2.8 V and a set current of I_{set} = 150 pA. At negative voltages a number of peaks S_Q occur, which arise from quantized states confined within the zone of tip-induced band bending below the position of the tip. No intrinsic surface states can be observed in the GaN band gap.*

voltages well within the band gap of n-type GaN, a few peaks labeled S_Q are visible. They arise from quantized states confined within the zone of tip-induced band bending below the position of the tip [65, 66]. Since these states do not directly contain information on the band edges, they will not be investigated. Empty states, however, are of great interest. As can be seen in Figure 7.2, the onset of the current due to the empty states of the conduction band is at approximately +0.9 V which is in good accordance with the previous STS data on GaN $(10\bar{1}0)$ surfaces [58, 61] and can be related to the minimum of the bulk conduction band, E_C [58, 61]. The absence of a detectable current below the onset of the current into the conduction band suggests that there are no intrinsic surface states present within

the fundamental band gap. These initial results seem to support the calculations which predict the absence of said surface states [57, 58].

8. Ab initio calculations

8.1. Calculation method

For a more thorough characterization of the electronic structure of the experimentally probed m-plane GaN surface (shown in Figure 8.1), first principle calculations within density functional theory (DFT) using the local density approximation (LDA) and the projector augmented wave approach (PAW) [67, 68] have been performed by L. Lymperakis at the *Max-Planck-Institut für Eisenforschung* in Düsseldorf, Germany. Within the calculations, Ga semicore d-states have been explicitly treated as valence electrons and an on-site Coulomb interaction U for these states has been included [69]. This approach yields a fundamental band gap of 2.87 eV. Hence it significantly improves the absolute values of the calculated band gap compared to those computed by conventional functionals (2.2 eV for LDA and 1.67 eV for generalized gradient approximations, GGA [69]).

The initial calculations used a slab with 24 1×1 monolayers. Detailed conversion checks showed that thin slabs consisting of less than 24 MLs do not contain enough bulk-like material to correctly describe the onset of the current into the bulk conduction band [62]. Additionally, they cannot provide a dense mesh of bulk states, as can be seen by comparing the red stars (results of thin slabs) and blue dots (calculated with thick slabs, see below) in Figure 8.2(a). For this reason, thin slabs not only underestimate the density of states (DOS) at the energy region of interest but also fail to correctly describe the decay of the bulk band edge states into the vacuum [62]. In addition, they also suffer from a charge sloshing [70] along the slab preventing self-consistency of the electronic charge to be reached. Self-consistent calculations of thin slabs can be sped up by modifying and extending the approach originally developed by Engels *et al.* [71] in the following way: First, the charge density of a slab consisting of 24 MLs (i.e. $\approx$ 2.5 nm) is calculated

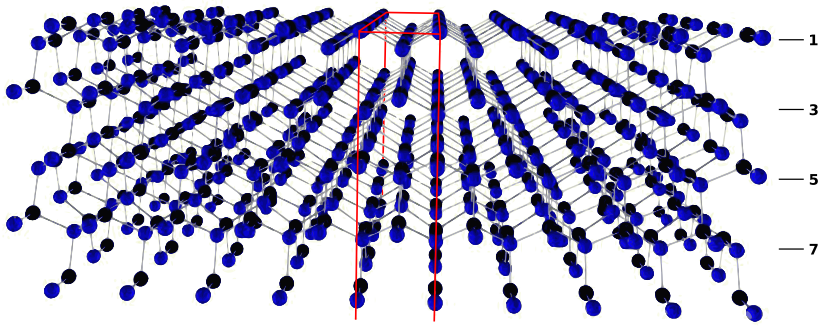

Figure 8.1. *Unrelaxed atomic structure of wurtzite-structure gallium nitride with an m-plane facing the top of the image. The upper part of the slab used in the calculations is indicated by red solid lines. The first four of 24 monolayers are visible and are labeled 1,...,4.*

self-consistently. Afterward, the slap is opened in the middle and additional 24 bulk like GaN MLs are inserted, yielding a slab with a thickness of 48 MLs (i.e. $\approx$ 5 nm). Second, non self-consistent calculations are performed by keeping the charge density fixed and using 187 k-points in the irreducible part of the surface Brillouin zone [62].

The results of this approach are shown in Figure 8.2(a). A comparison of the calculated red stars and blue dots with the projected bulk band structure (gray area) shows that this approach describes the bottom of the bulk conduction band with an accuracy of 0.15 eV[1].

[1] A more detailed analysis of the energetic position and dispersion of the surface state as well as of the decay of the states into the vacuum showed that this approach describes the dispersion and the decay with an accuracy better than 0.1 eV or 1%, respectively.

8.2. Surface states and dispersion

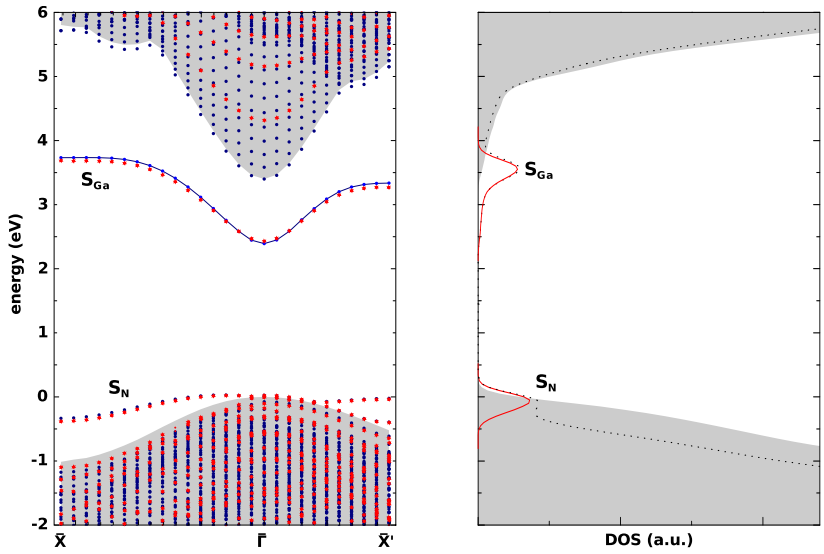

(a) (b)

Figure 8.2. *(a) Band structure of the relaxed GaN$(10\bar{1}0)$ surface along high symmetry lines of the surface Brillouin zone calculated with a slab consisting of 48 MLs (blue dots) and 12 MLs (red stars). The solid blue line indicates the Ga-derived unoccupied surface state (S_{Ga}). S_N denotes the N-derived occupied surface state. (b) Density of states of the 48 MLs slab (dotted line). The red solid curves indicate the DOS arising from the surface states. The grey shaded areas denote the projected bulk band structure (a) and DOS (b), respectively. In both cases, the top of the bulk valence band is set to 0 eV and the bulk conduction band has been rigidly shifted to meet the experimental band gap of GaN [62]. The high symmetry k points are defined according to Figure 3.2.*

Figure 8.2 shows the calculated band structure (a) and the corresponding density of states (b). As can be seen, the GaN $(10\bar{1}0)$ surface exhibits two noticeable states: A nitrogen-derived occupied state (S_N) at the top of the bulk valence band (E_V) at around 0 eV and a gallium-derived unoccupied s-type state (S_{Ga}) 2.4 eV above E_V. The empty gallium-derived surface state is within the fundamental band gap throughout the whole Brillouin zone and never is resonant with the bulk bands.

Surprisingly, this surface state apparently is not probed by conventional STM measurements.

A closer look at the dispersion in Figure 8.2(a) reveals that the energy of the unoccupied surface state exhibits a steep dependence on the parallel wave vector. A strong dispersion occurs at the $\bar{\Gamma}$ point while an almost flat dispersion can be observed near the edges of the Brillouin zone. This shape of the dispersion affects the density of states shown in Figure 8.2(b). The surface state exhibits a long tail with a low DOS decaying into the fundamental band gap, while the main peak overlaps with the onset of the bulk conduction band (projected bulk states shown in gray).

8.3. Decay of the DOS into the vacuum

Due to the fact that a scanning tunneling microscope probes the density of states far above the surface, the decay of the different states into the vacuum is of great importance. The extension of the states into the vacuum can be illustrated using the charge density distribution of two groups of states of different energetic positions: The energy of the first one is located at the onset of the surface state S_{Ga} (i.e. 2.4 eV above E_V), whereas states of the second group have an energy at the bulk conduction band edge E_C (i.e. 3.4 eV above E_V). The corresponding contour plots are shown in Figure 8.3. In both cases a localization at the Ga surface atoms is revealed, since the corresponding lobes extend furthest into the vacuum above the Ga sites. Surprisingly, the charge density arising from the states at $E_V + 3.4\,\text{eV}$ is much stronger and extends furthest into the vacuum. Hence, a scanning tunneling microscope will primarily probe states at the bulk conduction band minimum. The minimum of the surface state has only a very small contribution and hence is usually not visible in STM measurements. This is a direct consequence of the aforementioned strong dispersion of the surface state around the $\bar{\Gamma}$ point and the corresponding low tail of the density of states.

Despite having different energetic positions, the forecited two groups of states exhibit a similar decay into the vacuum, as can be seen in Figure 8.4 showing the partial charge densities integrated over the $(10\bar{1}0)$ plane. However, the states at the minimum of the bulk conduction band have an intensity more than two orders

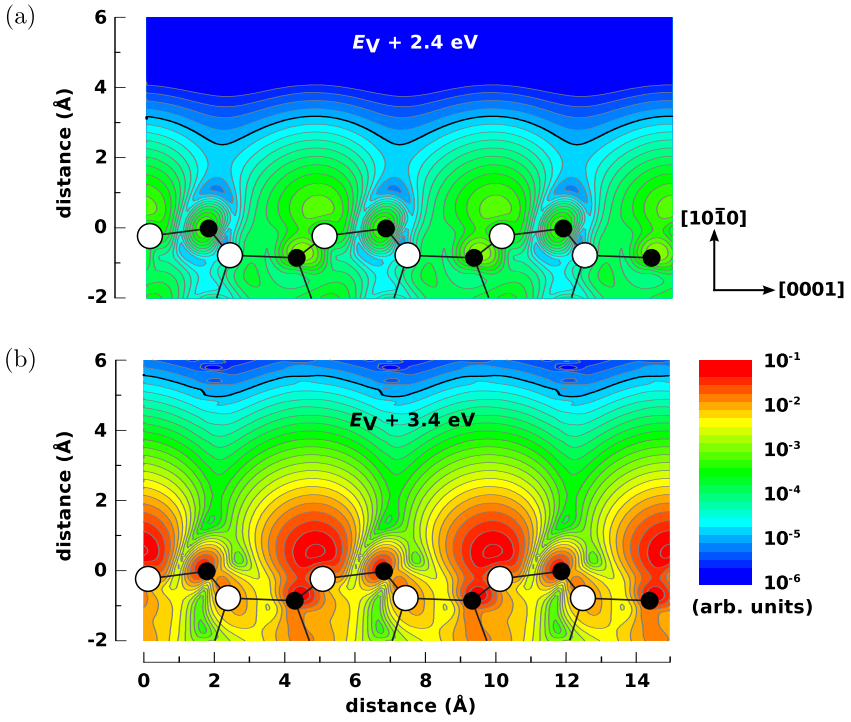

Figure 8.3. *Integrated partial charge density along the* $\langle 11\bar{2}0 \rangle$ *direction of the states at energies of (a)* $E_V + 2.4\,eV$ *(surface state onset) and (b)* $E_C = E_V + 3.4\,eV$ *(onset of bulk conduction band)[62]. In both cases, the partial charge density is the superposition of all states weighted with a Gaussian distribution with a standard deviation of* $25\,meV$ *centered at the corresponding energy value. The same logarithmic z-scale is used in (a) and (b). Thicker contour lines indicate isolines of the same value in (a) and (b). Open (filled) circles represent the Ga (N) atoms. As can be seen, the charge density arising from states at the onset of the bulk conduction band (b) extends further into the vacuum than the charge density of the surface state minimum (a), resulting in a preferential detection of states with energies at the minimum of the bulk conduction band.*

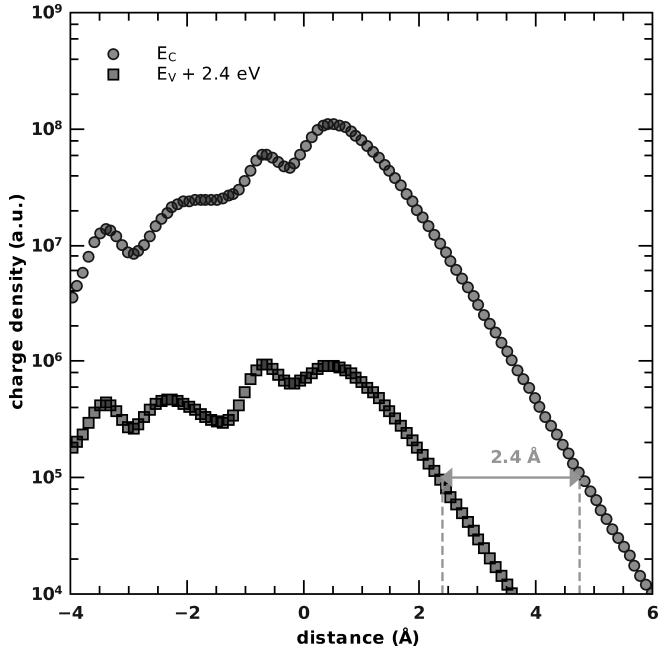

Figure 8.4. *Decay of the partial charge density integrated over the* $(10\bar{1}0)$ *planes arising from the states at the onset of* S_{Ga} *at* $E_V + 2.4\,eV$ *(squares) and those with energies at the bulk conduction band edge* E_C *(circles) [62]. The same Gaussian weighted superposition approach as used in Figure 8.3 has been applied.*

of magnitude higher than the intensity of states at the surface state minimum.

Furthermore, the decay of the surface state at different points of the Brillouin zone, as shown in Figure 8.5, shows that it is decaying slowest at the $\bar{\Gamma}$ point. At the edge of the Brillouin zone the decay is always faster and hence, at the $\bar{X}'$ and $\bar{M}$ points the DOS is negligible as compared to the DOS at the $\bar{\Gamma}$ point. At the $\bar{X}$ point, the DOS is still highest until an extrapolated distance of approximately 11 Å from the surface, due to the extremely flat dispersion of the surface state at the $\bar{X}$ point.

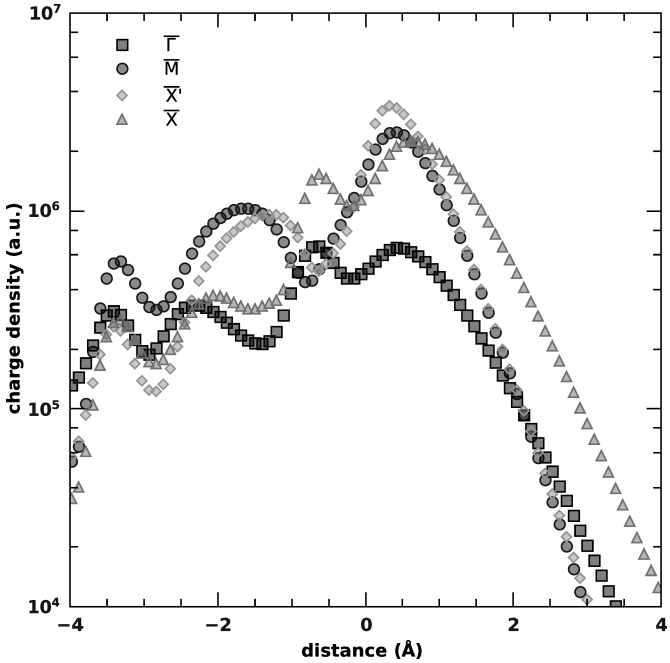

Figure 8.5. *Differences in the decay of the surface state for the high symmetry k-points of the surface Brillouin zone [62] as defined in Figure 3.2. The variations in the decay rates influence the strength of the signal when probing the surface in dependence on the separation of tip and sample. The topmost nitride surface atom is set to the distance of 0 Å within the calculations. Positive and negative values of the distance correspond to vacuum and bulk regions, respectively.*

As a result, the tip has to be approached[2] toward the surface by approximately 2.4 Å in order to probe equally strong signals for both states while measuring tunneling spectra, as can be seen by a smaller extent into the vacuum of the minimum of the surface state in Figure 8.3(a) or by looking at the separation of the dashed lines in Figure 8.4. According to these results, reducing the tip-sample separation should enable the detection of the empty S_{Ga} surface state.

[2]Due to Equation 2.9 ($I = I_0 \cdot e^{-2\kappa z}$), approaching the tip increases the tunneling current [64].

9. Experimental identification of the surface state

9.1. Modified experiment

As stated in Chapter 8.3 and shown in Figure 8.4, the tip has to be approached toward the surface in order to increase the sensitivity of the STM and hence be able to experimentally probe the minimum of the empty surface state S_{Ga}. In the experiment, the tip-sample separation hence has to be reduced. This has been achieved in two steps: First, the set current was increased from 150 pA to 200 pA and the set voltage was decreased from +2.8 V to +1.6 V to approach the tip by approximately 1.37 Å: To be able to determine the difference in tip-sample separation for these two sets of parameters, the tunneling spectrum measured at +2.8 V set voltage with constant tip-sample separation during the whole acquisition of the spectrum needs to be investigated. The tunneling current in this spectrum at a voltage of +1.6 V is 13 pA as shown in Figure 9.1. Hence, the same tip-sample separation could be adjusted using a set voltage of +1.6 V and a set current of 13 pA. Since the the tunneling current exponentially depends on the distance between tip and surface (Equation 2.9)[1], an increase in the set current from 13 pA to 200 pA (as used for the second spectrum) is equivalent to a reduction of the tip-sample separation Δz:

[1] $I = I_0 \cdot e^{-2\kappa z}$

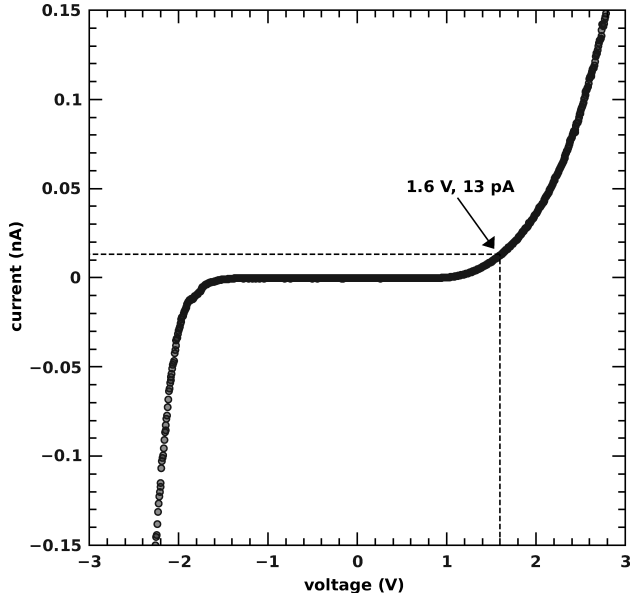

Figure 9.1. *Scanning tunneling spectrum acquired at 77 K, at a tip-sample separation defined by a setpoint of +2.8 V and 150 pA. A second spectrum (data not shown) has been measured at a distance resulting from a set voltage of +1.6 V and a set current of 200 pA. To compare the different tip-sample separations of the two spectra, the tip-sample separation resulting from the latter setpoint has to be determined using this spectrum and Equation 9.1. It follows that the tip is approached by 1.367Å using the setpoint of +1.6 V and 200 pA as compared to +2.8 V and 150 pA.*

$$\Delta z = -\frac{1}{2\kappa} \cdot \ln\left(\frac{I}{I_0}\right) \tag{9.1}$$

$$= -\frac{1}{2\kappa} \cdot \ln\left(\frac{200\,\mathrm{pA}}{13\,\mathrm{pA}}\right) \tag{9.2}$$

$$\approx -1.367\,\text{Å} \tag{9.3}$$

In a second step, the tip-sample separation has been further reduced by a ramp of

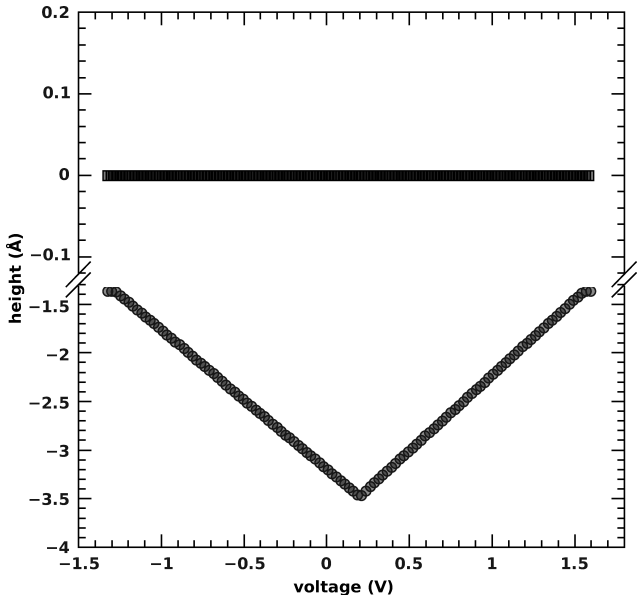

Figure 9.2. *Relative tip-sample separation for the two spectra shown in Figures 7.2 (upper line) and 9.3 (lower line). Performing the measurement using a constant gap voltage (upper line), which is the most common approach, results in the surface state not being probed. If, however, the tip-sample separation is modified (lower line) and the tip is hence approached up to 3.37 Å, the STM becomes more sensitive. Using this ramped tip-sample separation, the empty surface state S_{Ga} can be successfully probed.*

up to 2 Å as shown in Figure 9.2 instead of having a constant tip-sample separation. At the peak of the ramp, the tip is up to 3.37 Å closer to the surface. During the measurement, the tunneling current was always kept within the dynamic range of the pre-amplifier [72].

9.2. Experimental results and discussion

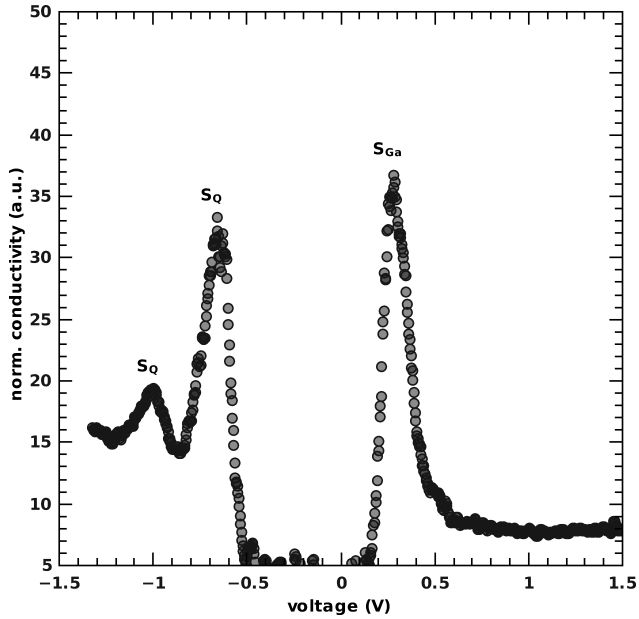

Figure 9.3. *Normalized differential conductivity spectrum measured at 77 K. The tip-sample separation z was varied by applying a ramp, as shown in Figure 9.2. The initial tip-sample separation was defined by a set voltage of +1.6 V and a set current of 200 pA. At negative voltages, peaks arise from quantized states S_Q confined in the zone of tip-induced band bending. The peak at approximately +0.25 V indicates the presence of a surface state roughly* 0.6 ± 0.2 *eV below* E_C.

The normalized conductivity spectrum measured with the reduced tip-sample separation is shown in Figure 9.3. In contrast to the spectrum shown in Figure 7.2, a strong signal appears within the fundamental band gap, peaking at voltages around +0.25 V (Figure 9.3).

In analogy to Figure 7.2, the peaks at negative voltages in Figure 9.3 are caused by quantized states S_Q confined in the zone of tip-induced band bending. Their voltage is shifted and their voltage separation is increased as compared to the spectrum at a large tip-sample separation in Figure 7.2. The reduction in the tip-

sample separation intensifies the band bending and thus increases the confinement energy in the band bending zone.

The peak at approximately +0.25 V indicates the presence of a surface state roughly 0.6 ± 0.2 eV below E_C (neglecting possible band bending effects)[2]. This is in good accordance with the energy position calculated for the minimum of the empty surface state of between 0.7 eV and 1 eV below E_C [59, 60]. Therefore, this peak is to be assigned to the onset of the surface state S_{Ga} at the $\bar{\Gamma}$ point. The absence of features related to the bulk band edge in Figure 9.3 has been shown to arise from spreading resistance effects in the transport of carriers at small tip-sample separations [73]. For larger gap voltages, the band edge reappears.

The presence of the surface state in the fundamental band gap results in an intrinsic pinning of the Fermi energy at n-type GaN $(10\bar{1}0)$ cleavage surfaces and at the analogous nanowire sidewall facets. Usually, the pinning of the Fermi energy should result in tunneling spectra without tip-induced band bending. In the present case, however, this is obviously not the case since quantized states from the zone of tip-induced band bending clearly occur. The reason for this behavior is the impossibility to fill electrons from the conduction band into the surface state, since both the surface state and the conduction band minimum have an s-type orbital character. Due to the transition rule $l \rightarrow l \pm 1$, the electron transition is impossible without the participation of a third partner, which considerably reduces the transition probability. Hence, the occupation of the surface state cannot be changed sufficiently on n-type GaN and the electric field between the tip and the surface thus cannot be screened by the surface state resulting in the fact that a tip-induced band bending occurs as if no surface state was present. This is also supported by the ability to image doping modulations on the GaN cleavage plane.

In this Part it was shown that while traditional scanning tunneling microscopy measurements suggest the absence of an empty gallium surface state in the fundamental band gap, a decrease in tip-saple separation results in the successful detection of said surface state according to *ab initio* calculations. Using this new approach, the former missing surface state S_{Ga} on the gallium nitride m-plane

[2]Due to the concentration of extrinsic surface defects on freshly cleaved GaN $(10\bar{1}0)$ surfaces being small, only intrinsic surface states can be located at the origin of the measured surface state within the band gap.

could successfully be probed with the STM. Its peak is determined to be located at 0.6 ± 0.2 eV below E_C thus being in good accordance with theoretical predictions.

Part III.

XSTM of v-shaped defects in gallium nitride

10. Introduction

For the application of gallium nitride in optoelectronic devices, the bulk material has to be reasonably free of defects [74]. However, there are hardly any large bulk substrates available and thus most epitaxial layers have to be deposited on substrates which exhibit a large lattice mismatch as well as a large thermal mismatch [3], inducing high concentrations of defects in the crystal.

The most prominent and largest features are the so-called inverted pyramidal pits at the growth surface [61, 75–77]. These micro-scale defects typically exhibit a v-shaped profile from which they received their name. During progressing growth, these v-shaped defects are overgrown. However, at present it is unclear how the v-shaped pits at the growth front will affect the resulting epitaxial material once the process of overgrowth has taken place [22]. The sparse electrical characterization of v-shaped defects in pure GaN shows strongly broadened cathodoluminescence spectra on both the growth surface [78] and at overgrown v-defects [79]. This indicates a locally increased free electron concentration of the v-shaped defects [78, 79] or at least an optically different zone extending along the c(growth)-direction [80]. Top-view measurements show an increase in the work function and the leakage current at v-pits on n-type GaN [81]. However, it is unclear to what degree these results are affected by the pinning of the Fermi energy at the polar c-plane surface [82]. Hence, the electronic structure of overgrown v-shaped defects in pure GaN remains unclear.

In this Part of the thesis, the geometric and electronic structure of overgrown v-shaped defects in gallium nitride epitaxial layers is investigated by cross-sectional scanning tunneling microscopy and spectroscopy.

A periodical change in the contrast of the STM images is investigated and a connection between the shape of the modulated contrast and the contour of the growth front is established in Chapter 11. This allows to extract irregularities at

the growth front after overgrowth using XSTM on cleavage surfaces.

In Chapter 12, overgrown v-shaped defects are identified in XSTM images, using the results of Chapter 11. The modulation visualizes the geometrical shape of the inclined growth front at v-shaped defects and the acquisition of scanning tunneling spectra within the center of the v-shaped defects and far away from the center of the v-shaped defects reveals information on their electronic characteristics.

The spatial meandering of v-shaped defects on a cross-sectional $(10\bar{1}0)$ cleavage plane of GaN(0001) epitaxial layers grown along the c-direction is investigated in Chapter 13.

11. Doping modulation in epitaxial gallium nitride

In this Chapter, a periodical change in the contrast of the STM images is investigated. A connection between the shape of the modulated contrast and the contour of the growth front is established, yielding information on large scale features on the cleavage surface.

11.1. Features on large scale STM images

Scanning tunneling microscopy offers the advantage of a very high resolution. Hence, the technique usually is employed for the imaging of the atomic structure of the sample being investigated. Due to a limited bandwidth of the electronics used to both control the tip as well as to acquire the actual data, the area being measured is usually rather small. Common STM images thus typically have a size smaller than $250\,\mathrm{nm} \times 250\,\mathrm{nm}$ when atomic resolution is to be achieved, since a further increase in image size results in a decrease in resolution if the image acquisition time is to remain reasonable. If, however, atomic resolution is not a prerequisite, the scanning tunneling microscope can be used to acquire much larger images, which can enable the observation of different, formerly unidentified properties and patterns only visible when the sample is studied on a larger scale.

In Figure 11.1, two images larger than $2000\,\mathrm{nm} \times 2000\,\mathrm{nm}$ are shown. As can be seen, there are periodical changes of contrast in both images, running bottom-left to top-right corner in (a) and left to right in (b). Despite exhibiting visible differences in the periodicity of the modulation of contrast, both images have been acquired from the same sample.

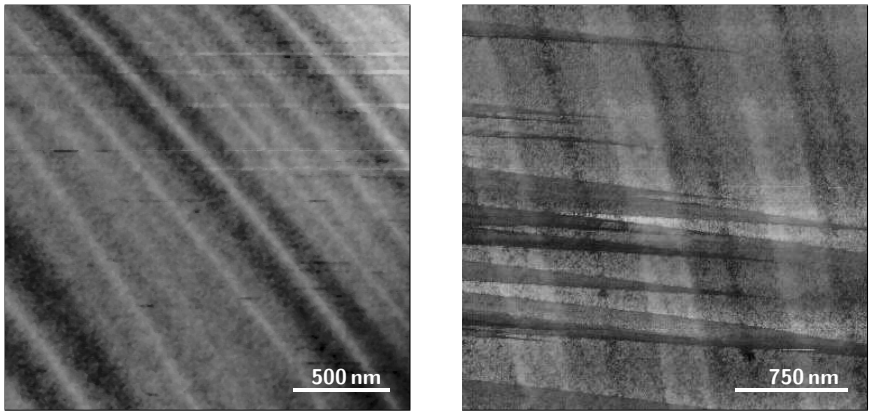

(a) 2100 nm×2100 nm, +3.25 V, 128 pA (b) 2700 nm×2700 nm, +2.5 V, 100 pA

Figure 11.1. *Two large scale scanning tunneling microscopy images showing periodical changes in contrast (bottom-left to top-right corner in (a), left to right in (b)). Despite exhibiting different periodicities in the modulation of contrast, both images have been acquired from the same sample. The cone shaped structures running left to right in (b) are actual surface steps and not part of the modulation of contrast.*

A change of contrast covering such a large scale in scanning tunneling microscopy images usually represents a change in the height of the sample. Yet, as shown in Figure 11.2, the intensity of the modulation of contrast drastically changes when altering the gap voltage: Being almost like a step-function at a gap voltage of +6.0 V, the modulation in contrast becomes more trapezoidal the smaller the gap voltages applied. An additional substructure of the modulation becomes visible at +2.5 V. Such an extreme dependence on the gap voltage suggests the modulation to be of electronic nature rather than being caused by topographical effects [83, 84]. Further evidence for this hypothesis can be drawn from the fact that, contrarily to the modulation of contrast, the actual surface steps in Figure 11.2 are not influenced by the change in gap voltage. A detailed analysis of the properties of the modulation of contrast will be presented within the next section.

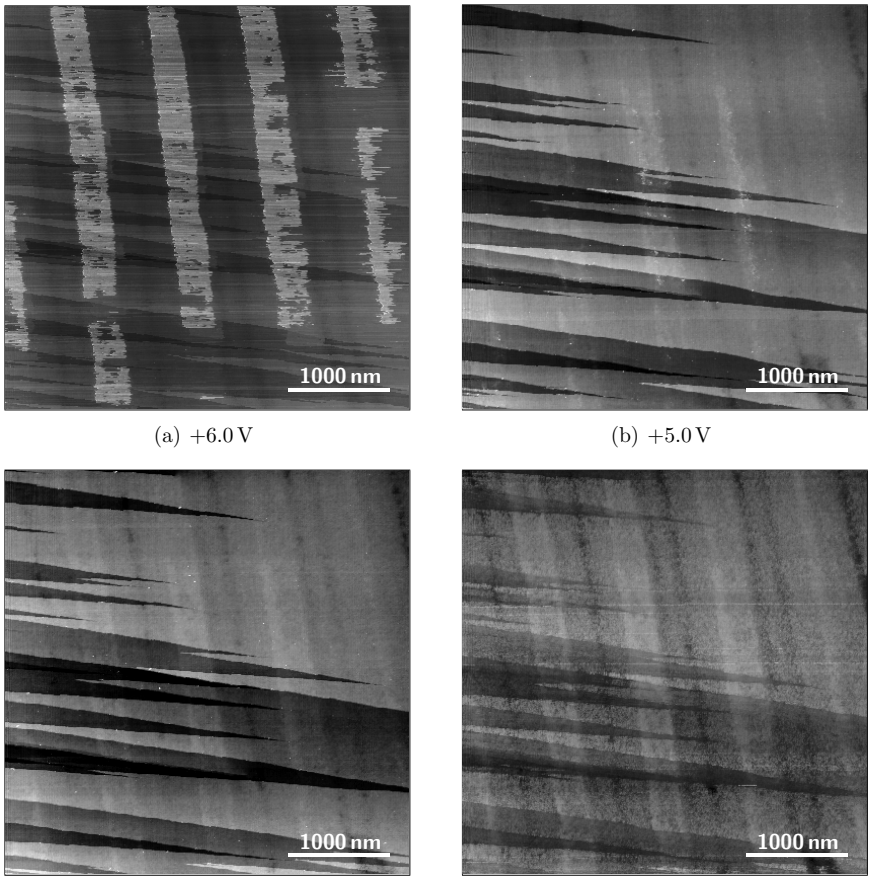

(a) +6.0 V (b) +5.0 V

(c) +4.5 V (d) +2.5 V

Figure 11.2. *STM investigation of the exact same area of the sample at different gap voltages, showing a dependency of the shape of the modulation of contrast on the gap voltage. While being almost like a step-function at a gap voltage of +6.0 V in (a), the modulation contrast becomes more trapezoidal with decreasing gap voltages. A substructure of the modulation becomes visible at +2.5 V in (d). There are also many actual surface steps visible propagating from the left hand to the right hand side of each image. The modulation of contrast does not appear to be influenced by those steps.*

11.2. Characterization of the modulation

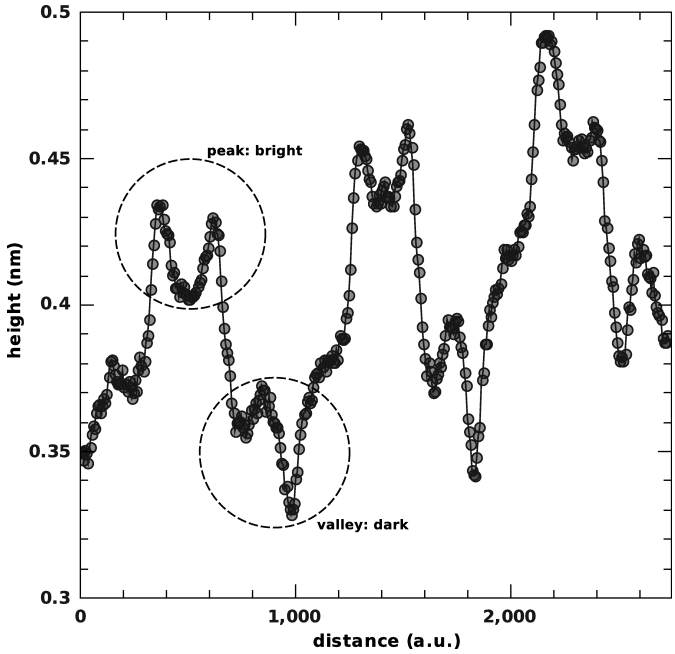

Figure 11.3. *Topographical height profile of Fig. 11.1(b). The change in contrast induces an apparent change in height of approximately 1 Å between peak and valley.*

Figure 11.3 shows the averaged topography of Figure 11.1(b): The change in contrast induces an apparent change in height of approximately 1 Å between peak and valley of the height profile.

To determine the origin of the modulation, scanning tunneling spectra were acquired both on top of the peak of the modulation, appearing as a brighter region, and in the darker areas which are the valley of the modulation. The spectra of the bright and dark areas were averaged separately and are shown in Figure 11.4. The averaged spectra of the dark and bright areas apparently mostly coincide.

11.3. Discussion of the contrast

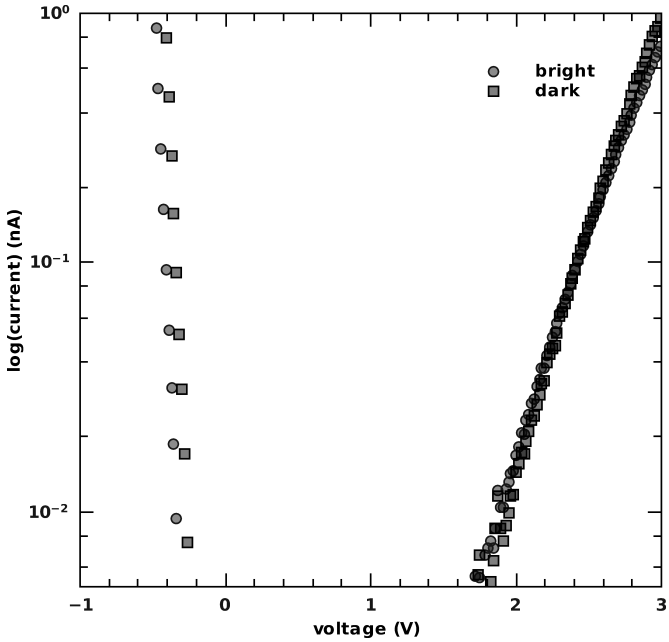

Figure 11.4. *Scanning tunneling spectra measured in bright (circles) and dark (squares) areas, acquired at +2.5 V and 100 pA.*

The modulation induces a strong change in height of the STM images. As mentioned above, the differences in height of the dark and bright areas are, however, very unlikely to be the real geometrical shape of the surface [84]. Furthermore, an analysis of the actual distribution of surface steps shows that the surface is atomically flat (aside from the surface steps). As a consequence, the different heights of the dark and bright areas can only result from the tip being further away from the surface while measuring the bright areas, thus creating a peak in the height profile in Figure 11.3 [83]. Consequently, the spectra shown in Figure 11.4 have been acquired at different tip-sample separations and need to be corrected. The difference in height of peak and valley in Figure 11.3 is approximately 1 Å. According to $I = I_0 \cdot e^{-2\kappa z}$ (Equation 2.13), a change in the tip-sample separation

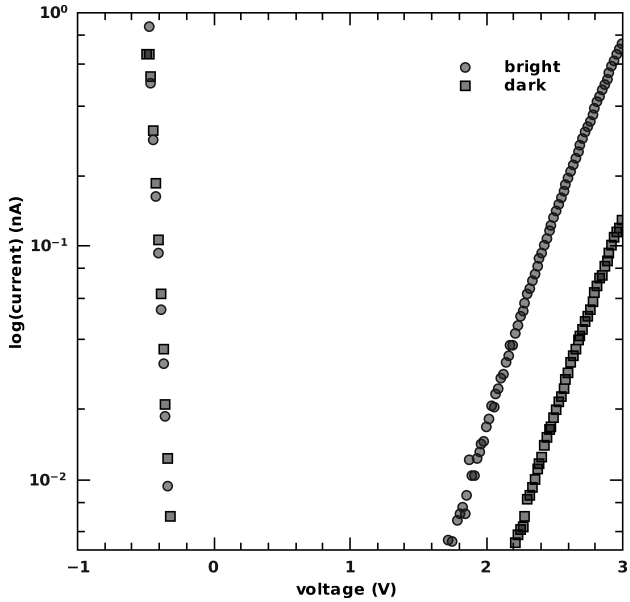

Figure 11.5. *Corrected scanning tunneling spectra measured in bright (circles) and dark (squares) areas, acquired at +2.5 V and 100 pA. The onset of the conduction band of the spectra acquired in the bright areas is shifted as compared to that of the spectra acquired in dark areas.*

of 1 Å reduces the current by a factor of 0.135[1]. This means, that the current of the spectra acquired in the bright areas is only 0.135 times the value that would result from the spectra being acquired at the same tip-sample separation as was used for the spectra in the dark areas. To compare the spectra, the current of the spectra acquired in the dark areas thus has been multiplied with a factor of 0.135 to match the tip-sample separation of the spectra acquired in bright areas. The corrected spectra are shown in Figure 11.5. While the currents of the two spectra now perfectly match within the region of the valence band, there is a distinct shift in the onset of the conduction band, resulting in the spectra appearing to have different sized band gaps. This indicates the dark and bright areas having a different carrier concentration [83, 84], which is supported by the orientation of the mod-

[1]Using $\kappa \approx 1/\mathring{A}$

ulation: A doping modulation induced by fluctuations during the growth process would be perpendicular to the c(growth)-direction, which is the same orientation as exhibited by the modulation of contrast.

The modulation of contrast is thus caused by a doping modulation induced by the growth process. It therefore maps the geometrical shape of the growth front with each period of the modulation reflecting a different time during growth.

12. Evidence of deep traps in overgrown v-shaped defects

In this Chapter, overgrown v-shaped defects in epitaxial layers of GaN are investigated using cross-sectional scanning tunneling microscopy (XSTM) and spectroscopy. In order to visualize overgrown v-shaped defects in XSTM images, an n-type doping modulation, as presented in Chapter 11, is utilized. The modulation is propagating along the c(growth)-direction of the epitaxial GaN layers and visualizes the geometrical shape of the initial growth front after overgrowth. Such a doping modulation can easily be probed with XSTM due to the induced slight potential modulation [76].

Contents of this Chapter have recently been published in [22]: P. H. Weidlich, M. Schnedler, H. Eisele, U. Strauss, R. E. Dunin-Borkowski, and Ph. Ebert. "Evidence of deep traps in overgrown v-shaped defects in epitaxial GaN layers". In: *Applied Physics Letters* **103** (2013), 062101.

12.1. Scanning tunneling microscopy observations

A constant-current XSTM image of a typical v-shaped defect exposed on a cross-sectional GaN $(10\bar{1}0)$ cleavage surface is shown in Figure 12.1, where the [0001] growth direction is toward the top of the image. The cleavage surface exhibits terraces separated by steps with some of these steps abruptly terminating at dislocation lines intersecting the cleavage surface [14]. Superimposed on the stepped surface, a doping modulation can be discerned as dark and bright contrast lines.

Figure 12.2 shows a v-shaped defect with its opening side toward the [0001] direction (right hand side of the image). The modulation of contrast is marked by dashed lines and the v-shaped edges are propagating along the growth direction

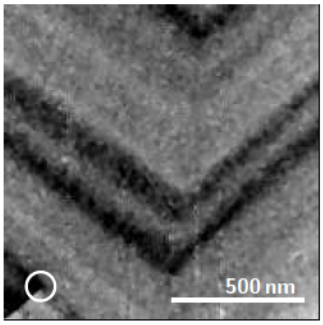

(a)

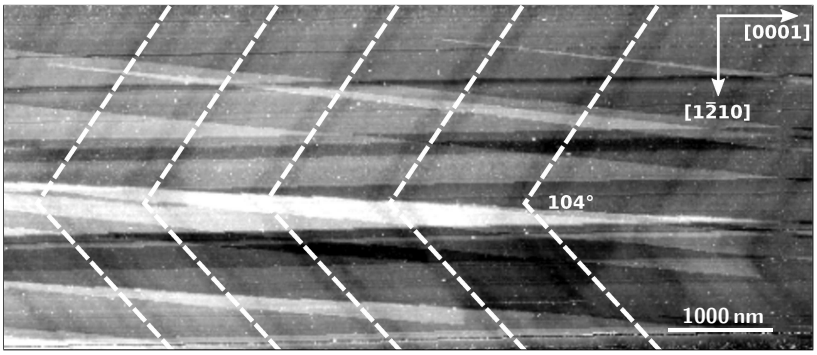

Figure 12.2. *Constant-current XSTM image of a cleaved GaN(10$\bar{1}$0) surface showing a cross-section through a v-shaped defect. The dashed lines indicate the doping modulation. The surface exhibits many cleavage steps running preferentially horizontally and forming narrow cone shaped terraces, superimposed on the contrast of the doping modulation. The image shows the density of empty states acquired at a gap voltage of +4.0 V and a set current of 100 pA.*

projections have the same opening angle of approximately 104°.

12.2. Determination of the geometric structure

The observation of stacking and a same opening angle for all m cleavage planes indicates that the overgrown v-shaped defect is orientated along the growth direction and originates from an inverted pyramidal three-dimensional pit structure at the growth surface. In previous investigations inverted hexagonal or dodecagonal pyramids were found having $\{10\bar{1}1\}$ [61, 75–80, 82, 85–93] or $\{11\bar{2}2\}$ [94] facets or both [95, 96], depending on the growth conditions. Figure 12.3 shows the two possible hexagonal pyramidal structures consisting of only $\{11\bar{2}l\}$ or only $\{10\bar{1}k\}$ planes, respectively, with $(k, l > 0)$.

To enable the determination of the type of these semi-polar facets present in the XSTM images, the shape of the measured opening angle is compared to the shape resulting from the geometry of the two possible hexagonal pyramids, as shown in Figure 12.4. An inverted hexagonal pyramid consisting of $\{11\bar{2}l\}$ facets

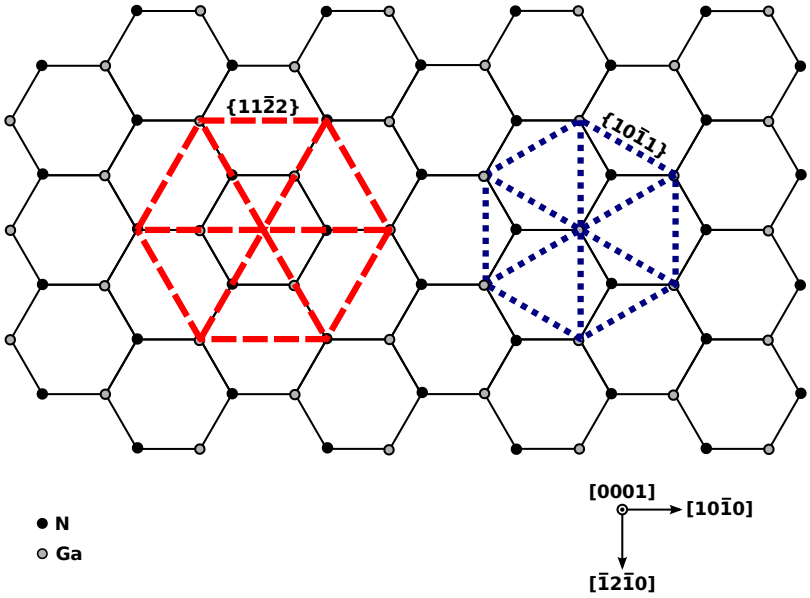

Figure 12.3. *Possible hexagonal pyramidal structures in wurtzite GaN: Hexagonal pyramids can consist of only* $\{11\bar{2}l\}$ *(dashed lines) or only* $\{10\bar{1}k\}$ *(dotted lines) planes, with* $(k, l > 0)$*.*

exhibits a v-shape in an m-plane cross section (Figure 12.4(c)), whereas pyramids consisting of $\{10\bar{1}k\}$ planes have a cross section with a flat bottom in the m-plane (Figure 12.4(f)). Without exception, every v-shaped defect imaged had a v-shaped bottom. Accordingly, the inverted pyramids must consist of $\{11\bar{2}l\}$ facets.

To determine the inclination, described by l, of the $\{11\bar{2}l\}$ facets, the opening angle is used. This angle of 104° agrees well with $l = 2$, for which an opening angle of 101.8° can be derived. If such a v-shaped defect is cleaved exactly through its center, the opening angle is reduced to 63.2°. Due to the large size of the v-shaped defects, however, it is much more likely to observe an off-center cleavage, where the opening angle on an m-plane cross section is 101.8°. Thus, the facets overgrown in these GaN epitaxial layers were $\{11\bar{2}2\}$ planes, which form the side facets of the inverted hexagonal pyramids as shown schematically in Figure 12.4(a).

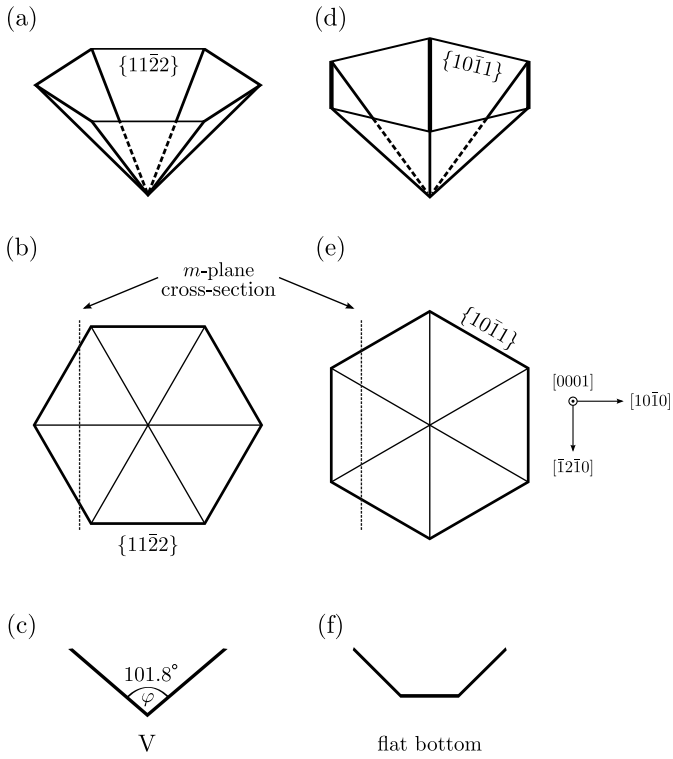

Figure 12.4. *Schematics of the three-dimensional structures of two possible hexagonal inverted pyramidal pits on a wurtzite GaN c-plane (a,d), top views (b,e), and cross sections at the m-plane (c,f). (a-c) and (d-f) show a pit with* $\{11\bar{2}2\}$ *and* $\{10\bar{1}1\}$ *facets, respectively, exhibiting a v-shaped profile or a profile with a flat bottom on the m-plane, respectively.*

12.3. Scanning tunneling spectroscopy on v-shaped defects

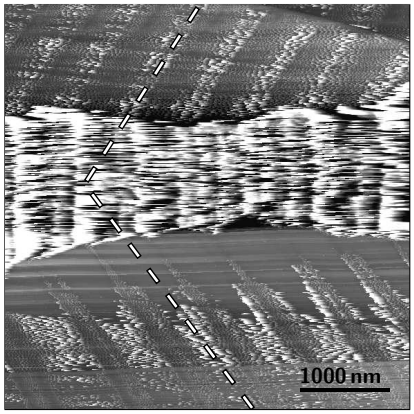

Figure 12.5. *Cross-sectional STM image. Oscillations of the tunneling current arise close to the center of the v-shaped defect (stacked horizontally in* [0001] *direction in the center of the image). The region with oscillations typically is 1 to 3 µm wide and extends along the c-direction.*

There is no visible difference between the center and the areas far away from the v-defects in the XSTM image shown in Figure 12.2. In other areas of the sample, however, the tunneling current is unstable near the cross-sectioned centers of the v-defects. This tunneling behavior results in oscillations in the XSTM image as seen in Figure 12.5. The region with oscillations is typically 1 to 3 µm wide and extends along the *c*-direction. These oscillations result in a collapse of the tunneling current and are visible for positive gap voltages only, as can be seen from Figure 12.6. In Figure 12.6(a) which was measured at +4.0 V, the oscillations are clearly visible within proximity to the center of the v-shaped pit. At -4.0 V as shown in (b), however, no oscillations can be observed. This voltage dependence indicates that v-shaped defects lancing through the sample might affect the electronic properties of the GaN epitaxial layers.

With the purpose of investigating possible electronic effects, scanning tunneling spectra were measured at the center of the cross-section of v-shaped defects and in

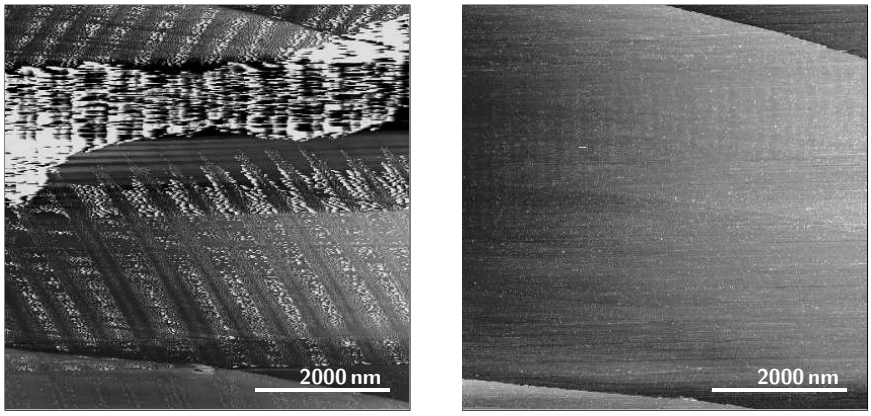

(a) +4.0 V (b) -4.0 V

Figure 12.6. *(a) Cross-sectional STM image measured at +4.0 V. Oscillations of the tunneling current arise close to the center of the v-shaped defect if positive gap voltages are applied. (b) Same area of the sample measured at -4.0 V. At negative gap voltages, the oscillations do not occur.*

areas far away from the defects. Averaged spectra of both locations are shown in Figure 12.7. The spectra far away from the defects show an onset of the tunneling current at -1.8 V for negative gap voltages and an onset at +1.8 V for positive gap voltages. In contrast, spectra measured at the center of the v-defects exhibit a slightly smaller onset voltage at negative voltages, but a much larger onset voltage for the tunneling current for positive gap voltages of approximately +4.0 V. Hence, tunneling is significantly more difficult at positive voltages.

12.4. Discussion of the electronic properties

To ascertain the origin of the different electronic properties within the v-shaped defect, simulations of the tunneling spectra were performed using the theoretical model as introduced by Bono and Good [97] as well as the software of R. M. Feenstra based on this model [98–104]. Since a highly stepped n-type GaN surface was observed, it is assumed that the defect states, e.g. at step edges, pin the Fermi energy. Using a band gap of 3.39 eV, the calculation yields results that

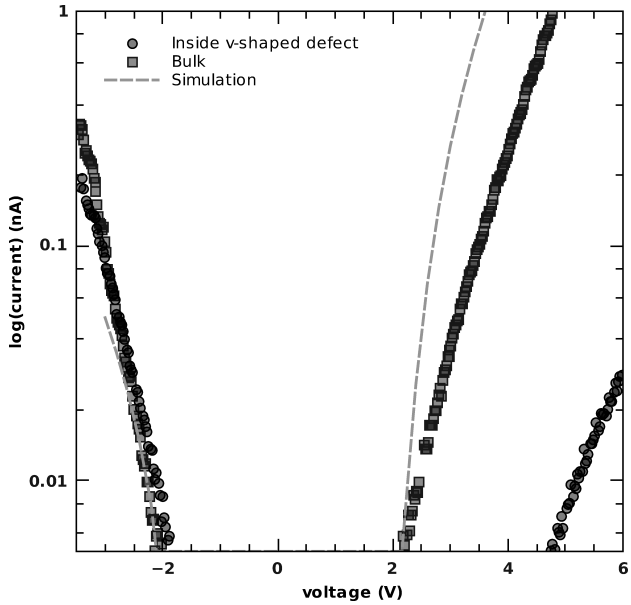

Figure 12.7. *Tunneling spectra measured at the center of a cross-sectioned v-shaped defect (black circles) and far away from the v-shaped defect (blue squares). The large apparent band gap of the tunneling spectrum measured at the v-shaped defect indicates a suppression of tunneling current for positive voltages due to deep traps. The dashed line is a calculated spectrum with an assumed pinning by surface defect states using the theory presented by Bono and Good [97]. The results of the simulation are in good accordance with the spectrum acquired in the bulk region far away from the center of the v-shaped defect.*

are in good accordance with the tunneling spectra measured far away from the v-shaped defect, as can be seen from the dashed line in Figure 12.7. For positive gap voltages, the current arises from electrons injected into the conduction band while for negative gap voltages, the current is caused by electrons being extracted from the valence band states [76]. This is in good agreement with typical tunneling spectra measured on pinned m-plane cleavage surfaces of n-type GaN [58, 61]. In contrast, the tunneling spectra measured in the vicinity of the center of the v-

shaped defect cannot be simulated using a reasonable low carrier concentration or any realistic material parameter as the apparent band gap widens strongly despite the assumed pinning. This indicates the carrier dynamics[2] within the GaN sample inhibiting an efficient injection of electrons [105], suggesting the presence of deep electron traps at the center of the v-defect. The electrons get caught in the deep trap and the surrounding GaN area experiences a charge-up, inhibiting further electron tunneling. These deep traps cannot be emptied, since the concentration of holes in the valence band (minority carriers) is far too low. However, the presence of the deep traps does not affect the hole conductivity and thus does not influence the process of extracting electrons from the valence band at negative voltages. Hence, based on this theory, a normal conductivity can be observed at negative voltages only, which is in excellent agreement with the experimental observations. At positive voltages large enough for a tunneling current to be observed, hot carriers with energies significantly higher than the energy of the conduction band edge ($\gtrsim 2.5\,\mathrm{eV}$) are injected. Hot electrons require longer times for thermalization during which they are able to migrate over long distances. They are thus able to leave the zone which is trapping thermalized carriers.

Another factor important for the electronic properties of the sample is the spatial distribution of the deep traps. The fraction of v-shaped defects containing deep traps (and hence exhibiting an unstable tunneling current) is found to be approximately one third of the investigated length along the c direction. The transition between sections with stable tunneling current and sections without tunneling current, i.e. those areas with oscillations, occurs along the same v-shaped defects. At the same time, there is no evidence of the cross-sectional cleavage plane being significantly ($\gtrsim 3\,\mu\mathrm{m}$) shifted with respect to the center of the v-shaped defect. The local absence of the tunneling current at positive voltages hence suggests the deep traps being distributed inhomogeneously along the line direction of the v-shaped defects. They are, however, always located close to the center of the cross-sectioned v-defect. Since the samples were cleaved macroscopically, the cleavage surface statistically is off-center with respect to the actual center of the v-defect. The observation of an inhomogeneous distribution of deep traps along the v-shaped defects hence may also be arising from fluctuating radial extensions of the distribution of

[2]This phenomenon has not been included in the calculations.

deep traps along the v-shaped defects. These inhomogeneous electronic properties of the v-shaped defects may explain the diverging reports about the electrical properties of v-shaped defects [77–82, 85, 86, 106].

In conclusion, v-shaped defects were found to be present in the samples. They are inverted hexagonal pyramids consisting of $\{11\bar{2}2\}$ side facets. Some of these v-shaped defects contain deep traps located close to their center, resulting in an unstable tunneling current. The deep traps are, however, distributed inhomogeneously along the line direction of the v-shaped defects.

13. Meandering of v-shaped defects

In this Chapter, the spatial meandering of v-shaped defects on a cross-sectional $(10\bar{1}0)$ cleavage plane of GaN(0001) epitaxial layers (grown along the c-direction) is investigated using scanning tunneling microscopy.

13.1. Experimental observations

Figure 13.1 shows a constant-current XSTM image of a typical overgrown v-shaped defect exposed at a cross-sectional GaN $(10\bar{1}0)$ cleavage surface. The [0001] growth direction is toward the right hand side of the image. Hence, the layers at the left hand side of the image were grown first and the location of the apex of the v-shaped dashed lines yields the position of the v-shaped corners as a function of the progressing growth. The average position of the apexes of the v-shaped lines form a line extending along the growth direction as indicated by a dashed horizontal line in Figure 13.1. The apexes of some of the dashed v-shaped lines, however, are displaced with regard to the average position of the apexes, with a displacement along the $[1\bar{2}10]$ direction labeled δ_1, δ_2 and δ_3. These lateral displacements were observed to have values of up to 0.5 µm. Despite the existence of those lateral displacements, the angle between the cross sectioned inclined facets of the v-shaped defects and the average position of the apexes is not changed. The geometrical shape[1] of the v-shaped defects is hence not changed by the lateral displacements. Accordingly, the lateral displacements of apexes are caused by spatial shifts of the center of the v-shaped defects at the growth surface.

[1] A pyramidal shape delimited by six $\{11\bar{2}2\}$ planes with an opening angle on the cross-sectional m-plane of $\alpha = 101.8^{\circ}$, see Chapter 12 and [22].

Figure 13.1. *Constant-current XSTM image of a cleaved n-type $GaN(10\bar{1}0)$ surface. The image shows a cross-section through a v-shaped defect. The v-shaped structure is indicated by the dashed lines. Some of the apexes of the kinks in the dashed lines are displaced in relation to the average position of the apexes (horizontal dashed line). The lateral displacements are marked by δ_1 to δ_3. Dislocation lines are intersecting the cleavage surface (marked by circles) at the end of some steps. The image shows the density of empty states acquired at a voltage of +4.0 V and 100 pA set current.*

13.2. Quantification of the meandering

To quantify the spatial shifts of the v-shaped defects, the lateral displacement of the apex was measured for every doping modulation period. For this purpose, several v-shaped defects were analyzed. A schematic representation of the displacement of a v-shaped defect is shown in Figure 13.2; The length of one period of the modulation is x_{mod}. Without crossing the arm of the i-th "v", the (i+1)-th "v" can be laterally displaced up to a maximal length δ_{max} given by $\delta_{\mathrm{max}} = \tan(\alpha/2) \cdot x_{\mathrm{mod}}$ with α being the opening angle of the "v"'s. The actual displacement of "v_i" in relation to the position of the mean of all apexes parallel to the c-axis (gray solid line) is labeled δ_i.

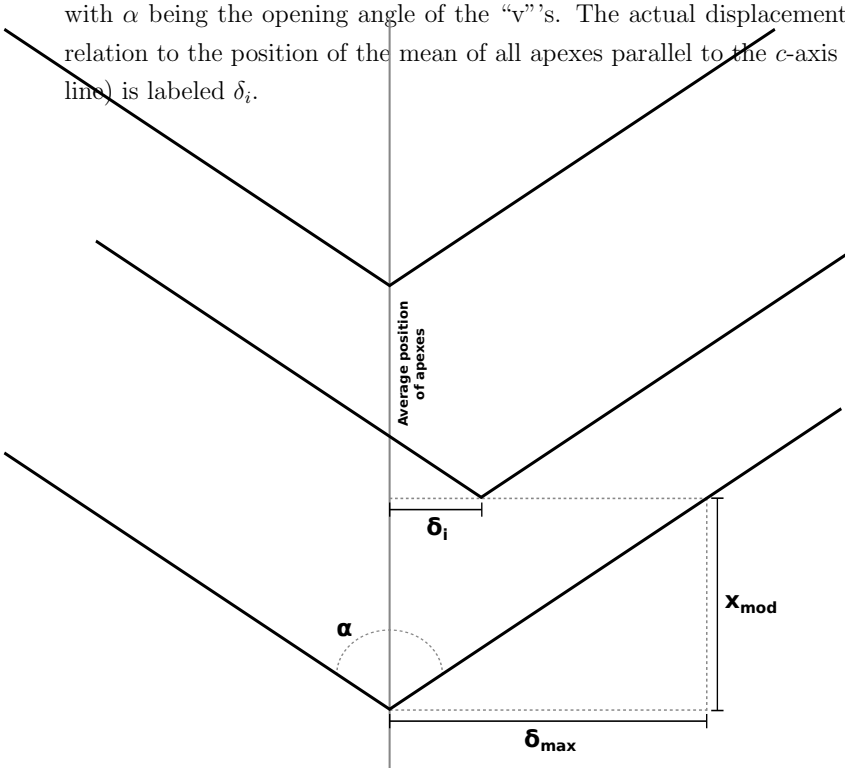

Figure 13.2. *Schematics of meandering: The length of one period of the modulation is x_{mod}. Without crossing the arm of the i-th "v", the (i+1)-th "v" can be displaced laterally up to a length δ_{max} given by $\delta_{\mathrm{max}} = \tan(\alpha/2) \cdot x_{\mathrm{mod}}$ with α being the opening angle of the "v"'s. The actual displacement of "v_i" in relation to the position of the mean of all apexes parallel to the c-axis (gray solid line) is labeled δ_i.*

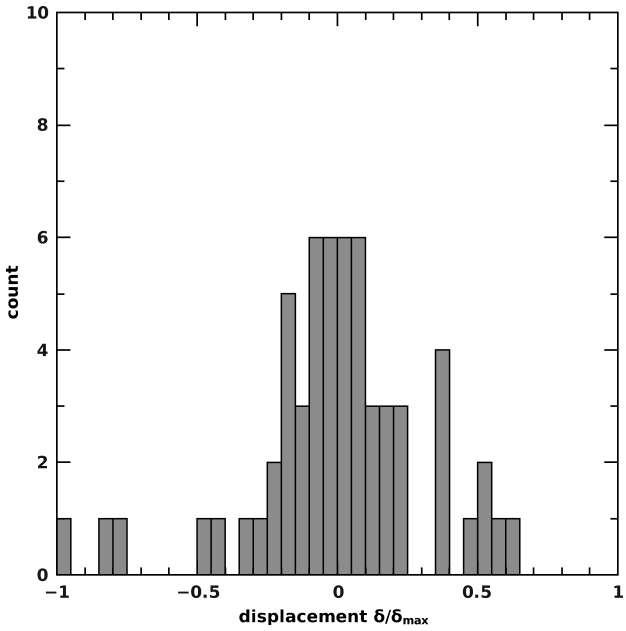

Figure 13.3. *Frequency distribution of the lateral displacements δ from the average position of the meandering v-shaped defects along the $[1\bar{2}10]$ direction in units of the maximal lateral displacement $\delta_{max} \approx 1.2\,\mu m$. The distribution is centered along the c-direction (equal to displacement 0), but exhibits a large width.*

The resulting distribution of the lateral displacements δ from the average position along the $[1\bar{2}10]$ direction is shown in Figure 13.3. The lateral displacement is measured in units of the maximal lateral displacement of the cross-sectioned v-shaped defect

$$\delta_{\max} = x_{\mathrm{mod}} \times \tan\left(\frac{101.8}{2}\right) \approx 1.2\,\mu\mathrm{m} \tag{13.1}$$

with $x_{mod} \approx 1\,\mu$m. The distribution is symmetrical and centered around a lateral displacement $\delta = 0$. Therefore, the overgrown v-shaped defects on average propagate along the growth direction. The width of the distribution of $0.27 \times \delta_{\max}$, however, shows a significant meandering perpendicular to the growth direction. Figure 13.4 shows the frequency distribution of jumps $\Delta_i = \delta_i - \delta_{i-1}$ in the lateral

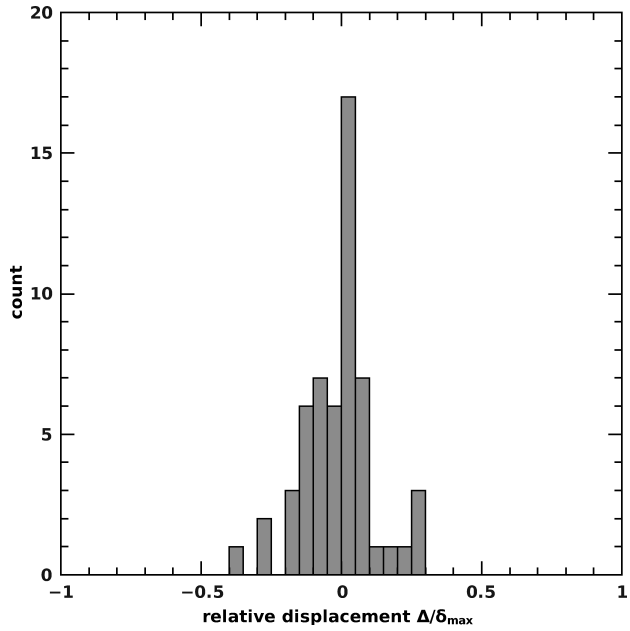

Figure 13.4. *Frequency distribution of the jumps in lateral displacement $\Delta_i = \delta_i - \delta_{i-1}$ within one period. Jumps in lateral displacements of up to 0.5 µm occur.*

displacement between one period and another. As can be seen, jumps of up to 0.5 µm occur within one period. Assuming that the line of the apex constantly bends over the whole modulation period rather than suddenly kinks, the bending angle in the $(10\bar{1}0)$ projection would be in the order of 26°.

13.3. Determination of the origin of the meandering

In an ideal, dislocation-free GaN material no strain field is present and hence a v-shaped defect should not undergo any lateral displacements with progressing growth. The spatial position would then only be determined by the growth speeds on the different facets. Since in theory, the six delimiting $\{11\bar{2}2\}$ facets have equal growth speeds, the inverted pyramidal pit at the growth surface should either

deepen or flatten out, depending on the relative growth speed along the c-direction. For GaN grown with hydride vapor phase epitaxy, however, inverted pyramidal v-shaped pits are known to form around growth instabilities, such as impurities, droplets, and/or defects [96, 107]. As a consequence, strain fields are induced which in turn can be expected to act as nucleation centers for threading dislocations around which the v-shaped defects form. The material hence cannot be considered to be free of strain. The v-shaped defect is overgrown during processing growth and its apex follows the intersection point of the dislocation at the growth surface at any time. Therefore, the directions of the dislocation lines are of great importance.

In general, there are three different types of threading dislocations in GaN epitaxial layers: First, pure edge dislocations with an $\frac{a}{3}\langle 11\bar{2}0\rangle$-type Burgers vectors are usually bent toward the non-polar directions [25, 37, 108–110] since their lowest energy state is for a 90° bending, where they become pure screw dislocations. Second, dislocations with an $\frac{a}{3}\langle 11\bar{2}\ (\pm\frac{3c}{a})\rangle$ Burgers vector, i.e. components along the a- and c-direction, have a significantly lower concentration [16, 111, 112] due to the higher energy related to the longer Burgers vector [113]. The third type of threading dislocations are pure screw type dislocations with a Burgers vector of $\pm c[0001]$. Their energy is lowest with a line direction along the c-direction [114]. Hence, they are likely to propagate through the entire epitaxial layer during overgrowth, eventually intersecting the growth surface [115]. The latter kind of dislocation can be expected to be dominating at the center of the v-shaped defects.

Although screw dislocations with a $\pm c[0001]$ Burgers vector ought have a line direction parallel to the Burgers vector, their line orientation may deviate from this preferred c-direction. The screw dislocations will interact with strain fields in the material. As stated in Chapter 15 and [37], dislocations are found to form agglomerations in GaN epitaxial layers, resulting in a fluctuation in the magnitude and orientation of the surrounding strain fields as well as the degree of interaction between the dislocations, which then induces a meandering of the screw dislocations. If the line energy of the dislocation is negligibly small, the dislocation will meander through the material along a line with minimal energy of strain interaction. In case of an orientation dependent line energy of the dislocation, the line will be bent to towards the preferred line direction to a certain amount, thus reducing the meandering.

The meandering introduced by the strain interaction of the screw dislocation induces spatial shifts of the intersection point of the dislocations at the growth surface. The apex of the inverted pyramidal pit at the growth surface consequently follows these spatial shifts. On that account, the apex of the overgrown v-shaped defect meanders with progressing growth, tracing the meandering dislocation. The pronounced meandering of the v-shaped defects proposes the dislocation also exhibiting a strong meandering, significantly bending the line direction. The spatial offsets of the apexes presented in Figure 13.4 show that bending angles of the order of 26° can be reached.

In conclusion, the apexes of the overgrown v-shaped defects are found to meander with progressing growth. The meandering is traced to a wriggly dislocation line at the core of each v-shaped defect.

Part IV.

Characterization of dislocations and their interactions

14. Introduction

The efficacy of devices based on GaN is currently limited by the quality of the bulk crystal material. Since there are hardly any large bulk substrates available [4], almost all GaN films are grown on substrates exhibiting a large lattice mismatch as well as a large thermal mismatch using heteroepitaxy or they are deposited on pseudo substrates which themselves were nucleated on mismatched substrates [3]. The mismatch induces high concentrations of defects, of which in particular dislocations negatively affect the properties of the device.

To improve the quality of GaN substrates, the high concentrations of dislocations have to be reduced [23]. A large variety of methods targeting the reduction of defects in GaN have been developed recently with the aim of interrupting the propagation of dislocations along the growth direction by bending their line direction. Crucial factors for the optimization of the reduction of dislocations are the interaction between dislocations themselves, between dislocations and the growth front as well as between dislocations and other defects. Unfortunately, rather little is known about interactions of dislocations in GaN epitaxial layers [34–37].

Hence, a detailed investigation of interactions between dislocations and v-shaped defects as well as between dislocations themselves is presented in Chapter 15. The investigation is performed by mapping the spatial distribution of dislocations as well as their projected line directions on a cross-sectional GaN $(10\bar{1}0)$ cleavage plane of GaN (0001) epitaxial layers using scanning tunneling microscopy.

In Chapter 16, a methodology for the determination of the intersection angle of a dislocation line is presented. Combined with the projected line direction of the dislocation, the entire three dimensional angle of intersection between the dislocation line and the cleavage surface can be determined.

15. Repulsive interactions between dislocations and overgrown v-shaped defects

Interactions between dislocations and v-shaped defects are investigated within this Chapter. The investigation is performed by mapping the spatial distribution of dislocations as well as their projected line directions on a cross-sectional GaN $(10\bar{1}0)$ cleavage plane of GaN (0001) epitaxial layers using scanning tunneling microscopy.

Contents of this Chapter have recently been published in [37]: P. H. Weidlich, M. Schnedler, H. Eisele, R. E. Dunin-Borkowski, and Ph. Ebert. "Repulsive interactions between dislocations and overgrown v-shaped defects in epitaxial GaN layers". In: *Applied Physics Letters* **103** (2013), 142105.

15.1. Experimental observations

Simultaneous mapping of the positions and line directions of dislocations is a rather difficult task thus far. The concentration of dislocations on surfaces can be mapped routinely by techniques like atomic force microscopy and etch point counts [107, 109, 116, 117]. However, these methods do not allow for the mapping of the line direction. Transmission electron microscopy allows a determination of the Burgers vector and line direction of dislocations as well as their concentration, but large scale mapping of several micrometers still remains a challenge.

In contrast, scanning tunneling microscopy allows a simultaneous determination of the Burgers vector and projected line direction of dislocations as well as a mapping of the concentration of dislocations over large areas of view [14]. To map

the positions of dislocations relative to the position of v-shaped defects, the n-type doping modulation presented in Chapter 11 is utilized.

Figure 15.1 shows a large scale overview mosaic consisting of three constant-current XSTM images, all of which have been enhanced by removing the non-linear distortion using the technique presented in Chapter 4. The [0001] growth direction is toward the top side of the image. As can be seen, the cleavage surface exhibits a number of terraces which are primarily separated by steps with a height of one monolayer. Some steps abruptly terminate at dislocations which are intersecting the cleavage surface [14]: These points are marked by dashed circles in Figure 15.1. Superimposed, the periodical contrast change arising from the doping modulation can be discerned as dark lines. The orientation of the doping modulation exhibits two sharp v-shaped cross-sections marked by v-shaped dashed lines which are extending along the growth direction. Two dashed vertical lines trace the growth direction. As shown in Chapter 12 and in Reference [22], v-shaped edges in these GaN epitaxial layers arise from overgrown v-shaped defects with six inclined $\{11\bar{2}2\}$ growth facets.

Each dislocation observed in Figure 15.1 induces a step with the height of one monolayer into the GaN $(10\bar{1}0)$ cleavage surface. This type of step corresponds to a Burgers vector of the type $\pm\frac{a}{3}[11\bar{2}0]$ or $\pm\frac{a}{3}[\bar{2}110]$, each of which is tilted by 30° with respect to the surface normal [14]. In general, a scanning tunneling image would also be compatible with "mixed" dislocations, such with an a+c Burgers vector, but their concentration is significantly lower [16, 111, 112] due to the higher energy related to the longer Burgers vector [113]. Dislocations with Burgers vectors lying fully within the surface plane, for example along the c direction, cannot be observed in such a large scale image due to the lack of lateral atomic resolution. Hence, only dislocations with $\frac{a}{3}\langle 11\bar{2}0\rangle$ Burgers vectors are observed.

Dislocations with such a Burgers vector are initially $\frac{a}{3}\langle 11\bar{2}0\rangle$-type threading edge dislocations with a line direction parallel to the [0001] direction. They never intersect with the cleavage plane and would thus be invisible. As a consequence, the lines of all dislocations observed on the cleavage surface have been bent away from the [0001] direction. These dislocations therefore switched from a pure edge type to a mixed type.[1]

[1] A more detailed analysis of the line direction will be performed in Chapter 16.

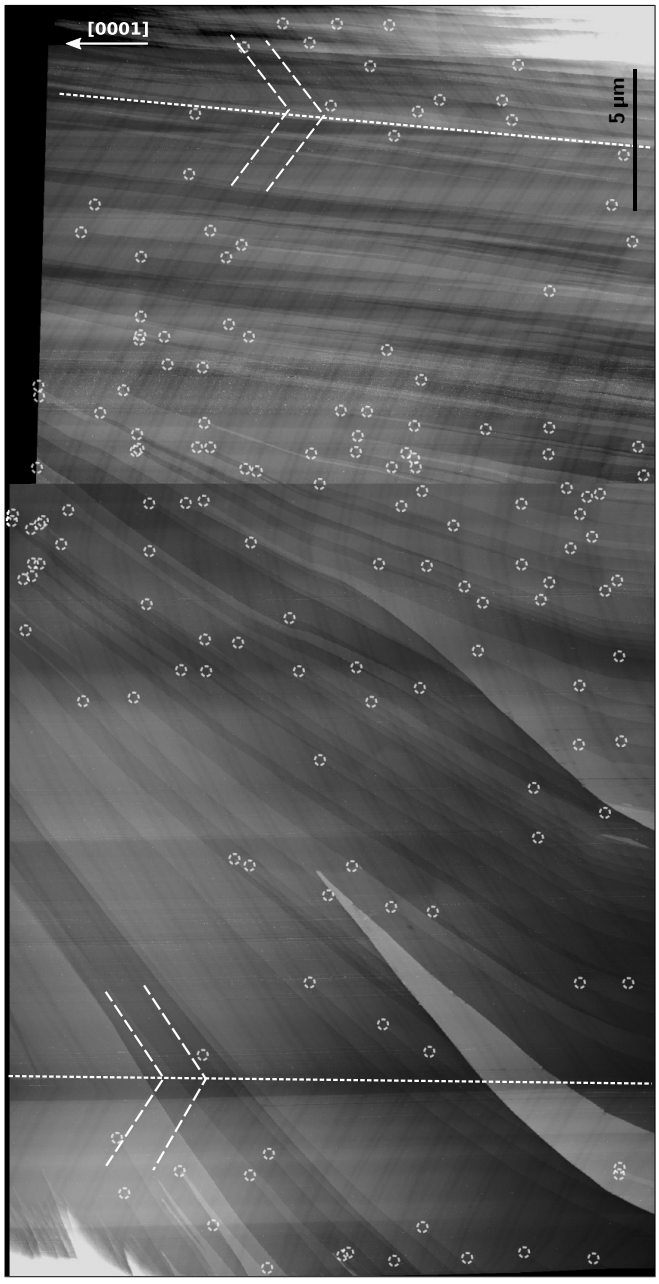

Figure 15.1. *Mosaic consisting of three corrected constant-current STM images of a cross-sectional cleavage plane through an epitaxial GaN(0001) layer. Two v-shaped defects are visible (dashed lines). The surface consists of terraces separated primarily by steps with the height of one monolayer. Dislocations intersect with the cleavage surface at termination points of steps (marked by dashed circles).*

15.2. Distribution of the dislocations

The STM image presented in Figure 15.1 also contains information on the spatial distribution of dislocations with respect to v-shaped defects. Each dislocation is marked by a dashed circle. The corresponding derived local density of dislocations is shown in Figure 15.2(c) and exhibits strong fluctuations. Two effects stand out:

First, the average concentration[2] of dislocations shown in Figure 15.2(c) changes by almost one order of magnitude along the $[1\bar{2}10]$ direction and reaches its maximum of about $5{\times}10^7\,\mathrm{cm}^{-2}$ for dislocations located in the area between the v-shaped defects. The minima occur at the centers of the v-shaped defects, whose positions are indicated by the dashed lines.

Second, the distribution of dislocations within the region of high densities exhibits striking inhomogeneities along the growth direction. The dislocations form agglomerations with dimensions of $3-5\,\mu\mathrm{m}$ that are each consisting of 10 to 20 dislocations. The concentration in these agglomerations reaches values of up to $1{\times}10^8\,\mathrm{cm}^{-2}$. In areas with a low density of dislocations, only individual dislocations are observed.

For an understanding of the formation of these agglomerations, the line directions of the dislocations might provide an insight. Initially, their line directions run parallel to the [0001] growth direction, but with progressing growth they may bend toward non-polar directions. Since only dislocations intersecting the $(10\bar{1}0)$ cleavage plane could be probed during the measurements, their lines have bent. The line direction can be further quantified using the displacement field visible in the STM images [14]. The displacement field of a dislocation has its maximum at the core of a dislocation and decays with increasing distance from the core[3]. If a dislocation line intersects the surface with a large angle with respect to the normal direction, the displacement field of the subsurface dislocation distorts the surface anisotropically. This can be seen in Figure 15.3 where the derivative of a detail from Figure 15.1 is shown. The displacement field extends anisotropically downward, tracing the line direction. The diagonal contrast lines arise from steps and

[2]The values of the concentrations only take into account dislocations with $\frac{a}{3}\langle 11\bar{2}0\rangle$-type Burgers vectors sticking out of or into the cleavage plane. The third $\frac{a}{3}\langle 11\bar{2}0\rangle$-type Burgers vector is lying parallel to the cleavage plane and hence is invisible in the STM images. Assuming an equal distribution of all Burgers vectors, the actual concentration is likely 50% higher.

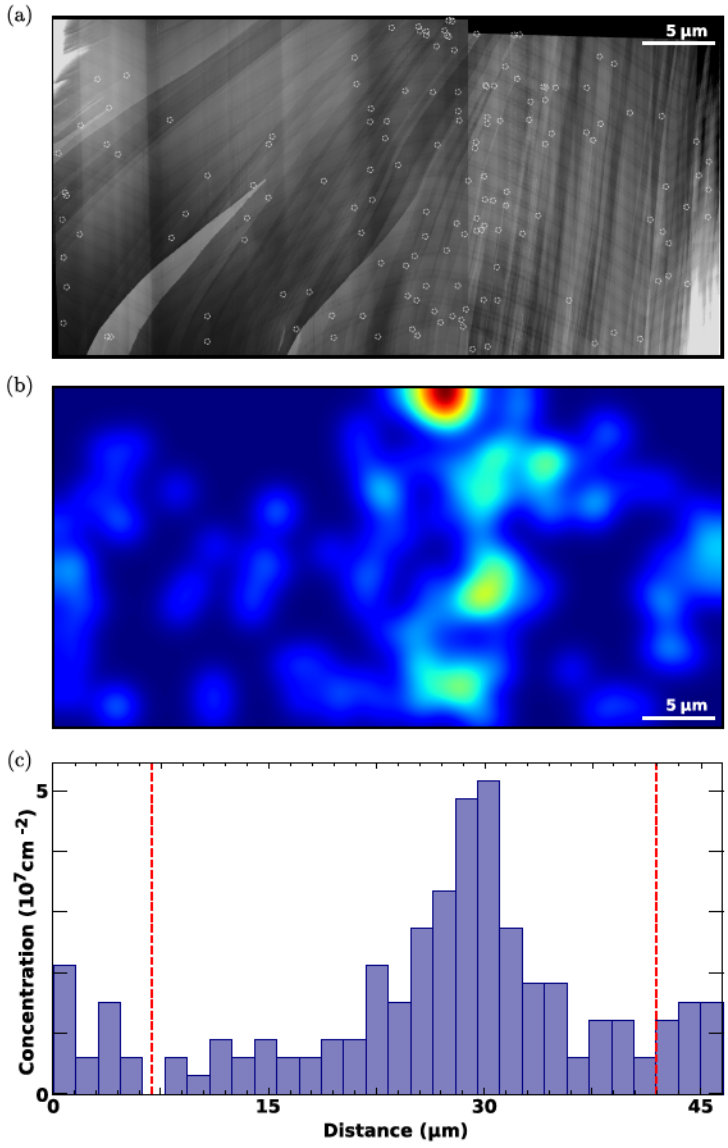

Figure 15.2. *(a) Mosaic consisting of three corrected constant-current STM images of a cross-sectional cleavage plane through an epitaxial GaN (0001) layer (taken from Figure 15.1). (b) Graphical representation of the local concentration of the dislocations intersecting the cleavage surface shown in (a), enabling the observation of agglomerations of dislocations. The colors dark blue and bright red indicate the lowest and highest ($1 \times 10^8 cm^{-2}$) concentration of dislocations, respectively. (c) Average concentration of dislocations along the $[1\bar{2}10]$ direction. The concentration meets its minimum at the locations of the v-shaped defects (indicated by dashed lines).*

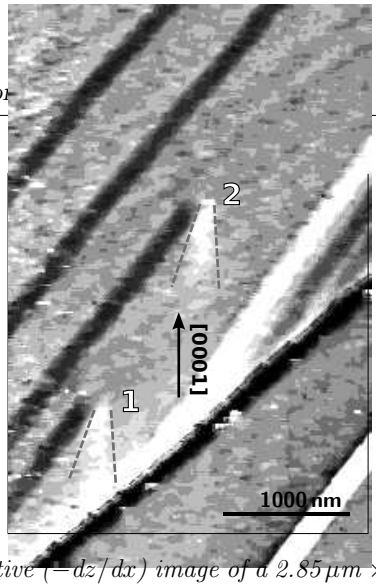

Figure 15.3. *Derivative ($=dz/dx$) image of a 2.85 µm × 2.85 µm detail from Figure 15.1. The straight black and white lines arise from the steps. The two dislocations exhibit a displacement field rotated by about 10° relative to the* [0001] *direction.*

are not of interest. Dislocations intersecting the surface perpendicularly, however, yield a spherical displacement field.[3]

Using this analysis, the projected line direction of every single dislocation in relation to the [0001] direction was determined. The line directions are shown in Figure 15.4(b), where the angle of each dislocation is plotted as color-coded circle at the position of the dislocation intersecting the cross-sectional surface using the same image as in Figure 15.1. Open circles represent dislocations with line directions normal to the surface (no detectable projected component). Figure 15.5 shows the frequency distribution of the projected line directions of the dislocations. In this analysis, the projected line directions in $[1\bar{2}1l]$ and $[\bar{1}2\bar{1}\bar{l}]$ directions are considered to be identical since the orientation of the dislocation line is arbitrary. The minimum at 0°, representing dislocation lines with a projected orientation along the c direction, indicates that most dislocations are bent, with large bending angles (>30°) apparently being preferred. Dislocations without a projected component of the line direction (not included in Figure 15.5), have a line direction perpendicular to the cross-sectional surface, i.e. they also have a large bending angle with respect to the [0001] direction. Figure 15.4(c) shows the average local projected line direc-

[3]Further analysis of the displacement fields of dislocations intersecting a surface is presented in Chapter 16.

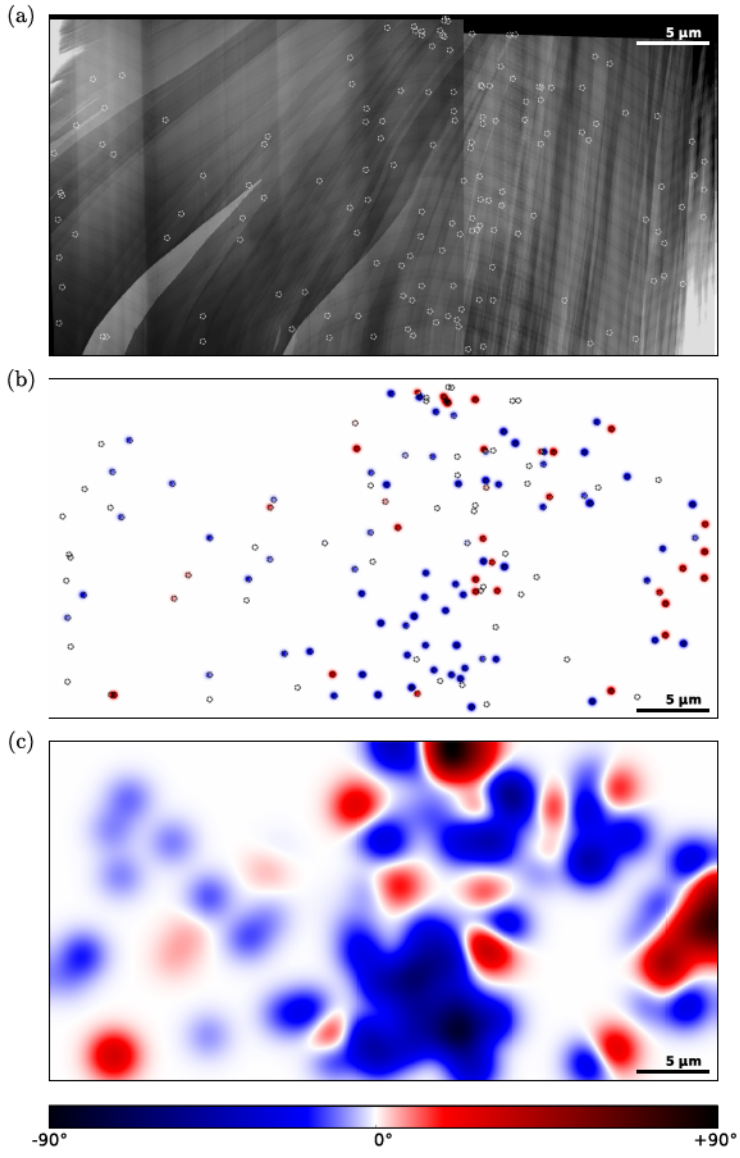

Figure 15.4. (a) Mosaic consisting of three corrected constant-current STM images of a cross-sectional cleavage plane through an epitaxial GaN (0001) layer (taken from Figure 15.1). (b) Color coded angle of the projected dislocation line direction with respect to the c direction (at 0°) marked at the spatial position of every dislocation of the image displayed in (a). Open circles represent line directions perpendicular to the surface. (c) Local average of projected line directions of the dislocations using the same color coding as in (b). The data suggests bundles of parallel dislocation lines.

tions. The large areas of same colors indicate agglomerations of dislocations with similar projected line directions, suggesting the presence of bundles of dislocations with mostly parallel line orientations.

15.3. Discussion

The statistical analysis above shows that the dislocation lines are bent toward the non-polar directions. Calculations yield the lowest energy state for a 90° bending resulting in a pure screw dislocation [114]. Local energy minima also exist for 45° bending angles. It can be expected that the bending results in an identical reduction of the energy of all dislocations with $\frac{a}{3}\langle 11\bar{2}0\rangle$ Burgers vectors. Hence, dislocations with the same Burgers vector should be bent similarly, leading to bundles of parallel dislocation lines. Neighboring parallel dislocations with the same Burgers vector or with one rotated by 60° feel repulsive forces induced by the strain field. At equilibrium, this repulsive interaction would lead to a homogeneous distribution of the dislocations with maximized separations. Since this is not observed within the scope of the measurements, additional attractive forces have to be present. As stated in Reference [118], a similar problem occurred for repulsively screened Coulomb interactions between charged dopants in GaAs, which were also found to form agglomerations. Many-body effects in the repulsive interactions lead to effectively attractive pair interaction potentials, which induce agglomerations. Since strain interactions have a large range of interaction caused by their slow decay [119], many dislocations will interact simultaneously. These many-body effects in the *strain* interactions may induce an effective attractive force to the interactions between the dislocations cores which would otherwise be dominated by repulsive strain interactions. Ultimately, these effects lead to inhomogeneities in the distribution of dislocations which are in agreement with the agglomerations[4] of dislocations observed in Figure 15.2(b).

In addition to interactions between the dislocations themselves, there might also be interactions between dislocations and v-shaped defects. The distribution of dislocations shown in Figure 15.2(b) peaks for dislocations located in between the

[4]Some of the agglomerations consist of two intersecting bundles of dislocations with different line directions as can be seen by comparing Figures 15.2(b) and 15.4(c).

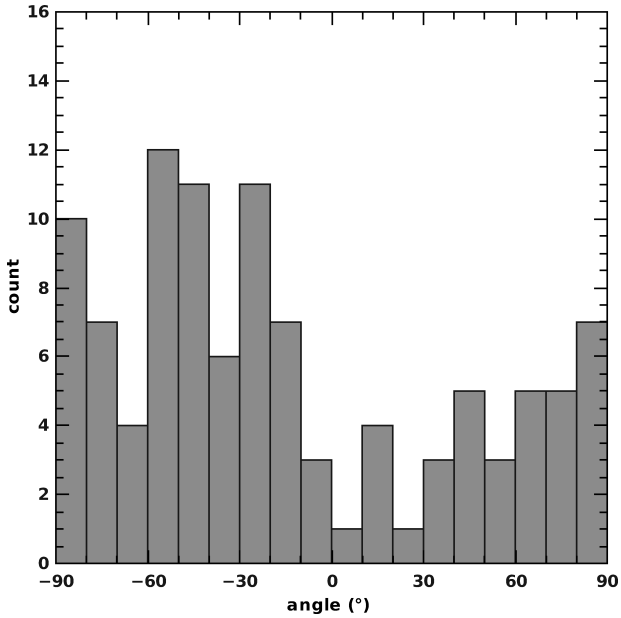

Figure 15.5. *Distribution of the orientation of the projected line directions of the dislocations relative to the [0001] c-direction at 0°. Nearly all dislocations are bent away from the c direction.*

v-shaped defects. The lowest concentration of dislocations in that cross-section is found in areas right at the core of the v-shaped defects. This is corroborated by the reduced dislocation density at v-shaped defects found on *c*-oriented growth planes [107]. These observations indicate a repulsive interaction between v-shaped defects and dislocations which bends the dislocations away from the v-shaped defect.

Previously, dislocations were found to bend toward inclined semipolar facets, i.e. the opposite direction than observed here [25, 26, 108, 110, 120, 121]. This effect can be traced to different strain structures: v-shaped defects in hydride vapor phase epitaxy grown GaN typically form around defect-induced growth instabilities [29, 96, 107], which introduce strain fields. For example, the presence of dislocations in these v-shaped defects is also indicated by their meandering behavior (Chapter 13). These dislocations induce strain effects. In contrast, wings in

epitaxial lateral overgrowth (ELO) are mostly free of defects and dislocations and their corresponding strain fields. In epitaxial lateral overgrowth, the minimization of the line length hence bends the dislocations lines *toward* the inclined facet. The strain fields in v-shaped defects, however, interact *repulsively* with the strain field of the surrounding dislocations and bend them *away* from inclined facets.

In conclusion, the spatial distribution and line directions of dislocations intersecting a cross-sectional cleavage surface were mapped. The correlation of the dislocation distribution and line directions with the spatial positions of v-shaped defects shows that the dislocations are bent away from the inclined semipolar facets of the v-shaped defects. The repulsive interaction between dislocations and v-shaped defects is traced to strain fields within the crystal lattice.

16. Analysis of dislocations

In this Chapter, a methodology for the determination of the intersection angle of a dislocation line is presented.

16.1. Determination of the intersection angle of the dislocation line

Within cross-sectional scanning tunneling microscopy, dislocations intersecting the surface can be identified by distinctive changes in contrast. The schematics of the imperfections in the crystal lattice caused by an edge dislocation are shown in Figure 16.1. The dislocation line is perpendicular to the shown two-dimensional plane. To generate the dislocation, two half-planes have been inserted in $+y$-direction, forming a (positive) line dislocation. The insertion of atomic half-planes locally disrupts the symmetry of the crystal lattice and hence exerts strain onto the crystal [123]. Koehler presented a formalism to quantify the strain [122]. This formalism is used to derive the effects of strain on surfaces imaged by STM. Following Koehler[1], an Airy stress function, χ, must satisfy the differential equation

$$\frac{\partial^4 \chi}{\partial x^4} + 2 \cdot \frac{\partial^4 \chi}{\partial x^2 \partial y^2} + \frac{\partial^4 \chi}{\partial y^4} = 0 \tag{16.1}$$

[1]The derivation of Equation 16.11 is made in analogy to [122].

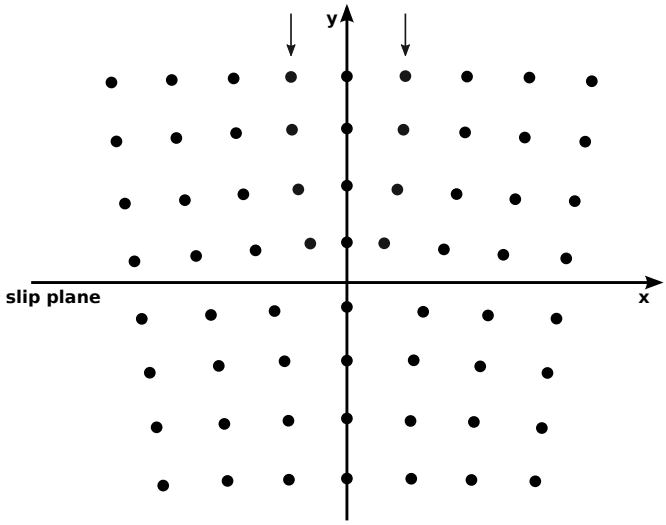

Figure 16.1. *Edge dislocation in a simple cubic crystal according to Koehler [122]. The dislocation line is perpendicular to the two-dimensional plane shown. To generate the dislocation, two half-planes have been inserted in +y-direction (see arrows), forming a (positive) line dislocation.*

and must yield stresses or displacements which satisfy the boundary conditions of the problem. The corresponding stresses are:

$$\sigma_x = \frac{\partial^2 \chi}{\partial y^2} \tag{16.2}$$

$$\sigma_y = \frac{\partial^2 \chi}{\partial x^2} \tag{16.3}$$

$$\tau_{xy} = -\frac{\partial^2 \chi}{\partial x \partial y} \tag{16.4}$$

An applicable stress function is[2]:

$$\chi = -Bxy - Dy \cdot \log(x^2 + y^2)^{\frac{1}{2}} \tag{16.5}$$

[2]For a derivation see Reference [123].

with the resulting stresses being:

$$\sigma_x = -Dy \cdot \frac{3x^2 + y^2}{(x^2 + y^2)^2} \tag{16.6}$$

$$\sigma_y = +Dy \cdot \frac{x^2 - y^2}{(x^2 + y^2)^2} \tag{16.7}$$

$$\tau_{xy} = +B + Dx \cdot \frac{x^2 - y^2}{(x^2 + y^2)^2} \tag{16.8}$$

Using Hooke's law, the resulting displacements are:

$$u = +\frac{m-1}{m \cdot G} \cdot D \cdot \arctan\left(\frac{y}{x}\right) + \frac{D}{2G} \cdot \frac{x \cdot y}{x^2 + y^2} \tag{16.9}$$

$$v = -\frac{m-2}{2m \cdot G} \cdot D \cdot \log(x^2 + y^2)^{\frac{1}{2}} - \frac{D}{2G} \cdot \frac{x^2}{x^2 + y^2} \tag{16.10}$$

where u and v are the displacements in x direction and y direction, respectively. G is the shear modulus of the material and $m = \frac{1}{\nu}$ is the reciprocal Poisson's ratio. Introducing the displacement λ (introduced by the Burgers vector), Equation 16.9 can be transformed into:

$$u = \frac{\lambda}{2\pi} \cdot \left(\arctan\left(\frac{y}{x}\right) + \frac{1}{2(1-\nu)} \cdot \frac{x \cdot y}{x^2 + y^2}\right) \tag{16.11}$$

with

$$D = \frac{m \cdot G \cdot \lambda}{2\pi(m-1)} \tag{16.12}$$

Figure 16.2 shows a dislocation intersecting the cleavage surface. The dislocation is marked by a dashed circle and the point of intersection is located at the center of this circle. As shown in Chapter 15, the projected line direction of such a dislocation can be measured by evaluating a derivative image of the dislocation. Yet, only the *projected* line direction is obtained using this method. In order to acquire information on the intersection angle of the dislocation line, Equation 16.11 will be utilized: When a dislocation line comes into close proximity to the cleavage surface (e.g. a coordinate close to the point of intersection), the surface material above the dislocation line will be deformed according to Equation 16.11. This

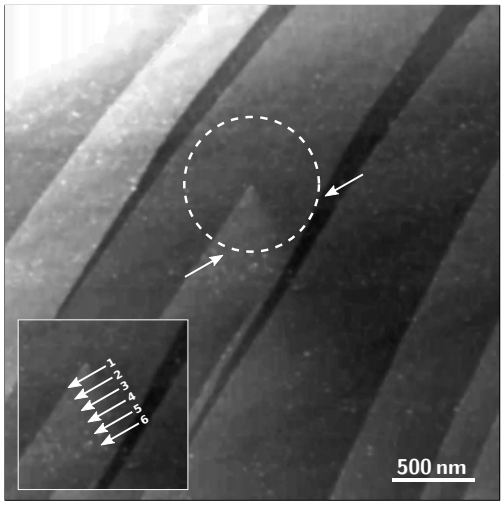

Figure 16.2. *STM image of a dislocation intersecting the GaN cleavage surface. The dislocation is marked by a dashed circle and the point of intersection is located at the center of the circle. Line profiles perpendicular to the projected line direction of the dislocation have been measured, as depicted in the inset.*

deformation can be seen by the contrast gradient in Figure 16.2: The contrast changes from darker to brighter (clockwise) in the lower right part of the circle. The change in contrast is caused by a change in height of the surface induced by the intersecting dislocation line.

For a quantitative analysis, only the edge part of the dislocation resulting in the displacement perpendicular to the surface is considered. An averaged line profile of the height along a straight line between the two arrows in Figure 16.2 perpendicular to the projected line direction is shown in Figure 16.3. The result of the application of Equation 16.11 onto the line profile in Figure 16.3 demonstrates that the Burgers vector of the investigated dislocation has a z-component of one monolayer. With the aim of determining the intersection angle of the dislocation line, n equidistant averaged line profiles are measured, each of them[3] covering the

[3]See inset of Figure 16.2, with each line representing an averaged profile covering the lateral distance of 1/6 of the distance between the center of the dashed circle and its border.

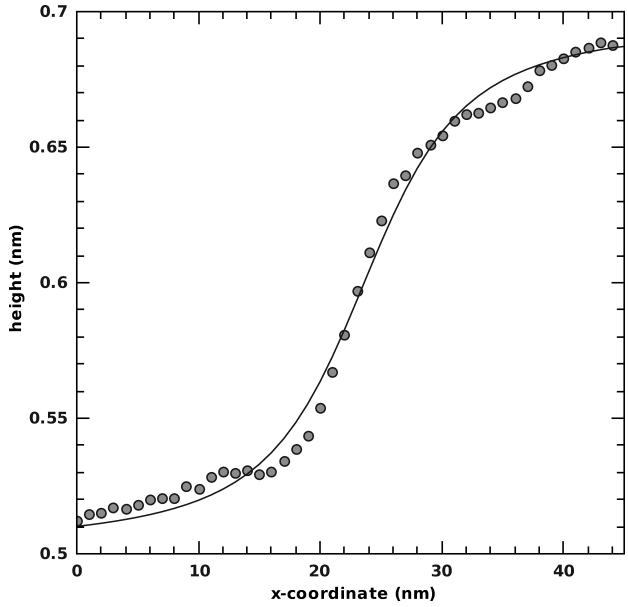

Figure 16.3. *Averaged line profile of the dislocation shown in Figure 16.2. The solid line is a fit of the formula in Equation 16.11 to the data (circles). The fit shows a good accordance with the data and yields a mean depth of the dislocation core of about 9 nm.*

same lateral distance of the projected line direction (see inset in Figure 16.2). The averaged equidistant line profiles for the dislocation shown in Figure 16.2 with $n = 6$ are presented in Figure 16.4.

The line profiles have different arbitrary y-offsets due to a slight gradient in the STM image (non plane parallel sample). These offsets are on the one hand compensated by the fitting algorithm and on the other hand enable a more facile distinction between the line profiles. By fitting Equation 16.11 to the different line profiles, the depth of each profile in relation to the surface can be obtained for the six different but equidistant positions along the projected line direction. These different depths are shown in Figure 16.5. The error on each depth is provided by the fitting algorithm and mainly depends on the noise of the image as well as on the number of averaged line profiles entering each of the six height profiles.

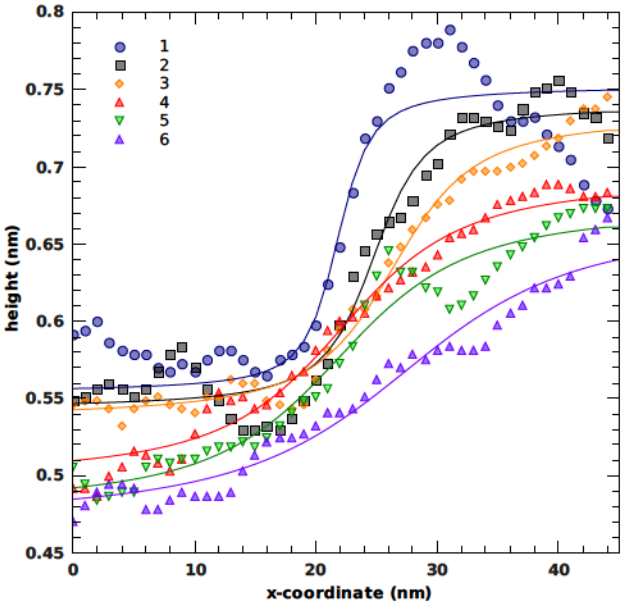

Figure 16.4. *Analyzed height profiles: The line profile of Figure 16.3 has been divided into six parts of equal distance, as shown in the inset in Figure 16.2. Afterward, the formula from Equation 16.11 has been fitted (solid lines) to each of the six height profiles to obtain the vertical position of the dislocation core below the surface. The first height profile (circles) represents a point on the dislocation line being in close proximity to the surface and has a shape close to a step function. The sixth profile (upright triangles) represents a point on the dislocation line farther away from the surface and has an almost linear shape because the extended displacement field of the dislocation.*

The points trace the subsurface position of the dislocation line. By fitting a linear slope to the depths of the line profiles, the actual intersection angle of the dislocation line can be measured (assuming a straight dislocation line). As can be seen from Figure 16.5, the dislocation shown in Figure 12.1 has an intersection angle of about -14°. The linear slope is in good accordance with the data, even with respect to the errors of the depth values. Using this method in combination with the method presented in Chapter 15, the three-dimensional angle of an edge dislocation intersecting the cleavage surface can be determined.

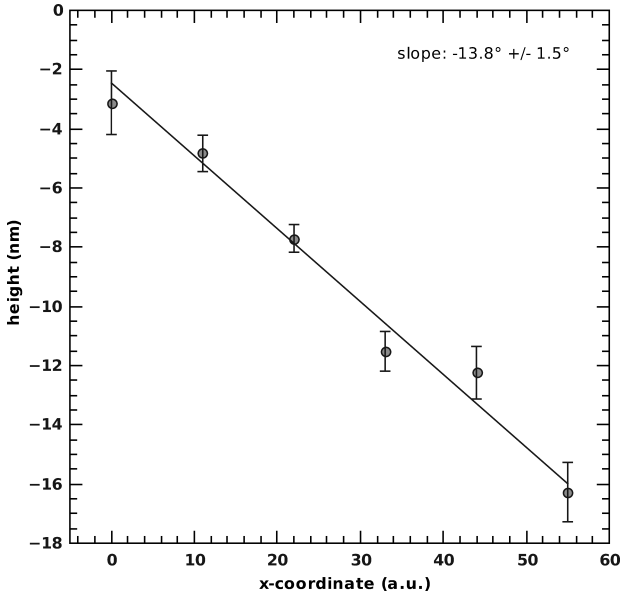

Figure 16.5. *Depth of the dislocation core below the surface as a function of the distance from the point of the dislocation intersecting the surface. By fitting Equation 16.11 to the height profiles in Figure 16.4, the depth of the dislocation can be obtained for the six different but equidistant positions along the projected line direction. The error on each depth is provided by the fitting algorithm and mainly depends on the noise of the image as well as on the number of averaged line profiles entering each of the six height profiles. Fitting a linear slope to the depths of the line profiles returns the actual intersection angle of the dislocation line of about -14˚.*

16.2. Simulation of the displacement field of a dislocation

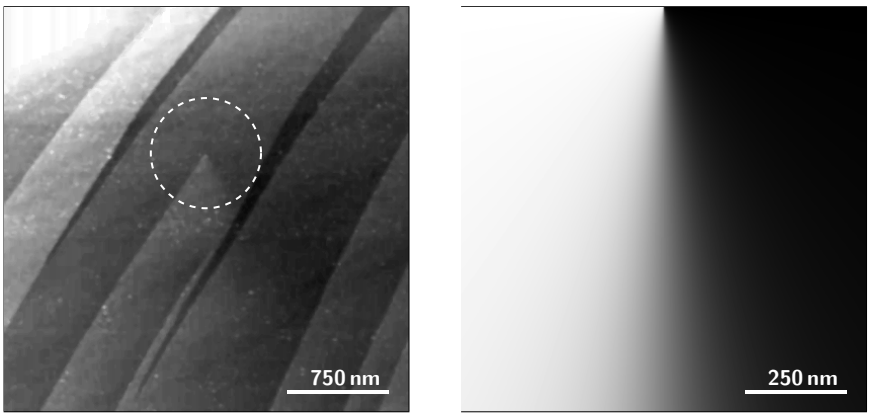

(a) Measurement (b) Simulation

Figure 16.6. *(a) Dislocation from Figure 16.2 intersecting the GaN cleavage surface marked by a dashed circle with the point of intersection being located at the center of the circle. (b) Simulated displacement filed of an edge dislocation with an intersection angle of 14° as obtained for (a) in Figure 16.5. Note the different length scale and rotation of both images.*

If there is no way of measuring a line profile as in Figure 16.3, i.e. if the resolution of the STM image is too small or if there is too much noise in the data, the formalism presented in this Chapter can still be used to qualitatively determine the intersection angle of the dislocation line. Computing the change in height of the surface induced by the dislocation line from Equation 16.11 for a set of different heights, i.e. values of height increasing or decreasing linearly, the arising change in contrast of the dislocation can be illustrated for any given intersection angle of the dislocation. The resulting image can then be compared to the noisy data, as shown in Figure 16.6, since the intersection angle of the dislocation line crucially changes

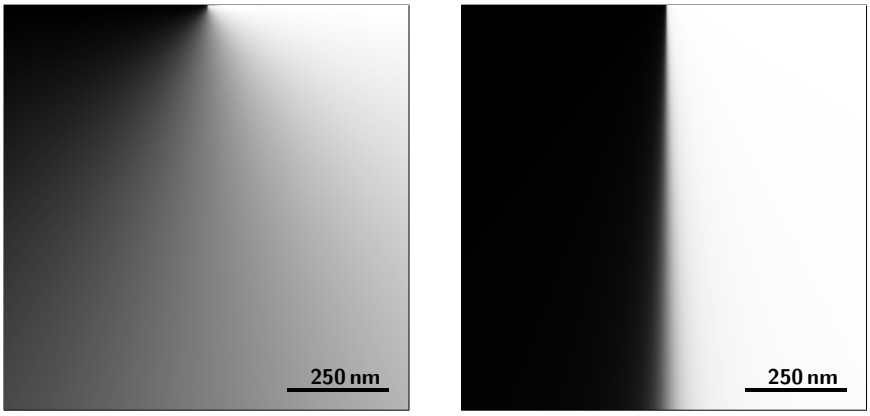

(a) Simulation: 50˚ (b) Simulation: 5˚

Figure 16.7. *Simulated displacement fields of two dislocations. (a) Edge dislocation intersecting the surface with an angle of 50˚. The contrast changes continuously from bright to dark in clockwise direction. (b) Edge dislocation intersecting the cleavage surface with an angle of 5˚. The gradient of contrast is still close to the one of a plain atomic step. Note the different length scale of both images.*

the gradient of the contrast: The closer to perpendicular[4] the angle becomes, the wider the distance (in circular measure) required for the gradient to change from its minimum to its maximum. A simulated edge dislocation with an intersection angle of 50˚ is shown in Figure 16.7(a), showing a continuous change in the contrast from bright to dark in clockwise direction. For very small angles, the gradient of contrast is like a step function comparable to the one of an atomic surface step, as shown by the simulation of a dislocation intersecting the cleavage surface at 5˚ (Figure 16.7(b)).

In summary, the angle between an edge dislocation and the cleavage surface can be approximated by comparing the simulated contrast of the intersecting dislocation with the measurement.

[4] A dislocation line perpendicularly intersecting the surface would be represented by an angle of 90˚. Due to the arc tangent in Equation 16.11, however, there is a singularity for this angle. Nonetheless, a perpendicular dislocation line would be easy to identify due to the gradient of contrast changing all over the 360˚ of the distance in circular measure.

17. Conclusion

The structure, electronic properties, and interactions of extended as well as micro-scale defects in [0001] grown GaN epitaxial layers were investigated using cross-sectional scanning tunneling microscopy (XSTM) and spectroscopy (XSTS).

First, the electronic structure of the cross-sectional GaN $(10\bar{1}0)$ surface was investigated in view of identifying defects by XSTM and interpreting XSTS data of defects. A new approach was developed to successfully probe the controversially debated minimum of the empty GaN $(10\bar{1}0)$ surface state utilizing the results of *ab initio* calculations to provide a set of experimental parameters. Using this new approach, the surface state was found to be located below the minimum of the conduction band and hence to be situated within the fundamental band gap. It has a surprisingly low density of states which is caused by an uncommon dispersion as well as by a special decay characteristic: One the one hand, there is a steep minimum with a low density of states near the $\bar{\Gamma}$ point and on the other hand an extremely flat area with a high density of states near the edge of the Brillouin Zone. As a consequence, the non-polar GaN $(10\bar{1}0)$ surface is intrinsically pinned at $(E_C - 0.6) \pm 0.2\,\mathrm{eV}$. The empty surface state in the fundamental band gap, however, does not inhibit a tip-induced band bending as it cannot be refilled with electrons since the surface state and the conduction band have the same azimuthal quantum number.

Second, the geometric and electronic structure of overgrown v-shaped defects in gallium nitride epitaxial layers was investigated by cross-sectional scanning tunneling microscopy and spectroscopy. By determination of their opening angle in the cross-sectional projection, the v-shaped defects were found to be three-dimensional hexagonal pyramidal structures defined by six inclined $\{11\bar{2}2\}$ growth facets. At their center, the v-shaped defects exhibit inhomogeneous electronic properties such

as an inhibited tunneling current caused by deep traps. These traps are blocking electrons from being injected into the conduction band of the GaN epitaxial layers when the tip is in close proximity to the center of a v-shaped defect.

By measuring large scale STM images of the cleavage surface, the v-shaped defects were found to exhibit a pronounced meandering around the growth (c-) direction. The v-shaped defects are supposedly meandering due to them tracing threading dislocations which themselves are alternating through the crystal. The interaction between the dislocation and the surrounding inhomogeneous strain fields is driving the meandering of the dislocation line. A quantitative analysis of the lateral displacements of the v-shaped defects leads to an estimated maximum line bending of c-screw dislocations of up to 26°.

Third, the large images also provided information on the spatial distribution and line directions of dislocations intersecting the cleavage surface. A comparison of the spatial distribution of the dislocations and their line directions revealed the dislocations being bent away from the semipolar facets of the v-shaped defects. The dislocations were found to form bundles of dislocations with parallel projected line directions. These agglomerations are caused by a line bending due to a minimization of energy as well as by many-body effects in the repulsive strain interactions.

For a better characterization of dislocations, a method for the determination of the angle between the line of a dislocation intersecting the surface and the cleavage surface itself was presented within this study. By mapping the displacement field arising from a dislocation intersecting the surface, the depth of the dislocation core below the surface was extracted for discrete distances from the point of intersection. This yielded the intersection angle of the dislocation line.

Bibliography

[1] I. Vurgaftman and J. R. Meyer. “Band parameters for nitrogen-containing semiconductors”. In: *Journal of Applied Physics* **94** (2003), 3675–3696.

[2] S. Nakamura, M. Senoh, S. Nagahama, N. Iwasa, T. Yamada, T. Matsushita, H. Kiyoku, and Y. Sugimoto. “Characteristics of InGaN multi-quantum-well-structure laser diodes”. In: *Applied Physics Letters* **68** (1996), 3269–3271.

[3] P. Gibart. “Metal organic vapour phase epitaxy of GaN and lateral overgrowth”. In: *Reports on Progress in Physics* **67** (2004), 667–715.

[4] I. Grzegory, B. Łucznik, M. Boćkowski, and S. Porowski. “Crystallization of low dislocation density GaN by high-pressure solution and HVPE methods”. In: *Journal of Crystal Growth* **300** (2007), 17–25.

[5] J. C. Moore, V. Kasliwal, A. A. Baski, X. Ni, U. Ozgur, and H. Morkoc. “Local electronic and optical behaviors of a-plane GaN grown via epitaxial lateral overgrowth”. In: *Applied Physics Letters* **90** (2007), 011913.

[6] F. A. Ponce, D. P. Bour, W. Gotz, and P. J. Wright. “Spatial distribution of the luminescence in GaN thin films”. In: *Applied Physics Letters* **68** (1996), 57–59.

[7] J. Cai and F. Ponce. “Determination by Electron Holography of the Electronic Charge Distribution at Threading Dislocations in Epitaxial GaN”. In: *physica status solidi (a)* **192** (2002), 407–411.

[8] G. Koley and M. G. Spencer. “Scanning Kelvin probe microscopy characterization of dislocations in III-nitrides grown by metalorganic chemical vapor deposition”. In: *Applied Physics Letters* **78** (2001), 2873–2875.

[9] P. J. Hansen, Y. E. Strausser, A. N. Erickson, E. J. Tarsa, P. Kozodoy, E. G. Brazel, J. P. Ibbetson, U. Mishra, V. Narayanamurti, S. P. DenBaars, and J. S. Speck. "Scanning capacitance microscopy imaging of threading dislocations in GaN films grown on (0001) sapphire by metalorganic chemical vapor deposition". In: *Applied Physics Letters* **72** (1998), 2247–2249.

[10] J. W. P. Hsu, H. M. Ng, A. M. Sergent, and S. N. G. Chu. "Scanning Kelvin force microscopy imaging of surface potential variations near threading dislocations in GaN". In: *Applied Physics Letters* **81** (2002), 3579–3581.

[11] M. Albrecht, J. L. Weyher, B. Lucznik, I. Grzegory, and S. Porowski. "Nonradiative recombination at threading dislocations in n-type GaN: Studied by cathodoluminescence and defect selective etching". In: *Applied Physics Letters* **92** (2008), 231909.

[12] A. Krtschil, A. Dadgar, and A. Krost. "Decoration effects as origin of dislocation-related charges in gallium nitride layers investigated by scanning surface potential microscopy". In: *Applied Physics Letters* **82** (2003), 2263–2265.

[13] D. Cherns and C. G. Jiao. "Electron Holography Studies of the Charge on Dislocations in GaN". In: *Phys. Rev. Lett.* **87** (2001), 205504.

[14] Ph. Ebert, L. Ivanova, S. Borisova, H. Eisele, A. Laubsch, and M. Dähne. "Electronic properties of dislocations in GaN investigated by scanning tunneling microscopy". In: *Applied Physics Letters* **94** (2009), 062104.

[15] J. Elsner, R. Jones, P. K. Sitch, V. D. Porezag, M. Elstner, T. Frauenheim, M. I. Heggie, S. Öberg, and P. R. Briddon. "Theory of Threading Edge and Screw Dislocations in GaN". In: *Phys. Rev. Lett.* **79** (1997), 3672–3675.

[16] Y. Xin, S. J. Pennycook, N. D. Browning, P. D. Nellist, S. Sivananthan, F. Omnes, B. Beaumont, J. P. Faurie, and P. Gibart. "Direct observation of the core structures of threading dislocations in GaN". In: *Applied Physics Letters* **72** (1998), 2680–2682.

[17] A. F. Wright and U. Grossner. "The effect of doping and growth stoichiometry on the core structure of a threading edge dislocation in GaN". In: *Applied Physics Letters* **73** (1998), 2751–2753.

[18] J. E. Northrup. “Theory of intrinsic and H-passivated screw dislocations in GaN”. In: *Phys. Rev. B* **66** (2002), 045204.

[19] I. Arslan, A. Bleloch, E. A. Stach, and N. D. Browning. “Atomic and Electronic Structure of Mixed and Partial Dislocations in GaN”. In: *Phys. Rev. Lett.* **94** (2005), 025504.

[20] L. Lymperakis, J. Neugebauer, M. Albrecht, T. Remmele, and H. P. Strunk. “Strain Induced Deep Electronic States around Threading Dislocations in GaN”. In: *Phys. Rev. Lett.* **93** (2004), 196401.

[21] A. T. Blumenau, J. Elsner, R. Jones, M. I. Heggie, S. Öberg, T. Frauenheim, and P. R. Briddon. “Dislocations in hexagonal and cubic GaN”. In: *Journal of Physics: Condensed Matter* **12** (2000), 10223–10233.

[22] P. H. Weidlich, M. Schnedler, H. Eisele, U. Strauss, R. E. Dunin-Borkowski, and Ph. Ebert. “Evidence of deep traps in overgrown v-shaped defects in epitaxial GaN layers”. In: *Applied Physics Letters* **103** (2013), 062101.

[23] A. Usui, H. Sunakawa, A. Sakai, and A. Yamaguchi. “Thick GaN Epitaxial Growth with Low Dislocation Density by Hydride Vapor Phase Epitaxy”. In: *Japanese Journal of Applied Physics* **36** (1997), L899–L902.

[24] H. Nam, M. D. Bremser, T. S. Zheleva, and R. F. Davis. “Lateral epitaxy of low defect density GaN layers via organometallic vapor phase epitaxy”. In: *Applied Physics Letters* **71** (1997), 2638–2640.

[25] P. Vennéguès, B. Beaumont, V. Bousquet, M. Vaille, and P. Gibart. “Reduction mechanisms for defect densities in GaN using one- or two-step epitaxial lateral overgrowth methods”. In: *Journal of Applied Physics* **87** (2000), 4175–4181.

[26] K. Hiramatsu, K. Nishiyama, M. Onishi, H. Mizutani, M. Narukawa, A. Motogaito, H. Miyake, Y. Iyechika, and T. Maeda. “Fabrication and characterization of low defect density GaN using facet-controlled epitaxial lateral overgrowth (FACELO)”. In: *Journal of Crystal Growth* **221** (2000), 316–326.

[27] A. Krost and A. Dadgar. “GaN-Based Devices on Si”. In: *physica status solidi (a)* **194** (2002), 361–375.

[28] A. Dadgar, M. Poschenrieder, J. Blasing, K. Fehse, A. Diez, and A. Krost. "Thick, crack-free blue light-emitting diodes on Si(111) using low-temperature AlN interlayers and in situ Si_xN_y masking". In: *Applied Physics Letters* **80** (2002), 3670–3672.

[29] K. Motoki, T. Okahisa, S. Nakahata, N. Matsumoto, H. Kimura, H. Kasai, K. Takemoto, K. Uematsu, M. Ueno, Y. Kumagai, A. Koukitu, and H. Seki. "Growth and characterization of freestanding GaN substrates". In: *Journal of Crystal Growth* **237–239** (2002), 912–921.

[30] V. Wagner, O. Parillaud, H. J. Bühlmann, M. Ilegems, S. Gradeçak, P. Stadelmann, T. Riemann, and J. Christen. "Influence of the carrier gas composition on morphology, dislocations, and microscopic luminescence properties of selectively grown GaN by hydride vapor phase epitaxy." In: *Journal of Applied Physics* **92** (2002), 1307–1316.

[31] K. Pakuła, R. Bożek, J. Baranowski, J. Jasinski, and Z. Liliental-Weber. "Reduction of dislocation density in heteroepitaxial GaN: role of SiH4 treatment". In: *Journal of Crystal Growth* **267** (2004), 1–7.

[32] S. Bohyama, H. Miyake, K. Hiramatsu, Y. Tsuchida, and T. Maeda. "Freestanding GaN Substrate by Advanced Facet-Con trolled Epitaxial Lateral Overgrowth Technique with Masking Side Facets". In: *Japanese Journal of Applied Physics* **44** (2005), L24–L26.

[33] M. Ali, A. Romanov, S. Suihkonen, O. Svensk, S. Sintonen, M. Sopanen, H. Lipsanen, V. Nevedomsky, N. Bert, M. Odnoblyudov, and V. Bougrov. "Analysis of threading dislocations in void shape controlled GaN re-grown on hexagonally patterned mask-less GaN". In: *Journal of Crystal Growth* **344** (2012), 59–64.

[34] A. Béré and A. Serra. "On the atomic structures, mobility and interactions of extended defects in GaN: dislocations, tilt and twin boundaries". In: *Philosophical Magazine* **86** (2006), 2159–2192.

[35] O. Contreras, F. Ponce, J. Christen, A. Dadgar, and A. Krost. "Dislocation annihilation by silicon delta-doping in GaN epitaxy on Si". In: *Applied Physics Letters* **81** (2002), 4712–4714.

[36] F. Y. Meng and S. Mahajan. "Dislocation reactions in hetero-epitaxial (0001) GaN layers". In: *physica status solidi (a)* **208** (2011), 2666–2670.

[37] P. H. Weidlich, M. Schnedler, H. Eisele, R. E. Dunin-Borkowski, and Ph. Ebert. "Repulsive interactions between dislocations and overgrown v-shaped defects in epitaxial GaN layers". In: *Applied Physics Letters* **103** (2013), 142105.

[38] W. Nolting. *Grundkurs Theoretische Physik 5/1*. 7th ed. Heidelberg: Springer, 2009.

[39] J. Bardeen. "Tunnelling from a many-particle point of view". In: *Physical Review Letters* **6** (1961), 57–59.

[40] P. Dirac. "The question theory of the emission and absorption of radiation". In: *Proceedings of the Royal Society of London Series A* **114** (1927), 243–265.

[41] G. Wentzel. "Über strahlungslose Quantensprünge". In: *Zeitschrift für Physik* **43** (1927), 524–530.

[42] J. Tersoff and D. R. Hamann. "Theory and Application for the Scanning Tunneling Microscope". In: *Physical Review Letters* **50** (1983), 1998–2001.

[43] J. Tersoff and D. R. Hamann. "Theory of the scanning tunneling microscope". In: *Physical Review B* **31** (1985), 805–813.

[44] R. J. Hamers and D. F. Padowitz. *'Methods of Tunneling Spectroscopy with the STM' from Scanning Probe Microscopy and Spectroscopy: Theory, Techniques, and Applications*. 2nd ed. New York: Wiley-VCH, 2001.

[45] E. Fermi. "Zur Quantelung des idealen einatomigen Gases". German. In: *Zeitschrift für Physik* **36** (1926), 902–912.

[46] S. M. Sze and K. K. Ng. *Physics of Semiconductor Devices*. 3rd ed. New York: Wiley-Interscience, 2007.

[47] Y. Varshni. "Temperature dependence of the energy gap in semiconductors". In: *Physica* **34** (1967), 149–154.

[48] D. Krüger, S. Kuhr, T. Schmidt, D. Hommel, and J. Falta. "Atomic structure of the non-polar GaN($\bar{2}$110) surface by cross-sectional scanning tunneling microscopy". In: *physica status solidi (RRL) – Rapid Research Letters* **3** (2009), 91–93.

[49] Y. R. Wang, C. R. Duke, K. Stevens, A. Kahn, K. O. Magnusson, and S. A. Flodström. "Photoemission from surface states on the (10$\bar{1}$0) and (11$\bar{2}$0) surfaces of CdSe". In: *Surface Science* **206** (1988), L817–L823.

[50] Y. Wang, C. Duke, and C. Mailhiot. "Electronic and atomic structure of cleavage faces of ZnSe". In: *Surface Science* **188** (1987), L708–L716.

[51] G. Binnig and D. P. E. Smith. "Single-tube three-dimensional scanner for scanning tunneling microscopy". In: *Review of Scientific Instruments* **57** (1986), 1688–1689.

[52] M. Schnedler, P. H. Weidlich, V. Portz, D. Weber, R. Dunin-Borkowski, and Ph. Ebert. "Correction of nonlinear lateral distortions of scanning probe microscopy images". In: *Ultramicroscopy* **136** (2014), 86–90.

[53] M. Schnedler and P. H. Weidlich. *STM Analyzer*.

[54] K. Bertness, A. Roshko, L. Mansfield, T. Harvey, and N. Sanford. "Nucleation conditions for catalyst-free GaN nanowires". In: *Journal of Crystal Growth* **300** (2007), 94–99.

[55] L. Largeau, D. L. Dheeraj, M. Tchernycheva, G. E. Cirlin, and J. C. Harmand. "Facet and in-plane crystallographic orientations of GaN nanowires grown on Si(111)". In: *Nanotechnology* **19** (2008), 155704.

[56] H. Eisele and Ph. Ebert. "Non-polar group-III nitride semiconductor surfaces". In: *physica status solidi (RRL) Rapid Research Letters* **6** (2012), 359–369.

[57] J. E. Northrup and J. Neugebauer. "Theory of GaN(10$\bar{1}$0) and (11$\bar{2}$0) surfaces". In: *Physical Review B* **53** (1996), R10477–R10480.

[58] M. Bertelli, P. Löptien, M. Wenderoth, A. Rizzi, R. G. Ulbrich, M. C. Righi, A. Ferretti, L. Martin-Samos, C. M. Bertoni, and A. Catellani. "Atomic and electronic structure of the nonpolar GaN($1\bar{1}00$) surface". In: *Physical Review B* **80** (2009), 115324.

[59] D. Segev and C. G. Van de Walle. "Origins of Fermi-level pinning on GaN and InN polar and nonpolar surfaces". In: *EPL (Europhysics Letters)* **76** (2006), 305–311.

[60] C. G. Van de Walle and D. Segev. "Microscopic origins of surface states on nitride surfaces". In: *Journal of Applied Physics* **101** (2007), 081704.

[61] T. Paskova, E. M. Goldys, R. Yakimova, E. B. Svedberg, A. Henry, and B. Monemar. "Influence of growth rate on the structure of thick GaN layers grown by HVPE". In: *Journal of Crystal Growth* **208** (2000), 18–26.

[62] L. Lymperakis, P. H. Weidlich, H. Eisele, M. Schnedler, J.-P. Nys, B. Grandidier, D. Stievenard, R. E. Dunin-Borkowski, J. Neugebauer, and Ph. Ebert. "Hidden surface states at non-polar GaN ($10\bar{1}0$) facets: Intrinsic pinning of nanowires". In: *Applied Physics Letters* **103** (2013), 152101.

[63] B. Siemens, C. Domke, P. Ebert, and K. Urban. "Electronic structure of wurtzite II-VI compound semiconductor cleavage surfaces studied by scanning tunneling microscopy". In: *Phys. Rev. B* **56** (1997), 12321–12326.

[64] R. Feenstra, J. A. Stroscio, and A. Fein. "Tunneling spectroscopy of the Si(111)2 $\times$ 1 surface". In: *Surface Science* **181** (1987), 295–306.

[65] R. Dombrowski, C. Steinebach, C. Wittneven, M. Morgenstern, and R. Wiesendanger. "Tip-induced band bending by scanning tunneling spectroscopy of the states of the tip-induced quantum dot on InAs(110)". In: *Physical Review B* **59** (1999), 8043–8048.

[66] M. Wenderoth, M. A. Rosentreter, K. J. Engel, A. J. Heinrich, M. A. Schneider, and R. G. Ulbrich. "Low-temperature scanning tunneling spectroscopy as a probe for a confined electron gas". In: *EPL (Europhysics Letters)* **45** (1999), 579–584.

[67] G. Kresse and J. Hafner. "Ab initio molecular dynamics for liquid metals". In: *Physical Review B* **47** (1993), 558–561.

[68] G. Kresse and J. Furthmüller. "Efficient iterative schemes for ab initio total-energy calculations using a plane-wave basis set". In: *Physical Review B* **54** (1996), 11169–11186.

[69] A. Janotti, D. Segev, and C. G. Van de Walle. "Effects of cation *d* states on the structural and electronic properties of III-nitride and II-oxide wide-band-gap semiconductors". In: *Physical Review B* **74** (2006), 045202.

[70] G. P. Kerker. "Efficient iteration scheme for self-consistent pseudopotential calculations". In: *Physical Review B* **23** (1981), 3082–3084.

[71] B. Engels, P. Richard, K. Schroeder, S. Blügel, Ph. Ebert, and K. Urban. "Comparison between *ab initio* theory and scanning tunneling microscopy for (110) surfaces of III-V semiconductors". In: *Physical Review B* **58** (1998), 7799–7815.

[72] P. Mårtensson and R. M. Feenstra. "Geometric and electronic structure of antimony on the GaAs(110) surface studied by scanning tunneling microscopy". In: *Physical Review B* **39** (1989), 7744–7753.

[73] V. Ramachandran and R. M. Feenstra. "Scanning Tunneling Spectroscopy of Mott-Hubbard States on the 6*H*-SiC(0001) $\sqrt{3} \times \sqrt{3}$ Surface". In: *Physical Review Letters* **82** (1999), 1000–1003.

[74] S. E. Bennett. "Dislocations and their reduction in GaN". In: *Materials Science and Technology* **26** (2010), 1017–1028.

[75] Z. Liliental-Weber, Y. Chen, S. Ruvimov, and J. Washburn. "Formation Mechanism of Nanotubes in GaN". In: *Physical Review Letters* **79** (1997), 2835–2838.

[76] Y. Chen, T. Takeuchi, H. Amano, I. Akasaki, N. Yamada, Y. Kaneko, and S. Y. Wang. "Pit formation in GaInN quantum wells". In: *Applied Physics Letters* **72** (1998), 710–712.

[77] X. H. Wu, C. R. Elsass, A. Abare, M. Mack, S. Keller, P. M. Petroff, S. P. DenBaars, J. S. Speck, and S. J. Rosner. "Structural origin of V-defects and correlation with localized excitonic centers in InGaN/GaN multiple quantum wells". In: *Applied Physics Letters* **72** (1998), 692–694.

[78] T. Paskova, E. M. Goldys, and B. Monemar. “Hybride vapour-phase epitaxy growth and cathodoluminescence characterisation of thick GaN films”. In: *Journal of Crystal Growth* **203** (1999), 1–11.

[79] T. Riemann, J. Christen, B. Beaumont, J.-P. Faurie, and P. Gibart. “Self-organized domain formation in low-dislocation-density GaN”. In: *Superlattices and Microstructures* **36** (2004), 833–847.

[80] W. Lee, H. J. Lee, S. H. Park, K. Watanabe, K. Kumagai, T. Yao, J. H. Chang, and T. Sekiguchi. “Cross sectional CL study of the growth and annihilation of pit type defects in HVPE grown (0001) thick GaN”. In: *Journal of Crystal Growth* **351** (2012), 83–87.

[81] A. Lochthofen, W. Mertin, G. Bacher, L. Hoeppel, S. Bader, J. Off, and B. Hahn. “Electrical investigation of V-defects in GaN using Kelvin probe and conductive atomic force microscopy”. In: *Applied Physics Letters* **93** (2008), 022107.

[82] M. Herrera, A. Cremades, M. Stutzmann, and J. Piqueras. “Electrical properties of pinholes in GaN:Mn epitaxial films characterized by conductive AFM”. In: *Superlattices and Microstructures* **45** (2009), 435–443.

[83] P. H. Weidlich, R. E. Dunin-Borkowski, and Ph. Ebert. “Quantitative determination of local potential values in inhomogeneously doped semiconductors by scanning tunneling microscopy”. In: *Physical Review B* **84** (2011), 085210.

[84] H. Eisele, L. Ivanova, S. Borisova, M. Dähne, M. Winkelnkemper, and Ph. Ebert. “Doping modulation in GaN imaged by cross-sectional scanning tunneling microscopy”. In: *Applied Physics Letters* **94** (2009), 162110.

[85] J. Elsner, R. Jones, M. Haugk, R. Gutierrez, T. Frauenheim, M. I. Heggie, S. Öberg, and P. R. Briddon. “Effect of oxygen on the growth of (100) GaN surfaces: The formation of nanopipes”. In: *Applied Physics Letters* **73** (1998), 3530–3532.

[86] C. L. Progl, C. M. Parish, J. P. Vitarelli, and P. E. Russell. "Analysis of V defects in GaN-based light emitting diodes by scanning transmission electron microscopy and electron beam induced current". In: *Applied Physics Letters* **92** (2008), 242103.

[87] N. Sharma, P. Thomas, D. Tricker, and C. Humphreys. "Chemical mapping and formation of V-defects in InGaN multiple quantum wells". In: *Applied Physics Letters* **77** (2000), 1274–1276.

[88] A. M. Sánchez, M. Gass, A. J. Papworth, P. J. Goodhew, P. Singh, P. Ruterana, H. K. Cho, R. J. Choi, and H. J. Lee. "V-defects and dislocations in InGaN/GaN heterostructures". In: *Thin Solid Films* **479** (2005), 316–320.

[89] M. C. Johnson, Z. Lilienthal-Weber, D. N. Zakhariv, D. E. McCready, R. J. Jorgenson, J. Wu, W. Shan, and E. D. Bourret-Courchesne. "Investigation of Microstructure and V-Defect Formation in $In_xGa_{1-x}N$/GaN MQW Grown Using Temperature-Gradient Metalorganic Chemical Vapor Deposition". In: *Journal of Electronic Materials* **34** (2005), 605–611.

[90] H.-L. Tsai, T.-Y. Wang, J.-R. Yang, C.-C. Chuo, J.-T. Hsu, Z.-C. Feng, and M. Shiojiri. "Observation of V Defects in Multiple InGaN/GaN Quantum Well Layers". In: *Materials Transactions* **48** (2007), 894–898.

[91] J.-R. Yang, W.-C. Li, H.-L. Tsai, J.-T. Hsu, and M. Shiojiri. "Electron microscopy investigations of V defects in multiple InGaN/GaN quantum wells and InGaN quantum dots". In: *Journal of Microscopy* **237** (2010), 275–281.

[92] B. Pécz, Z. Makkai, M. A. di Forte-Poisson, F. Huet, and R. E. Dunin-Borkowski. "V-shaped defects connected to in inversion domains in AlGaN layers". In: *Applied Physics Letters* **78** (2001), 1529–1531.

[93] A. Hangleiter, F. Hitzel, C. Netzel, D. Fuhrmann, U. Rossow, G. Ade, and P. Hinze. "Suppression of Nonradiative Recombination by V-Shaped Pits in GaInN/GaN Quantum Wells Produces a Large Increase in the Light Emission Efficiency". In: *Physical Review Letters* **95** (2005), 127402.

[94] Z. Liliental-Weber, M. Benamara, W. Swider, J. Washburn, I. Grzegory, S. Porowski, R. D. Dupuis, and C. J. Eiting. "Ordering in bulk GaN : Mg samples: defects caused by Mg doping". In: *Physica B* **273-274** (1999), 124–129.

[95] L. Zhou, M. R. McCartney, D. J. Smith, A. Mouti, E. Feltin, J. F. Carlin, and N. Grandjean. "Observation of dodecagon-shape V-defects in GaN/ AlInN multiple quantum wells". In: *Applied Physics Letters* **97** (2010), 161902.

[96] E. Richter, U. Zeimer, S. Hagedorn, M. Wagner, F. Brunner, M. Weyers, and G. Tränkle. "Hydride vapor phase epitaxy of GaN boules using high growth rates". In: *Journal of Crystal Growth* **312** (2010), 2537–2541.

[97] J. Bono and R. H. Good. "Theoretical discussion of the scanning tunneling microscope applied to a semiconductor surface". In: *Surface Science* **175** (1986), 415–420.

[98] R. M. Feenstra. "Electrostatic Potential for a Hyperbolic Probe Tip near a Semiconductor". In: *Journal of Vacuum Science & Technology B* **21** (2003), 2080–2096.

[99] R. M. Feenstra, S. Gaan, G. Meyer, and K. H. Rieder. "Low-temperature tunneling spectroscopy of Ge(111) c(2x8) surfaces". In: *Physical Review B* **71** (2005), 125316.

[100] R. M. Feenstra, Y. Dong, M. P. Semtsiv, and W. T. Masselink. "Influence of Tip-induced Band Bending on Tunneling Spectra of Semiconductor Surfaces". In: *Nanotechnology* **18** (2007), 044015.

[101] Y. Dong, R. M. Feenstra, M. P. Semtsiv, and W. T. Masselink. "Band Offsets of InGaP/GaAs Heterojunctions by Scanning Tunneling Spectroscopy". In: *Journal of Applied Physics* **103** (2008), 073704.

[102] N. Ishida, K. Sueoka, and R. M. Feenstra. "Influence of surface states on tunneling spectra of n-type GaAs(110) surfaces". In: *Physical Review B* **80** (2009), 075320.

[103] S. Gaan, G. He, R. M. Feenstra, J. Walker, and E. Towe. "Size, shape, composition, and electronic properties of InAs/GaAs quantum dots by scanning tunneling microscopy and spectroscopy". In: *Journal of Applied Physics* **108** (2010), 114315.

[104] R. M. Feenstra. *SEMITIP version 6*. 2011.

[105] N. D. Jäger, E. R. Weber, K. Urban, and Ph. Ebert. "Importance of carrier dynamics and conservation of momentum in atom-selective STM imaging and band gap determination of GaAs(110)". In: *Physical Review B* **67** (2003), 165327.

[106] L. C. Le, D. G. Zhao, D. S. Jiang, L. Li, L. L. Wu, P. Chen, Z. S. Liu, Z. C. Li, Y. M. Fan, J. J. Zhu, H. Wang, S. M. Zhang, and H. Yang. "Carriers capturing of V-defect and its effect on leakage current and electroluminescence in InGaN-based light-emitting diodes". In: *Applied Physics Letters* **101** (2012), 252110.

[107] J. Weyher, B. Łucznik, I. Grzegory, J. Smalc-Koziorowska, and T. Paskova. "Revealing extended defects in HVPE-grown GaN". In: *Journal of Crystal Growth* **312** (2010), 2611–2615.

[108] A. Sakai, H. Sunakawa, and A. Usui. "Transmission electron microscopy of defects in GaN films formed by epitaxial lateral overgrowth". In: *Applied Physics Letters* **73** (1998), 481–483.

[109] E. Feltin, B. Beaumont, P. Vennéguès, M. Vaille, P. Gibart, T. Riemann, J. Christen, L. Dobos, and B. Pécz. "Epitaxial lateral overgrowth of GaN on Si (111)". In: *Journal of Applied Physics* **93** (2003), 182–185.

[110] A. E. Romanov, P. Fini, and J. S. Speck. "Modeling the extended defect evolution in lateral epitaxial overgrowth of GaN: Subgrain stability". In: *Journal of Applied Physics* **93** (2003), 106–114.

[111] X. H. Wu, L. M. Brown, D. Kapolnek, S. Keller, B. Keller, S. P. DenBaars, and J. S. Speck. "Defect structure of metal-organic chemical vapor deposition-grown epitaxial (0001) GaN/Al_2O_3". In: *Journal of Applied Physics* **80** (1996), 3228–3237.

[112] N. Grandjean, J. Massies, P. Vennéguès, M. Leroux, F. Demangeot, M. Renucci, and J. Frandon. "Molecular-beam epitaxy of gallium nitride on (0001) sapphire substrates using ammonia". In: *Journal of Applied Physics* **83** (1998), 1379–1383.

[113] D. Hull and D. J. Bacon. *Introduction to Dislocations*. 5th ed. Amsterdam: Elsevier, 2011.

[114] S. Gradeçak, P. Stadelmann, V. Wagner, and M. Ilegems. "Bending of dislocations in GaN during epitaxial lateral overgrowth". In: *Applied Physics Letters* **85** (2004), 4648–4650.

[115] A. R. Smith, V. Ramachandran, R. M. Feenstra, D. W. Greve, M.-S. Shin, M. Skowronski, J. Neugebauer, and J. E. Northrup. "Wurtzite GaN surface structures studied by scanning tunneling microscopy and reflection high energy electron diffraction". In: *Journal of Vacuum Science & Technology A* **16** (1998), 1641–1645.

[116] M. Khoury, A. Courville, B. Poulet, M. Teisseire, E. Beraudo, M. J. Rashid, E. Frayssinet, B. Damilano, F. Semond, O. Tottereau, and P. Vennéguès. "Imaging and counting threading dislocations in c-oriented epitaxial GaN layers". In: *Semiconductor Science and Technology* **28** (2013), 035006.

[117] H. Miyake, R. Takeuchi, K. Hiramatsu, H. Naoi, Y. Iyechika, T. Maeda, T. Riemann, F. Bertram, and J. Christen. "High Quality GaN Grown by Facet-Controlled ELO (FACELO) Technique". In: *physica status solidi (a)* **194** (2002), 545–549.

[118] Ph. Ebert, T. Zhang, F. Kluge, M. Simon, Z. Zhang, and K. Urban. "Importance of Many-Body Effects in the Clustering of Charged Zn Dopant Atoms in GaAs". In: *Physical Review Letters* **83** (1999), 757–760.

[119] S. Mathis, A. Romanov, L. Chen, G. Beltz, W. Pompe, and J. Speck. "Modeling of threading dislocation reduction in growing GaN layers". In: *Journal of Crystal Growth* **231** (2001), 371–390.

[120] R. Datta and C. J. Humphreys. "Mechanisms of bending of threading dislocations in MOVPE-grown GaN on (0001) sapphire". In: *physica status solidi (c)* **3** (2006), 1750–1753.

[121] J. K. Farrer and C. B. Carter. “Defect structure in GaN pyramids”. English. In: *Journal of Materials Science* **41** (2006), 779–792.

[122] J. S. Koehler. “On the Dislocation Theory of Plastic Deformation”. In: *Physical Review* **60** (1941), 397–410.

[123] G. I. Taylor. “The Mechanism of Plastic Deformation of Crystals. Part I. Theoretical”. In: *Proceedings of the Royal Society of London. Series A* **145** (1934), 362–387.

List of Figures

2.1. Quantum mechanical tunneling in one dimension 14
2.2. Probe tip 17
2.3. Schematic band structure 19

3.1. Topview of wurtzite GaN 24
3.2. GaN surface Brillouin zones 25

4.1. Sample preparation 28
4.2. Measurement 30
4.3. Calibration pattern 32
4.4. Corrected image of the calibration sample 33
4.5. Corrected STM image 34

5.1. GaN samples 37
5.2. Laue diffraction image 38

7.1. Averaged height profile 44
7.2. Normalized differential conductivity spectrum 45

8.1. Crystal structure wurtzite GaN 48
8.2. Band structure of the relaxed GaN $(10\bar{1}0)$ surface 49
8.3. Integrated partial charge density 51
8.4. Decay of the partial charge density 52
8.5. Decay of the surface state 53

9.1. Scanning tunneling spectrum 56
9.2. Tip-sample separation 57
9.3. Optimized normalized differential conductivity spectrum 58

11.1. Modulation of the contrast 66
11.2. Modulation of the contrast at different gap voltages 67
11.3. Topographical height profile 68
11.4. Scanning tunneling spectra 69
11.5. Corrected scanning tunneling spectra 70

12.1. V-shaped defect 74
12.2. Overview image 75
12.3. Hexagonal pyramidal structures in wurtzite GaN 76
12.4. Schematics of the three-dimensional structures 77
12.5. Oscillations of the tunneling current 78
12.6. Oscillations at different gap voltages 79
12.7. Scanning tunneling spectra 80

13.1. Constant-current XSTM image 84
13.2. Schematics of meandering 85
13.3. Frequency distribution of the lateral displacements 86
13.4. Frequency distribution of the jumps in lateral displacement 87

15.1. Overview mosaic image 97
15.2. Density of dislocations 99
15.3. Derivative image 100
15.4. Spatial distribution of dislocation angles 101
15.5. Frequency distribution 103

16.1. Dislocation in a simple cubic crystal 106
16.2. Edge dislocation intersecting the GaN cleavage surface 108
16.3. Averaged line profile 109
16.4. Analyzed height profiles 110
16.5. Fits to the line profiles 111
16.6. Comparison of measurement and simulated image 112
16.7. Simulated displacement fields of two dislocations 113

Abbreviations

DFT	density functional theory
DOS	density of states
ELO	epitaxial lateral overgrowth
GGA	generalized gradient approximations
HVPE	hydride vapor phase epitaxy
LDA	local density approximation
LED	light emitting diode
ML	monolayer
PAW	projector augmented wave approach
STM	scanning tunneling microscope / microscopy
STS	scanning tunneling spectra
XSTM	cross-sectional scanning tunneling microscopy
XSTS	cross-sectional scanning tunneling spectroscopy

Symbols

a	Lattice constant (3.189 Å)
B	Barrier height
c	Lattice constant (5.185 Å)
d	Separation of tip and sample
D_t	Density of states of the tip per unit of volume
e	Elementary charge (positive sign) or Euler number
E_A	Energy level of acceptors
E_{CB}	Energy of the conduction band edge at the bulk
E_{CS}	Energy of the conduction band edge at the surface
E_D	Energy level of donors
E_F	Fermi Energy
$E_{F,\mathrm{tip}}$	Fermi Energy of the tip
E_g	Band gap
E_s	Energy of a state ψ_s in the sample
E_t	Energy of a state ψ_t in the tip
E_V	Energy of the valance band
E_{vac}	Energy level at vacuum
E_{VB}	Energy of the valence band edge at the bulk
E_{VS}	Energy of the valence band edge at the surface
$F_{1/2}(x)$	Fermi-Dirac integral
$f(E)$	Fermi-Dirac distribution

G	Shear modulus
$\hbar$	Planck constant/2π
I, I_0	Current
k_B	Boltzman constant
m	Inverse Poisson's ratio
m_n^*	Effective mass of electrons
m_p^*	Effective mass of holes
M_{ts}	Matrix element of the transition of ψ_t to ψ_s
n	Concentration of negative charge due to electrons
N_a^-	Concentration of ionized acceptors
N_C	Effective density of states in the conduction band
N_d^+	Concentration of ionized donors
N_V	Effective density of states in the valence band
p	Concentration of positive charge due to holes
R	Radius of curvature of the tip
$\vec{r}_0$	Position of the tip
S_{Ga}	Unoccupied Ga surface state
S_N	N-derived occupied surface state
S_Q	Quantized state
T	Temperature
$T(\varepsilon, eV, z, U)$	Transmission coefficient
u	Displacement in x direction
U	Potential
V	Voltage
v	Displacement in y direction
V_0	Height of the potential $V(z)$
V_{set}	Gap voltage

V_{vac}	Difference in electrostatic potentials
$V(z)$	Time-constant potential
w	Space charge region in the semiconductor
x_{mod}	Length of one period of the modulation
$\bar{X}, \bar{X}', \bar{\Gamma}, \bar{M}$	High symmetry points in the surface Brillouin Zone (defined on page 25)
α, φ	Opening angle of the v-shaped defect
Δ_i	Jump in lateral displacement between the i-th and (i+1)-th "v"
δ_i	Displacement of the i-th "v"
δ_{max}	Maximum possible displacement of a "v"
$\Delta\Phi$	Contact potential
κ	Inverse decay constant
λ	Displacement
ν	Poisson's ratio
ξ_{vac}	Electric field within the gap
$\rho(\vec{r}_0, E_F)$	Density of states of the sample at the Fermi energy being measured at the position $\vec{r}_0$ of the tip
ρ_t	Density of states of the tip
Φ	Work function
Φ_m	Work function of the metal tip
Φ_s	Work function of the tip
Φ_t	Work function of the sample
ϕ_s	Barrier potential
Φ_{SC}	Work function of the semiconductor
χ_{SC}	Electron affinity of the semiconductor
ψ_s	A state in the sample

ψ_t	A state in the tip
$\psi(z)$	Wave function

Acknowledgement

I would like to thank Prof. Dr. R. E. Dunin-Borkowski and Prof. Dr. J. Mayer for the opportunity to prepare this thesis at the Institute for Microstructure Research at the Forschungszentrum Jülich GmbH.

Special thanks go to Priv.-Doz. Dr. Ph. Ebert for supervising this thesis and his guidance during the experiments and analysis of the data as well as to Prof. Dr. M. Morgenstern for the co-supervision.

I also want to thank Prof. Dr. J. Neugebauer and Dr. L. Lymperakis from the Computational Materials Department at the Max-Planck-Institut für Eisenforschung GmbH for the *ab initio* calculations used in Chapter 8.

I would further like to thank Prof. Dr. M. Dähne, Dr. H. Eisele and Dr. A. Lenz from the Institut für Festkörperphysik at the Technische Universität Berlin as well as Dr. B. Grandidier, Dr. D. Stiévenard and J.-P. Nys from the Institut d'Electronique, de Microélectronique et de Nanotechnologie in Lille, France for giving me the opportunity to perform measurements using their equipment.

Thanks also to go to my colleagues Dipl.-Phys. M. Schnedler and Dipl.-Phys. V. Portz for the joint development of the *STM-Analyzer*, Dipl.-Ing. K. H. Graf for his technical assistance and Dipl.-Ing. D. Weber for the fabrication of the calibration sample

Last but not least, I would like to thank my family, thereof especially S. Ullmann, M.Sc for her support and trust.

Band / Volume 20
Stacked device structures for resistive memory and logic
R. D. Rosezin (2012), 137 pp
ISBN: 978-3-89336-777-1

Band / Volume 21
Optical and electrical addressing in molecule-based logic circuits
M. Manheller (2012), XIV, 183 pp
ISBN: 978-3-89336-810-5

Band / Volume 22
Fabrication of Nanogaps and Investigation of Molecular Junctions by Electrochemical Methods
Z. Yi (2012), 132 pp
ISBN: 978-3-89336-812-9

Band / Volume 23
Thermal Diffusion in binary Surfactant Systems and Microemulsions
B. Arlt (2012), 159, xlvi pp
ISBN: 978-3-89336-819-8

Band / Volume 24
Ultrathin Gold Nanowires - Chemistry, Electrical Characterization and Application to Sense Cellular Biology
A. Kisner (2012), 176 pp
ISBN: 978-3-89336-824-2

Band / Volume 25
Interaction between Redox-Based Resistive Switching Mechanisms
C. R. Hermes (2012), iii, 134 pp
ISBN: 978-3-89336-838-9

Band / Volume 26
Supported lipid bilayer as a biomimetic platform for neuronal cell culture
D. Afanasenkau (2013), xiv, 132 pp
ISBN: 978-3-89336-863-1

Band / Volume 27
15th European Workshop on Metalorganic Vapour Phase Epitaxy (EWMOVPE XV) June 2-5, 2013, Aachen, Germany
A. Winden (Chair) (2013)
ISBN: 978-3-89336-870-9

Band / Volume 28
Characterization, integration and reliability of HfO_2 and $LaLuO_3$ high-κ/metal gate stacks for CMOS applications
A. Nichau (2013), xi, 177 pp
ISBN: 978-3-89336-898-3

Band / Volume 29
The role of defects at functional interfaces between polar and non-polar perovskite oxides
F. Gunkel (2013), X, 162 pp
ISBN: 978-3-89336-902-7

Band / Volume 30
Parallelisation potential of image segmentation in hierarchical island structures on hardware-accelerated platforms in real-time applications
S. Suslov (2013), xiv, 211 pp
ISBN: 978-3-89336-914-0

Band / Volume 31
Carrier mobility in advanced channel materials using alternative gate dielectrics
E. Durğun Özben (2014), 111 pp
ISBN: 978-3-89336-941-6

Band / Volume 32
Electrical characterization of manganite and titanate heterostructures
A. Herpers (2014), ix, 165 pp
ISBN: 978-3-89336-948-5

Band / Volume 33
Oxygen transport in thin oxide films at high field strength
D. Weber (2014), XII, 115 pp
ISBN: 978-3-89336-950-8

Band / Volume 34
Structure, electronic properties, and interactions of defects in epitaxial GaN layers
P. H. Weidlich (2014), 139 pp
ISBN: 978-3-89336-951-5

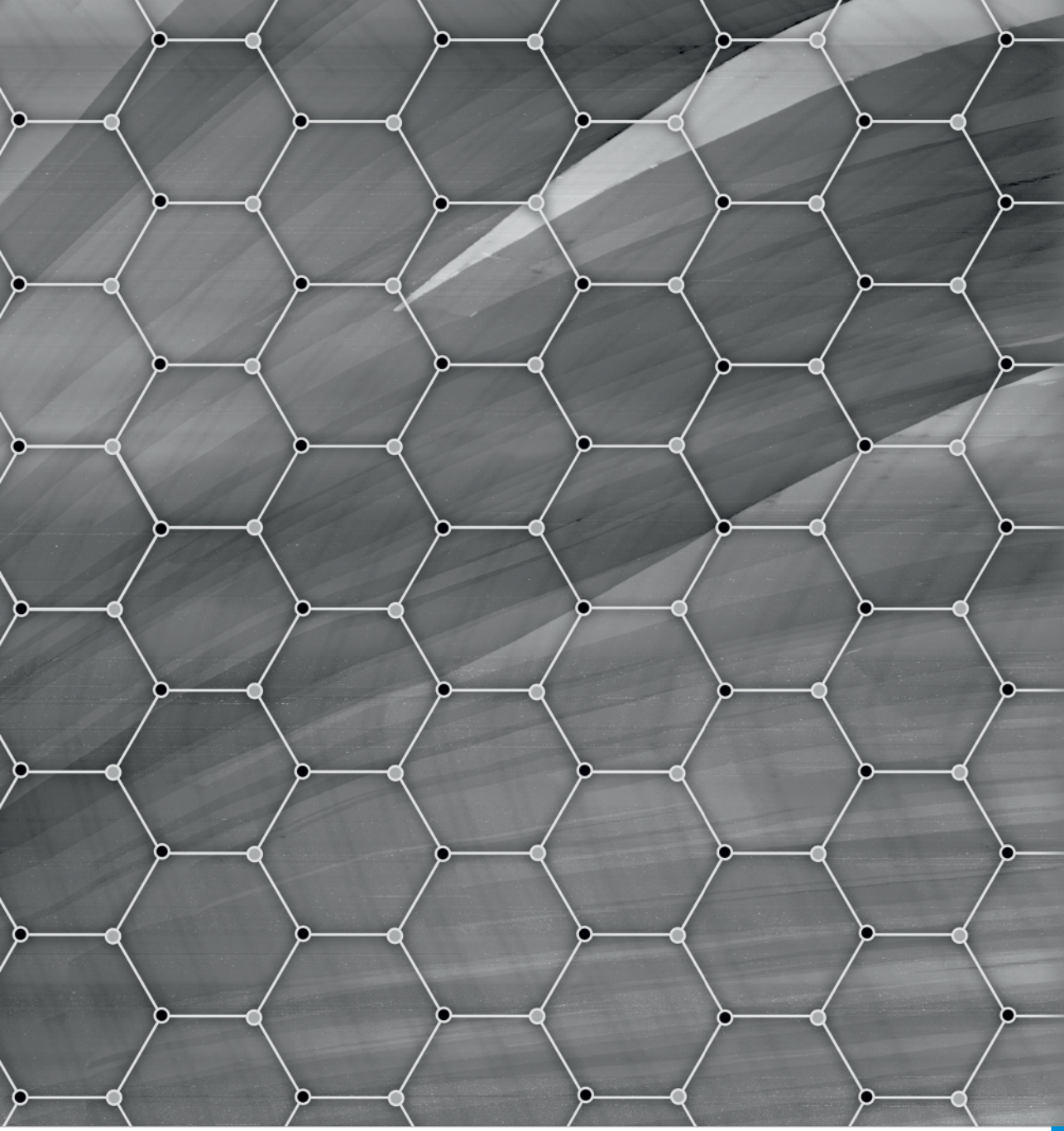

Information / Information
Band / Volume 34
ISBN 978-3-89336-951-5

JÜLICH
FORSCHUNGSZENTRUM